

Wireless Transformer Condition Monitoring System

Hermanus Andries Jakobus Zandberg

2013

Wireless Transformer Condition Monitoring System

By

Hermanus Andries Jakobus Zandberg

Submitted to:

The Department of Electrical Engineering in fulfilment of the
requirements for the Magister Technologiae in Electrical
Engineering at the

Cape Peninsula University of Technology

November 2013

Declaration

I, Hermanus Andries Jakobus Zandberg, submit this thesis in fulfilment of the requirements of the degree of Magister Technologiae (MTech) in Electrical Engineering.

I claim that this is my own original work and that it has not been submitted in this or similar form for a degree at any other tertiary institution.

Hermanus Andries Jakobus Zandberg

CANDIDATE

31 / 10 / 2013

DATE

CPUT, Cape Town Campus

PLACE

Synopsis

Pole mounted transformers (PMT) in rural areas present an opportunity for local utilities to do current monitoring on these systems. These transformers are exposed to abnormal amounts of stress due to the vast power demand in these areas. The aim of this study is to develop a more cost-effective condition monitoring system. Transformer current monitoring can be a dangerous practice if not done by suitably trained utility electricians. Hence this study is partly aimed at the elimination of hazardous working environments associated with manual electrical measurements.

An investigation to determine a safe and cost-effective way to obtain the electrical measurements required from PMTs is undertaken. Although current measurements can be done with a current clamp-on meter, these measurements still take place at the phases of the transformer and are unsafe. The possibility of implementing wireless data gathering on current clamp-on meters is therefore investigated. This is made possible by a wireless sensor node (WSN) which gathers information and transmits it wirelessly to a WSN base station.

This wireless solution is battery powered, necessitating battery replacements, therefore leading to the investigation of magnetic fields, magnetic materials and magnetic induction. A current clamp able to generate a high voltage (HV) output with minimal magnetic field strength is developed. The magnetic fields produced by the transformer's phase cables are used to generate an alternating voltage. With the help of a microcontroller and an energy harvesting circuit, this voltage is converted and used to charge supercapacitors. The magnetic fields are also used to determine the current flow in the transformer phase cables when the device is not in energy harvesting mode.

The device will then undergo comprehensive laboratory testing to determine its accuracy and durability, and is then used to do 'real life' current measurements, the results of which are compared against an off-the-shelf current monitoring device.

Acknowledgements

The completion of this thesis would not have been possible without the support, inspiration and encouragement of the following people and organisations to whom I would like to express my sincere gratitude.

- I would like to thank God for providing me with the knowledge, perseverance and above all the opportunity to do this study and seeing it through to the end.
- Jacques Wheeler, Professor Richardt Wilkinson, Professor Gerhard de Jager, and Shaun Kaplan for their patience, guidance and support with this project.
- Eskom TESP for funding provided.
- The Centre for Instrumentation Research (CIR) staff, store members and students, in particular Khaleel Jooste for his ongoing assistance and willingness to help out.
- Special thanks to my colleagues Gavin Mutch and Garry de Villiers for their input.
- I would also like to thank my parents, Herman Zandberg and Susan Zandberg for always supporting and encouraging me through tough times. A special thanks to my little sister, Elzaan Zandberg for all her effort and help with the finalising of this document. Finally I would like to thank Nelani Jacobs for her role in supporting me and encouraging me to push through and finish this.

Table of Contents

Declaration	i
Synopsis.....	ii
Acknowledgements	iii
Table of Contents	iv
List of Figures and Tables.....	vii
List of Symbols and Abbreviations	xi
Chapter 1 - Introduction	1
1.1 Problem statement.....	2
1.2 Problem approach.....	4
1.3 Outline of thesis	5
Chapter 2 - Characteristics of condition monitoring system.....	6
2.1 Typical power grid layout.....	7
2.1.1 Transformer loading profile	9
2.1.2 Household power loading profile	11
2.1.3 Transformer failures	12
2.1.4 PMT monitoring procedures.....	14
2.1.5 Typically expected urban load harmonics	16
2.2 Harmonic measurement	17
2.2.1 Field measurements on a distribution transformer in Paarl.....	17
2.2.2 Current measurement techniques dealing with harmonics.....	19
2.2.3 Available transformer monitoring systems	21
2.3 WSN – an alternative transformer monitoring solution.....	23
2.3.1 Types of WSNs.....	24
2.3.2 WSN framework.....	25
2.4 WSN power consumption	26
2.4.1 The sensor.....	27
2.4.2 The processor.....	27
2.4.3 The transceiver	28
2.4.4 TelosB typical power consumption illustration.....	29

2.5	Energy storage.....	30
2.5.1	Batteries	31
2.5.2	Capacitors	33
2.6	Energy harvesting techniques	35
2.6.1	Solar energy	35
2.6.2	Wind energy	36
2.6.3	Vibration energy	37
2.6.4	Magnetic field energy	38
2.6.5	Evaluation of energy harvesting techniques	38
Chapter 3- Design considerations.....		41
3.1	The transformer	41
3.1.1	Transformer current	41
3.1.2	Transformer cables	42
3.2	The energy harvesting and current monitoring system	42
3.2.1	The CT	43
3.2.2	Electrical control and energy management	43
3.2.3	CT electrical specifications	44
3.2.4	Possible voltage and power expectations	45
3.2.5	Accuracy of current measurements	46
Chapter 4- The current monitoring system.....		47
4.1	Electromagnetism.....	48
4.1.1	Magnetic materials	50
4.2	CT design	53
4.2.1	Core material	53
4.2.2	CT circuit analysis	59
4.2.3	Current ratio.....	61
4.2.4	Core area.....	62
4.2.5	Saturation voltage	62
4.2.6	Power output.....	63
4.2.7	Core losses.....	65
4.2.8	Copper losses.....	66
4.2.9	Input power.....	67

4.2.10	Efficiency	68
4.3	Electronic design	72
4.3.1	The rectifier	72
4.3.2	The voltage regulator.....	73
4.3.3	Energy storage	75
4.3.4	Voltage analysis.....	75
4.3.5	The load	80
4.3.6	Testing the condition monitoring system	84
Chapter 5- CT calibration.....		88
5.1	Results	89
Chapter 6 - Field testing		92
Chapter 7 - Conclusions		96
7.1	Problems encountered	97
7.2	Proposed future work	98
References.....		99
Appendices.....		107
Appendix A–CT Design		107
Appendix B– Electronic circuit schematic layout.....		122
Appendix C– Calibration procedure		124
Appendix D – WSN program.....		125

List of Figures and Tables

Figure	Title	Page
Figure 2-1	Illustration of a typical power grid, as redrawn from (Chambers, 1999).....	7
Figure 2-2	PMTs in Matzikama district.....	8
Figure 2-3	Loading profile of a 200kVA PMT in commercial sector	9
Figure 2-4	Loading profile of a 200kVA PMT in rural sector	10
Figure 2-5	South African residential loading profile, as redrawn from (Eskom, 2011). 11	
Figure 2-6	Daily energy usage on a typical summer day, as redrawn from (Atikol, et al., 1999).....	12
Figure 2-7	Utility worker performing routine transformer measurements (Mughal, 2008).....	15
Figure 2-8	PMT taken in the Matzikama district Municipality (Lutzville).....	16
Figure 2-9	Phase current measurement during off-peak period	18
Figure 2-10	Phase current measurement during peak period	18
Figure 2-11	Typical WSN applications, as redrawn from (de Villiers, 2009).....	23
Figure 2-12	Basic construction of a WSN, as redrawn from (Jun Zheng, 2009)	25
Figure 2-13	Star and mesh network topology, as redrawn from (de Villiers, 2009).....	28
Figure 2-14	Measured power consumption of WSN (de Villiers, 2009).....	30
Figure 2-15	Layout of a lithium-ion battery cell (Goodenough, et al., 2007)	32
Figure 2-16	Some capacitor types and sizes.....	33
Figure 2-17	Energy and power properties of various power sources (Johansson & Andersson, 2008).....	35
Figure 2-18	Solar photovoltaic cell, as redrawn from (Flipsen, 2004).....	36
Figure 2-19	CT clamped onto a motor phase conductor (Ahola, et al., 2008)	38
Figure 3-1	Block diagram of circuit for power management and current measurement	44
Figure 4-1	Overview of system structure leading to CT design.....	47
Figure 4-2	Magnetic field around current carrying wire, as redrawn from (Mclyman, 2004).....	48
Figure 4-3	Flux density and total flux bounded by an area, as redrawn from (Erickson & Maksimović, 2004)	49
Figure 4-4	Magnetic field produced by an air core	50

Figure 4-5 Magnetization curve, as redrawn from (Mclyman, 2004)	51
Figure 4-6 Flux in a magnetic core produced by a coil, as redrawn from (Mclyman, 2004).....	51
Figure 4-7 Different stages of magnetic core excitation, as redrawn from (Mclyman, 2004)	52
Figure 4-8 CT design procedure	53
Figure 4-9 B-H characteristic curve of an iron core with sinusoidal excitation, as redrawn from (Erickson & Maksimović, 2004).....	54
Figure 4-10 Estimated B-H characteristics of iron core (a) where hysteresis and saturation are neglected and (b) only hysteresis is neglected, as redrawn from (Erickson & Maksimović, 2004)	54
Figure 4-11 B-H curve of ferromagnetic material (Gupta, 1999).....	55
Figure 4-12 B-H curve of soft ferrite material (Ferroxcube, 2012).....	56
Figure 4-13 Illustration of CT core	56
Figure 4-14 Hysteresis loop, as redrawn from (Mclyman, 2004).....	58
Figure 4-15 Secondary AC monitoring system, as redrawn from (Mclyman, 2004)	59
Figure 4-16 Equivalent circuit of CT redrawn from (Mclyman, 2004).....	59
Figure 4-17 Relation between input and output current, as redrawn from (Mclyman, 2004)	60
Figure 4-18 Current simulation rig	63
Figure 4-19 Measured voltage (V_LOAD), current (I_LOAD) and power (F1) before CT saturation.....	64
Figure 4-20 Measured voltage (V_LOAD), current (I_LOAD) and power (F1) at maximum power	65
Figure 4-21 Calculated efficiency of CT	68
Figure 4-22 Voltage delivered by CT with change in load resistance with 120A primary current for different secondary wire gauges	69
Figure 4-23 CT current output linked to changes in load resistance with 120A primary current for different secondary wire gauges	70
Figure 4-24 CT power output linked to changes in load resistance with 120A primary current for different secondary wire gauges	71
Figure 4-25 Design process for the electronic circuit.....	72
Figure 4-26 High current shunt regulator, as redrawn from (Texas Instruments, 2004)	73

Figure 4-27 Simulation of voltage and current regulation..... 74

Figure 4-28 Voltage regulation circuit with actual circuit capacitance 75

Figure 4-29 Illustration of hysteresis band 76

Figure 4-30 Threshold detector, as redrawn from (Maxim, 2012) 77

Figure 4-31 Simulation graph illustrating output voltage control across the load..... 79

Figure 4-32 Simulation graph illustrating upper and lower threshold voltages 79

Figure 4-33 Current measurement circuit 80

Figure 4-34 Waveform illustration for current measurement 81

Figure 4-35 Flow diagram of WSN program layout..... 82

Figure 4-36 Timing structure of the WSN program 83

Figure 4-37 Condition monitoring system connected to test rig 84

Figure 4-38 Transformer condition monitoring system laboratory measurement..... 85

Figure 4-39 Capacitor charge cycle indicating voltage ripple 85

Figure 4-40 Flow diagram of WSN with ripple averaging 86

Figure 4-41 Capacitor charge curve indicating voltage samples taken on ripple 86

Figure 5-1 Accuracy of current monitoring system over full measurement range 89

Figure 5-2 Error measurement on current monitoring system..... 90

Figure 5-3 Error measurement comparison between ARC CT and OTS CT 90

Figure 6-1 Internal layout of mini substation in Paarl 92

Figure 6-2 OK Minimarket phase current tests 93

Figure 6-3 Close-up of current monitoring devices on blue phase feeding Mash Street 94

Figure 6-4 Measurement of transformer phase current supplying Mash Street 95

Table	Title	Page
Table 2-1	Transformer system components, defects and failures (Chambers, 1999).....	14
Table 2-2	Comparison of techniques for AC current measurements (McEachern, 1993)	21
Table 2-3	Transformer monitoring systems (Fluke, 2012)(Microdaq, 2012)(Ecologix controls ltd, 2012).....	22
Table 2-4	WSN comparisons (Anon., 2012)(AE Sensors, 2012)(Anon., 2012)	24
Table 2-5	Supercapacitors, their manufacturers and specifications (Sahay & Dwivedi, 2009).....	34

Table 2-6 Supercapacitors, cost per Farad and KJ, as redrawn from (Sahay & Dwivedi, 2009)	34
Table 2-7 Comparison between energy harvesting methods	39
Table 3-1 PMT specifications (WBSEDCL, 2012)	41
Table 3-2 CT Electrical design specifications	45
Table 4-1CT performance characteristics	71
Table 5-1 ARC CT results compared with OTS CT results as measured at $100A_{rms}$	91

List of Symbols and Abbreviations

Roman alphabet

A	Area, m ²
A_c	Area of material core, m ²
B	Magnetic flux density, T
B_c	Flux density in ferrite material core, T
B_g	Flux density in the air gap, T
B_{max}	Maximum flux density, T
F	Frequency, Hz
\mathcal{F}_c	Magneto motive force of ferrite material core, At
\mathcal{F}_g	Magneto motive force of air gap, At
H	Magnetic field strength, A/m
I	Electric current, A
I_{Load}	Load current, A
I_m	Magnetising current, A
I_{sat}	Saturation current, A
J	Current density, A/m ²
K	Constant value, no unit
L	Inductance, H
ℓ_c	Core length, m
ℓ_g	Length of the air gap between two U core, m
ℓ_{MP}	Magnetic path length of U core, m
N	Number of turns, no unit
N_p	Number of primary windings, no unit
N_s	Number of secondary windings, no unit
P	Power, W
P_c	Core losses, W
P_{ce}	Acceptable core losses, W
r	Radius, m
\mathfrak{R}	Reluctance, At/Wb
\mathfrak{R}_c	Reluctance of air gap, At/Wb

\mathfrak{R}_g	Reluctance of air gap, At/Wb
\mathfrak{R}_t	Reluctance of total circuit, At/Wb
t	time, s
V_L	Line voltage, V
V_p	Peak voltage, V
$Wtfe$	Core mass, W

Greek alphabet

Δ	Delta, indicates a change in the parameter to which it is attached, no unit
ε	Indicates strain, no unit
μ	Mu, indicates magnetic permeability, Vs/Am
μ_r	Relative permeability, no unit
μ_0	Permeability of free space, Vs/Am
ϕ	Indicates magnetic flux, Vs

Abbreviations

AC	Alternating current
ADC	Analogue to digital converter
ARCCT	Average RMS calibrated current transformer
AWG	American wire gauge
CPU	Central processing unit
CT	Current transformer
DC	Direct current
DGA	Dissolved gas analysis
EMF	Electromotive force
EES	Electrical energy storage
GIO	General input output
GPRS	General packet radio service
GPS	Global positioning system
HV	High voltage
IC	Integrated circuit
IEEE	Institute of electrical and electronic engineers
LHA	Left hand axis

LV	Low voltage
Lth	Lower threshold
OTS	Off-the-shelf
OTSCT	Off-the shelf current transformer
PC	Personal Computer
PCB	Printed circuit board
PD	Partial discharge
PMT	Pole mount transformer
RAM	Random access memory
RF	Radio frequency
RHA	Right hand axis
RISC	Reduced instruction set computing
RMS	Root mean square
ROM	Read only memory
THD	Total harmonic distortion
Uth	Upper threshold
USB	Universal Serial Bus
WSN	Wireless sensor node

Chapter 1

Introduction

Public service corporations spend a substantial amount of capital each year on the purchasing and maintenance of electrical distribution transformers(Khawaja, et al., 2013). These transformers form the backbone of the national power grid, consisting of thousands of transformers, ranging from the power generation phase to the distribution phase.

Malfunctioning of distribution transformers, as well as unscheduled downtime, causes local utility companies to receive numerous complaints regarding production losses, spoiled food products and claustrophobic reactions from individuals in lifts. Failures can also cause life-threatening situations, like malfunctioning traffic lights and fire alarm systems, and inconveniences experienced by people with disabilities who rely on electrical devices for their basic needs. The impact of such power failures on the community is so great that it is impossible to accurately determine the financial implications of the outage caused by one transformer. It is therefore the responsibility of the local utility to effect immediate repairs on the faulty transformer (Voss, et al., 2005).

Due to a lack of information pertaining to the operating condition of transformers, a self-sustainable condition monitoring system is proposed as a possible solution to this problem. This system will make use of a WSN, which gathers relevant information about the transformer, in order to be able to predict current health states.

1.1 Problem statement

Illegal connections (electricity theft) in informal settlements results in overloading of low voltage (LV) networks (Suresh & Elachola, 2000). This causes transformers to be loaded beyond their design specifications (Swarztrauber & Shafir, 2012) resulting in excessive thermal stress leading to a significant reduction in life expectancy. Illegal connections may also result in a short circuit in the network, causing decompression of the transformer windings, friction and possibly a further short circuit created between the windings (Wang, et al., 2002).

Dissolved gas analysis (DGA) is a proven testing procedure used by electrical utilities to perform condition monitoring on transformers. This system enables the utility to test the transformer by analysing dissolved gasses in the oil of the transformer, allowing early detection of faulty conditions. The DGA testing procedure is limited, in the sense that it can only be used on more expensive power transformers, and not on smaller, dry-type power transformers (Catrinu & Nordgård, 2010). Dry-type power transformers are greatly influenced by partial discharge (PD) (Werle, et al., 2000)– a process that occurs when an electric field overpowers the dielectric strength of the transformer's winding insulation. Potential causes for this are over voltage, over current, lightning strikes, or natural insulation deterioration over time (Judd, et al., 2005).

In order to prevent such breakdowns, transformers require some form of monitoring while in operation. Typical monitoring systems capable of detecting PD problems are not cost-effective when it comes to smaller, dry-type transformers. This is due to the fact that the purchasing cost of the measuring system may even exceed the value of the transformer, making this an unfeasible option (Werle, et al., 2000). This suggests room for improvement in information gathering systems related to smaller transformers.

In order to perform daily measurements on dry-type PMTs, an operator would have to climb up the pole and physically take the measurements. In so doing, he would be exposed to hazardous situations, such as electrocution and falling from the pole mounted platform (Catrinu & Nordgård, 2010).

Transformers have an expected lifespan of a few decades, and the ability to monitor current and predict failure of HV power transformers is very important for energy utilities (Hong, 2009). Time based maintenance and replacements are required on power transformers; however, this is not feasible in the current electrical industry. Such transformers are large capital investments, necessitating monitoring. Online monitoring as well as condition based monitoring is now being used more frequently (Saha, 2003).

The development of a wireless current monitoring system, able to be positioned on the transformer, is proposed in this thesis. This device will take regular current measurements and transmit them to a remote location, which will eliminate some of the safety hazards usually associated with traditional monitoring techniques(Mughal, 2008). In order to successfully monitor the operational current patterns of the transformer remotely, a number of measurements will have to be taken. Therefore, a WSN is used to take the measurements and continuously monitor the transformer. The TelosB WSN has low power consumption, a user-friendly interface, and wireless capability.

However, attached to this proposed solution, is the problem that the WSN is likely to be battery powered. Battery powered devices require regular battery replacement, thereby negating batteries as the power source of the WSN (Ye, et al., 2004). Energy harvesting is therefore proposed as a possible solution to this problem. If this approach is feasible, energy can be harvested from the environment and manipulated to power the monitoring device. By successfully monitoring HV transformers over a period of time, the information gathered can be used to determine operational current patterns and provide an accurate and reliable source of information to local utilities. Successful implementation of this system would allow for unforeseen failures and transformer downtime to be minimised.

1.2 Problem approach

An accurate, wireless, current measurement system, capable of monitoring a 100kVA PMT, without the need for routine maintenance, will be designed. The following questions will be answered:

- What are the normal operating conditions of a typical PMT?
- Can an accurate current sensor be developed for this project?
- Which WSN is best suited for this application?
- What are the power requirements of the end node for the WSN?
- Which energy harvesting techniques are best suited for this application?
- Can the energy harvesting source deliver sufficient energy to power the system, if connected to a 100kVA transformer, in a rural environment?
- Will this wireless system be able to accurately measure current in the field, when compared to similar commercial products?

A thorough literature review will be conducted on transformer operation, in order to be able to identify the reasons for transformer malfunctions, and create a clear understanding on typical transformer behaviour. By analysing a few PMTs, typical operational patterns can be observed, allowing for the identification of areas of stress that PMTs typically endure.

In order to log this information successfully, a smart sensor will have to be installed on the transformer. If possible, typical operation patterns can then be documented, which may lead to more effective maintenance schedules and prevent unnecessary damage to transformers and neighbouring devices. Therefore, a WSN is chosen, which can be programmed to act as a central computer; having the ability to control electronics for energy harvesting as well as current measurements. After data collection, the information will be remotely transmitted to a logging station for further analysis.

The focus of this thesis revolves around two main aspects – accurate, sustainable measurements, and providing the WSN with a constant and reliable source of power.

1.3 Outline of thesis

The layout of the remaining part of this thesis is as follows:

Chapter 2: This chapter covers a rural distribution network and illustrates the normal loading conditions of a typical PMT. Possible causes of transformer failure are identified, with overloading highlighted. The dangers associated with current monitoring procedures are also investigated. Power quality of a typical rural environment is defined, focusing on distortions of the current wave and techniques required for accurate measurements. Existing measurement systems, various WSN systems, and energy harvesting and storage techniques are evaluated.

Chapter 3: Here, the design specifications of the monitoring system are discussed, which includes all relevant information pertaining to the PMT, and block diagrams illustrating the building structure for the measurement current transformer (CT) as well as the electronic circuitry associated with the energy harvesting and current measurements.

Chapter 4: This chapter is divided into three main sections. The first section begins with a study on electromagnetism, covering magnetic fields, magnetic materials and magnetic induction. The design of the CT is then discussed, covering its material selection, manufacture and testing. The second section explains the electrical circuit of the CT and how it implements smart power control, transforming alternating current (AC) into direct current (DC) for storage purposes, and looks at the way in which the current measurements are done. Laboratory testing of the system is covered in the third section.

Chapter 5: Here, the calibration procedure is described, and the results of a comparison between the wireless current measurement device and an industrial CT are shown, in order to verify accuracy and repeatability

Chapter 6: This chapter describes field tests done on an actual transformer when it is supplying power to a residential area in Paarl, with the aim of proving the measurement technique and energy harvesting concept.

Chapter 7: Here, the conclusions of the study are drawn, and proposals are made with a view to future improvements that could be made to the monitoring system.

Chapter 2

Characteristics of condition monitoring system

Distribution transformers are passive devices with no movable parts, therefore they require little care and maintenance, resulting in a simple, rugged and durable construction (Anon., 1977). Although the design is durable, these devices still have their limits, including voltage spikes, over current, transient vibrations and temperature violations (Brittian, 2012) (Kim, et al., 2011). Protection against such issues increases a transformer's lifespan, however, factors such as human error, rodents and system deterioration with age can still have an impact on their operation (Hemming, 2012).

When a new section of land is developed for urban usage, the entire area is evaluated and the amount of inhabitants predetermined. A power plan is then developed which will determine the amount of power required per household. In addition, some leeway must be provided for future development in the area. As the growth rate of the area increases as much as 16% (Gaunt, et al., 2012) so does the power usage over time. According to the City of Cape Town Municipality, a typical power plan will provide room for development for at least fifteen years, after which the energy consumption must be re-evaluated and adapted.

The South African power grid is facing the reality of illegal power connections and excessive loading in informal settlements (Gaunt, et al., 2012). Although these settlements also have a need for power supply, the power lines initially installed for the community are only sufficient for the planned power demand. As the informal settlement develops, more power outlets are required, and the local utility cannot always provide on such short notice. This typically causes the community to take matters into their own hands and install their own power outlets. As the demand for household power increases, individuals start to tap into the live power line (Gaunt, et al., 2012), resulting in the initial power plan no longer being valid and the fifteen year period decreasing dramatically.

The dense housing structure of these informal settlements therefore increases the energy demand, and transformers are easily overloaded within the first few years of instalment. In order to prevent the overloading of PMTs, more frequent information regarding the loading state of these devices is required. This study focuses on PMTs with a power rating of 100kVA. In addition, a data monitoring system must be developed in order to collect the data from the transformers.

2.1 Typical power grid layout

In order to gain a better understanding of the problem, the following section provides a brief overview on where exactly the problem is situated and on what sector of the power grid this study will focus on. A general power grid layout is shown in Figure 2-1.

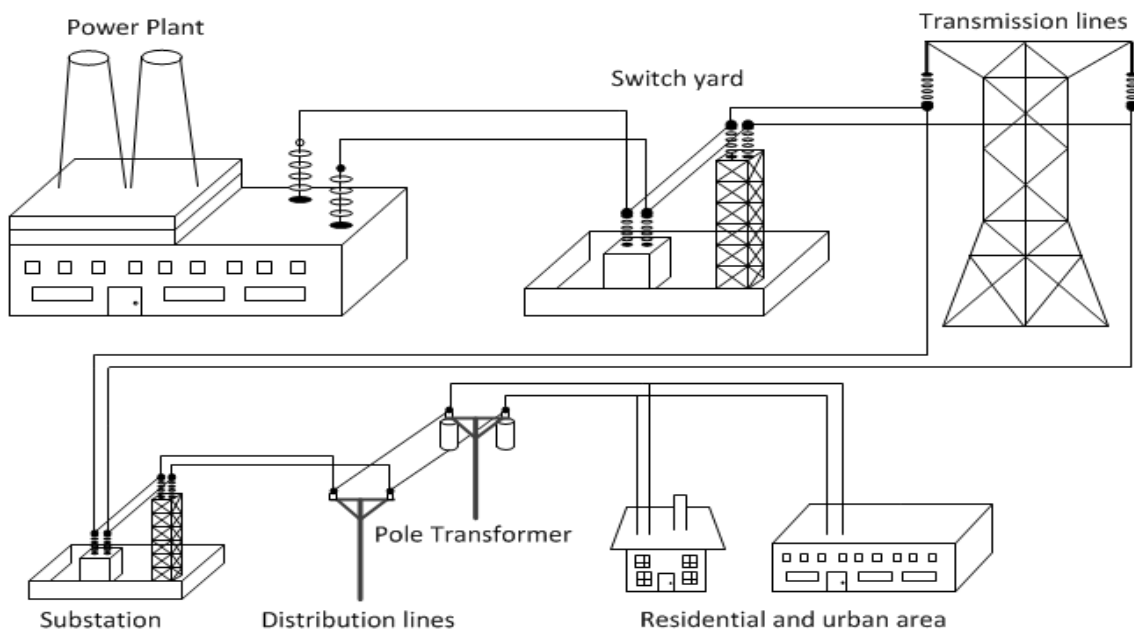


Figure 2-1 Illustration of a typical power grid, as redrawn from (Chambers, 1999)

The power generated from the power plant is transported via transmission lines – overhead cables used to transmit HV electricity – to the switching yard and substation. The latter regulates the voltage coming from the switching yard, and incorporates distribution transformers that step down the voltage. This voltage is still of such magnitude that it cannot be used by industry, which is then fed into distribution lines, being either overhead or underground cables. Overhead lines tend to be more favourable due to cost effectiveness(Chambers, 1999).

The distribution lines then carry the electricity to PMTs situated in residential and rural areas, which step the voltage down further from 11kV down to 420V. The secondary side of the PMT is connected to the grid that provides power to meet the demands from the industrial, urban or residential areas (Chambers, 1999).

The information on PMTs, shown in Figure 2-2, was provided by the Matzikama Municipality, and illustrates the different types of PMTs currently used in the Matzikama Municipality district. Here it can clearly be seen that PMTs are generally used to supply power to the towns in this particular district.

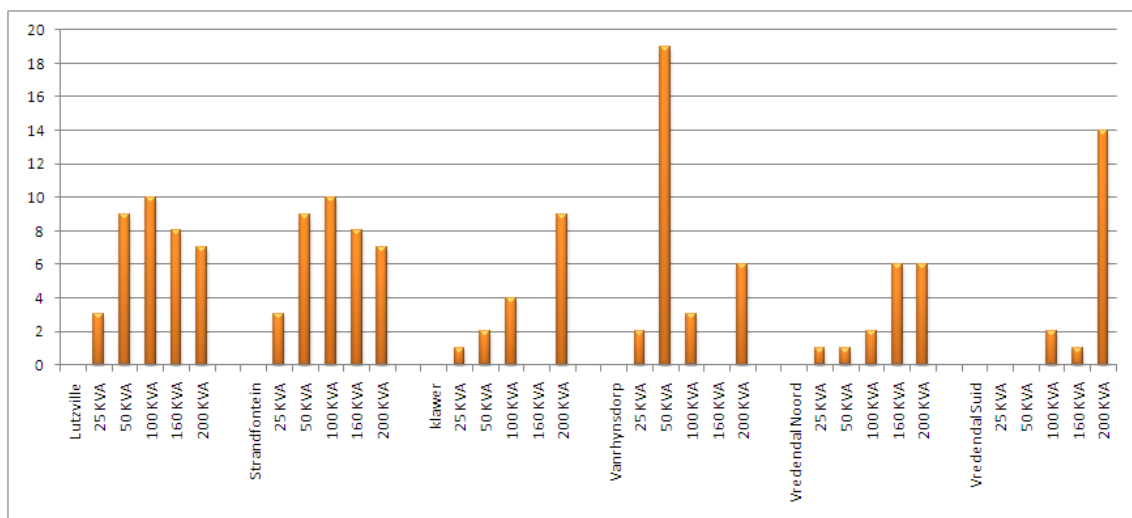


Figure 2-2PMTs in Matzikama district

The transformers in Figure 2-2 are from five different towns in the Western Cape. By analysis, the amount and types of PMTs being used in the field in one district can be seen. Currently, there is no monitoring being done on any of these transformers (according to the electrical department). Therefore, the overall condition of these devices is unknown. PMTs are the most common choice of transformer for installation in informal settlements. The reason for this is that these settlements are usually situated in unstable sections of land that are vulnerable to the risk of flooding (Gaunt, et al., 2012). Hence the safety of the community and well-being of the transformers is a problem that the local utility is faced with daily. When these transformers suffer extensive damage, they become a danger to their surroundings due to the possibility of electrical shocks and fires (Hemming, 2012).

2.1.1 Transformer loading profile

The City of Cape Town Municipality was contacted and an interview conducted in order to receive first-hand information on the issues mentioned in the previous section. In so doing, it was possible to observe the physical data of two types of transformers, each from a separate location. This is done to help clarify why the problem of transformer overloading is increasing. Figure 2-3 is a typical loading profile of a 200kVA PMT, being the main supply to a small commercial and residential area. The transformer was monitored for the duration of one year, with half hour sampling intervals. This gives a general idea as to how the transformer is loaded, and helps to provide clearer insight on the typical stress factors it will endure under operation.

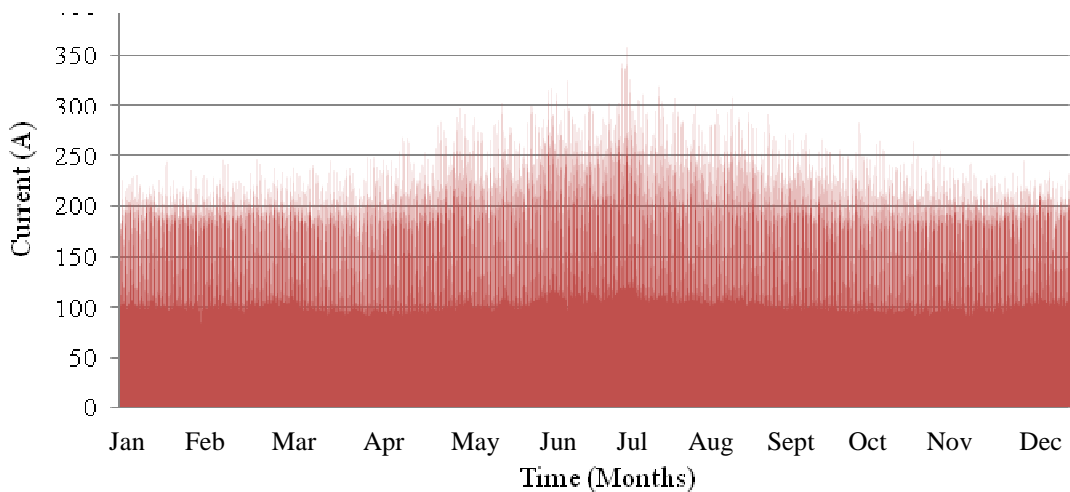


Figure 2-3 Loading profile of a 200kVA PMT in commercial sector

Here it can be seen that the average current passing through the secondary phases of the transformer is around 100A (indicated by the darker red section). This graph also indicates the overloading magnitude of this transformer. The peak current increases between May and October, rising from 250A to a maximum of 350A. By calculation it was determined that when the transformer is operating at 100% the total secondary phase current should not exceed 266A, meaning that a current of 350A is substantially more than its designed operational range. This puts the transformer at risk of overheating and consequently deteriorating the winding dielectric.

Figure 2-4 is a loading profile of a 200kVA PMT situated in a rural area, where the average secondary phase current is also around 100A. The average current flow profile is more or less the same than that of the transformer from the commercial sector; however, there is a big difference in the overloading of the transformer. Notice that the loading profile in Figure 2-4 is not what would typically be expected from an informal settlement in the City of Cape Town district. The loading profile presents higher energy consumption during the summer months from December to March which is unexpected, as this is the summer months where less lighting and heating is required. The exact rural area where this transformer is from is unknown, therefore it can only be speculated what the cause is for this unexpected rise in energy demand. Take note that rural areas are high risk areas where floods and fires are likely to occur. If a fire or flood broke out where this study was done, it could easily affect the energy usage of that area(Gaunt, et al., 2012).

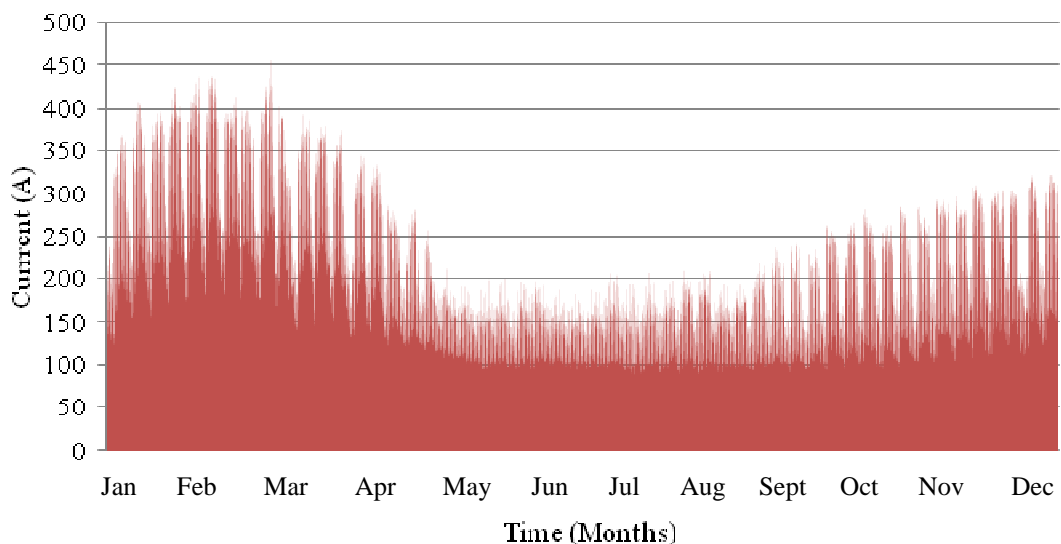


Figure 2-4 Loading profile of a 200kVA PMT in rural sector

Here it can be clearly seen that the transformer suffers from overloading. This occurs for eight of the twelve months, i.e. between October and May. The maximum secondary phase current reaches a peak of 450A meaning that this transformer was driven well beyond its rated capacity.

According to the municipality, the loading profile reduced once an additional transformer was installed. However, with the addition of this transformer to the grid, the old one still remained in operation.

The fact that this transformer has been operated beyond its design specifications means that severe damage may have been caused to the internal winding dielectric. Therefore, by not replacing the old transformer, a weak link has now been created in the grid. If the load were to increase further, the old transformer might fail, and the new transformer would then have to supply the entire load, placing it now at risk of failure.

The overloading experienced by the two transformers above accelerates their ageing and increases the possibility of premature failure, hence the need for condition monitoring. The implementation of such monitoring would enable electrical utilities to keep track of the loading of their transformers and commission upgrades before unnecessary damage is caused.

2.1.2 Household power loading profile

This section investigates the loading of a PMT in a residential area, with the South African residential profile provided by Eskom. A circular graph is shown in Figure 2-5 which illustrates the key energy consuming components in modern day South African households (Eskom, 2011).

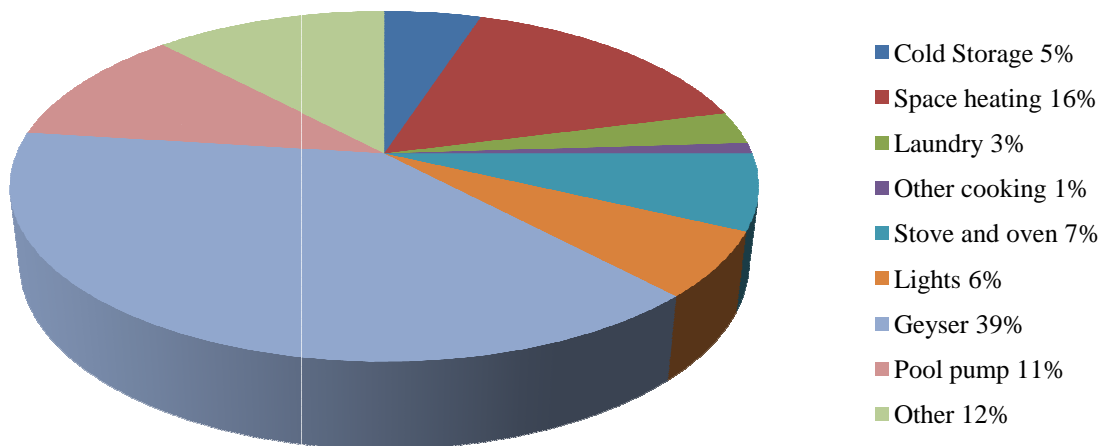


Figure 2-5 South African residential loading profile, as redrawn from (Eskom, 2011)

Here it can be seen that up to 55% of the total energy used in a household is consumed by heating appliances. These mainly comprise space heating and geysers for water heating. Furthermore, in Figure 2-6, the daily usage patterns of different household appliances on a typical summer day are shown (Atikol, et al., 1999).

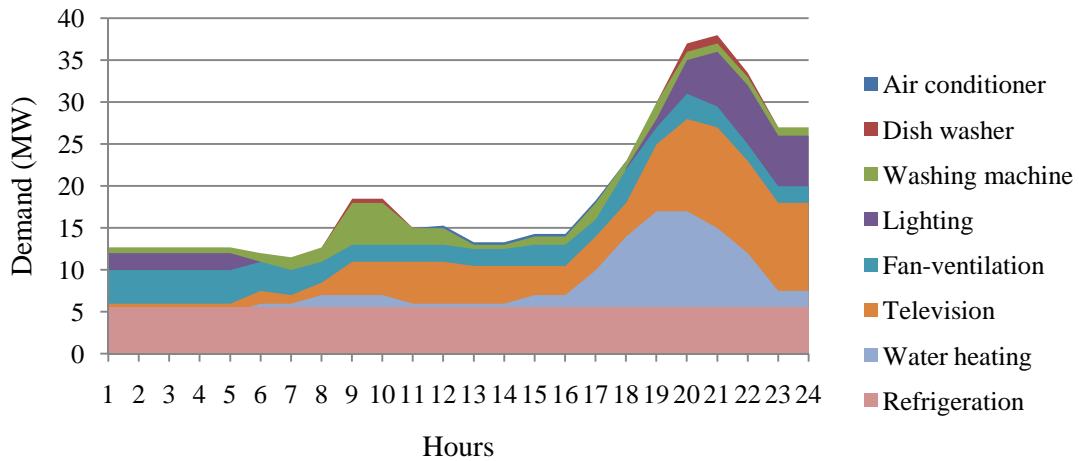


Figure 2-6 Daily energy usage on a typical summer day, as redrawn from (Atikol, et al., 1999)

Here it is shown that the peak power consumption most likely occurs between the hours of 07h00 and 11h00. The second peak is then from 16h00 to 23h00, reaching a maximum at around 21h00. As the energy consumption is directly linked to the transformer, the maximum residential load at 21h00 means that the PMTs are most likely operating at or above their maximum power ratings at this time. Therefore, condition monitoring during these peak periods is of vital importance. Notice that start and end energy usage of Figure 2-6 does not line up as expected. This is not of significant importance as the main focus of this illustration is to determine which appliances are likely to be operational during certain periods of the day.

2.1.3 Transformer failures

A large number of national power grid transformers are operated beyond their specified design lifetime. This offers financial benefits to the local utility; however, the main reasons for this are the mixture of aged and newer transformers as well as limited resources. An aged transformer will not necessarily malfunction, but the loading conditions it will endure are unknown.

Previous incidents may have weakened the winding dielectric, hence weakening the transformer, and therefore creating a potential weak link in the power grid (Chambers, 1999).

Transformer malfunctions occur when it can no longer handle operational stresses. Beginning from its initial installation, a transformer is introduced to thermal, mechanical, chemical, electrical and electromagnetic stresses. All of these factors contribute toward its deterioration (Khawaja, et al., 2013).

Transformer deterioration may result in:

- a decrease in dielectric strength, i.e. reducing the ability to resist short circuits, lightning strikes and switching impulses induced on the line,
- a reduction in the ability to withstand mechanical tension,
- exposure to thermal conditions, i.e. a circuit that carries current no longer has the ability to withstand overload conditions, and
- electromagnetic energy transfer implications, i.e. problems with energy transfer when occurrences like overloading and over-excitation take place.

Transformer failure is most likely to occur when one of the above mentioned parameters are exceeded during operation (Chambers, 1999). The system components of power distribution transformers are shown in Table 2-1. Here the various stresses transformers are exposed to as well as the possible resulting defects, faults and failures can be seen.

This study will focus on the electromagnetic and the current carrying circuits of the transformer. Table 2-1 shows that transformers generally have problems with overheating. Increases in temperature relate directly to a decrease in the life expectancy of the transformer. Increased temperatures result in insulation deterioration and failure (Khawaja, et al., 2013). Short circuits are the main cause of overheating in a transformer, which would not occur if the conductor insulation is intact.

Table 2-1 Transformer system components, defects and failures (Chambers, 1999)

System Components	Possible Defects	Fault and Failure Mode
Dielectric System <ul style="list-style-type: none"> • Major insulation • Minor insulation • Leads insulation • Electrostatic screens 	<ul style="list-style-type: none"> • Abnormal oil ageing • Abnormal paper aging • Partial Discharge • Excessive water • Oil contamination • Surface contamination 	Flashover due to: <ul style="list-style-type: none"> • Major insulation • Minor insulation • Leads insulation • Electrostatic screens
Mechanical System <ul style="list-style-type: none"> • Clamping • Winding • Leads Support 	<ul style="list-style-type: none"> • Loosening of windings • Loosening of winding clamps 	Failure of solid insulation due to: <ul style="list-style-type: none"> • Failure of lead support • Winding displacement (radial axial twisting)
Electromagnetic circuit <ul style="list-style-type: none"> • Core • Core winding • Structure insulation • Clamping structure • Magnetic shields • Grounding circuit 	<ul style="list-style-type: none"> • Circulating current • Leakage flux • Aging lamination • Short circuit 	Excessive gassing due to: <ul style="list-style-type: none"> • General overheating • Localized overheating • Arcing discharges • Short circuited turns in winding conductors
Current carrying circuit <ul style="list-style-type: none"> • Leads • Winding conductors 	<ul style="list-style-type: none"> • Bad joints • Bad contacts • Contact deterioration 	Short circuit due to: <ul style="list-style-type: none"> • Localized overheating

2.1.4 PMT monitoring procedures

Condition monitoring on PMTs require current logging meters which have to be permanently implemented on the transformer. Data would then be downloaded from the device at regular intervals and the power source (batteries) regularly replaced. This monitoring system would not only be time consuming for the utility personnel but would also be at risk of being stolen or vandalised. In addition, if there is no power access point at the bottom of the pole, the downloading of data and battery replacements would have to take place fairly close to the transformer's secondary phases (ABB, 2013). Figure 2-7 shows how the current in PMTs is typically measured. Access is usually gained via a ladder, as the transformers are mounted on poles of approximately 5m from ground level, which places the operator in danger of electric shock or falling (Mughal, 2008).



Figure 2-7 Utility worker performing routine transformer measurements (Mughal, 2008)

This study will focus on these transformers for condition monitoring. Note the enlarged section of the transformer in Figure 2-8 – here is where utility workers will have to climb to in order to take current measurements at the phase cables. These phase cables are only insulated up to the connection point and the transformer terminals are open, therefore there is a good possibility of electric shock due to the unsafe access to the terminals. In addition, distorted current waves produced by various load types also present measurement problems, and will be discussed in the following section.



Figure 2-8PMT taken in the Matzikama district Municipality (Lutzville)

2.1.5 Typically expected urban load harmonics

Harmonics associated with urban settlements can be rather similar to those associated with informal settlements. This section comprises three studies on expected total harmonic distortion (THD) levels in urban areas.

The first study determined the voltage and current distortion levels at seventy-six sites, ranging from pump stations, oil refineries and community colleges. Data collection was done by random spot checks lasting between one to two hours. Within this time, measurements of harmonic levels are taken at one minute time intervals or faster, depending on the rate of change in the respective loads. It was shown that measurements taken at motels and pump stations most closely represented urban loading environments, generating THD levels up to a maximum of 3.4% (Govindarajan, et al., 1991).

The second study determined the power system harmonic levels on seven different distribution circuits, which are exposed to various load types, ranging from residential to industrial. Data collection was done over a period of one week, with measurement time intervals of one hour.

The first location was a purely residential load, and represents the typical harmonic profile the measurement CT would be exposed to, with the maximum current distortion ranging between 1.84% and 3.45% (Shuter, et al., 1989).

The third study determined the harmonic current and voltage levels present in commercial, industrial and residential customers. Data collection was once again done over a period of one week. It was shown that apartment buildings (residential load) displayed an almost repetitive characteristic and indicated that a maximum THD value of 6.38% was detected during this measurement period (Emanuel, et al., 1993).

According to the three surveys above, the harmonics expected in residential environments are somewhere between 1.84% and 6.38%. The next section covers a physical harmonic measurement taken in a residential area.

2.2 Harmonic measurement

This section focuses on current measurements taken in Paarl – a small farming and residential area near Cape Town – where harmonics in the system and the different techniques used to take current measurements will be considered.

2.2.1 Field measurements on a distribution transformer in Paarl

Current waveforms produced by AC power systems are generally assumed to be sinusoidal. However, when these systems are exposed to different load types – consisting of variable speed drives, data processing centres and personal computers – harmonics are introduced into the system, which distort the pure sine wave (McEachern, 1993). Figures 2-9 and 2-10 show current measurements done on a local residential transformer.

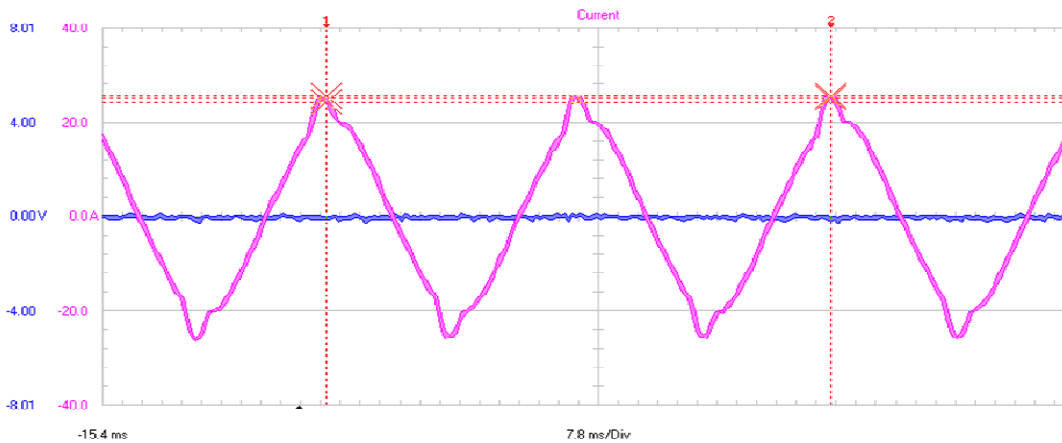


Figure 2-9 Phase current measurement during off-peak period

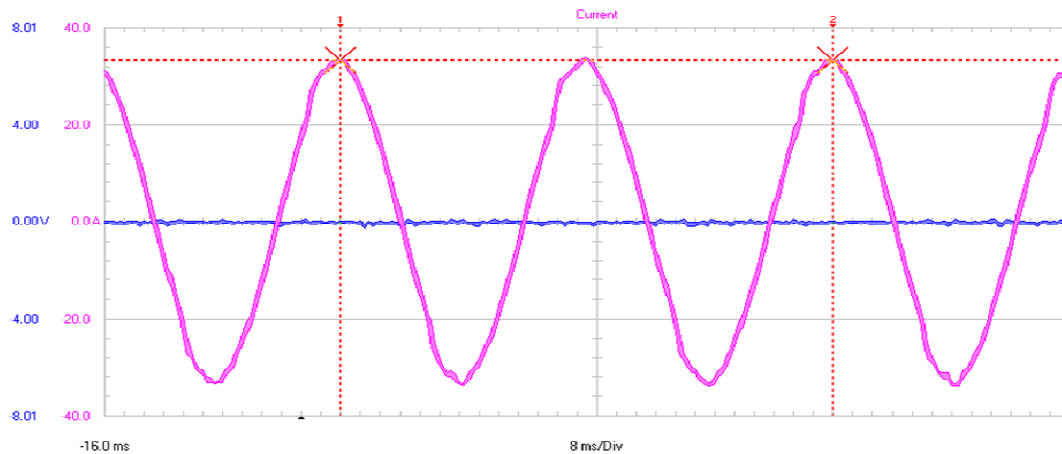


Figure 2-10 Phase current measurement during peak period

The above waveforms were measured at a mini substation in Paarl – achieved by connecting a current clamp to a secondary phase of the transformer and capturing the data by a Fluke 43 power quality analyser. Figure 2-9 shows a heavily distorted wave with a THD of 9.9% which was measured between the morning hours of 07h00 and 08h00. By referring back to Figure 2-6, the typical loads that can be expected during this time are likely to be a mixture of washing machines, fans, televisions, water heating and refrigerators, all of which (bar water heating) have the potential to load the system with harmonics(Sumper & Baggini, 2012)(Arrillaga & Watson, 2003)(Cyganski, et al., 1989).

The waveform in Figure 2-10 was taken between the morning hours of 09h00 and 10h00. This wave has a THD of only 3.3%, exhibiting less distortion than the waveform in Figure 2-9. This may be due to the fact that when the wave was captured, the total burden placed on the transformer was more resistive due to heating elements, which is characteristic of the peak power demand period of residential areas.

2.2.2 Current measurement techniques dealing with harmonics

This section discusses the various types of current measurement techniques available. Each technique provides a different outcome, which is investigated.

2.2.2.1 True RMS measurements

True RMS can be described as the heat generated when a voltage is applied across a resistive load. Therefore, in order to measure true RMS, a thermal detector is used (Deyer, 2001), which, according to (McEachern, 1993), is the most accurate method. By using the heating method, the measurement is taken over a time interval (usually in the order of minutes) where a steady voltage is required. The time taken (time constant) to measure the true RMS value is a critical factor. More recently, however, a digital method can be used which makes use of sampling intervals to measure the magnitude of the signal. For accuracy, the sampling rate must be one hundred times the operating frequency, and the following equation is implemented in order to calculate the RMS value of the signal (McEachern, 1993).

$$True_{RMS} = \sqrt{\frac{M_1^2 + M_2^2 + M_x^2}{N}} \quad (1)$$

Where:

$True_{RMS}$	True RMS value
M_1^2, M_2^2, M_x^2	Measurements taken and squared with itself
N	Number of measurements taken

The sampling rate would therefore be 5kHz on the South African power grid, necessitating one hundred samples to be taken over a period of twenty milliseconds. The processor then converts each sample to digital format, which are then squared. At the end of the time period, the squared values are summed and divided by the total number of samples taken in order to calculate the mean value.

The RMS value is then determined by taking the square root of the mean value (McEachern, 1993).

2.2.2.2 Average RMS calibrated

This method determines the average value of a rectified signal. When dealing with purely sinusoidal signals, the average value measured by the device can be scaled to RMS by multiplying the average with a constant $K = 1.11$ (Deyer, 2001). Digital meters that use this method are the most common metering devices, according to (Deyer, 2001)(Bakshi, et al., 2008)(Jones, 2008)(Anand, 2006). However, accurate measurements are only possible if the signal is purely sinusoidal. Therefore, errors are introduced when harmonics are present.

2.2.2.3 True RMS to DC Converter ICs

Two RMS to DC converter ICs from different manufactures are compared. The first IC is the LTC1967 from Linear Technology. This uses a sigma-delta computational technique to calculate the true RMS value, is able to operate from single rail supplies at 4.5V - 5.5V and 330 μ A, bandwidths of 500kHz and linearity and gain error readings of 0.5% – 1% (Williams, 2012).

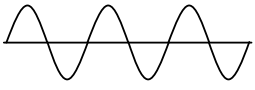
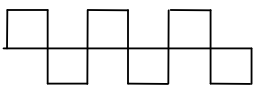

The second IC is the AD637 from Analogue Devices. According to the datasheet, this device uses a monolithic RMS to DC converter. It can be used to compute true RMS values from fairly complex waveforms, is able to operate from a rail-to-rail supply of 3V and 2.2mA, a bandwidth of 800MHz and a total error reading of 0.02% – 0.1% (Analogue Devices, 2012).

The accuracy of both ICs are fairly close by comparison, however, the operating bandwidth of the AD637 is greater than that of the LTC1967. The operating frequency of transformers in South Africa is around 50Hz; therefore, the bandwidth of both these devices is more than adequate. However, accurate measurements are not only expensive but also have high power consumption. According to RS Components (local electronics supplier), the LTC1967 would cost \$7.47 (US) per unit and the AD637 as much as \$122.64 (US) per unit.

2.2.2.4 Measurement comparisons

Table 2-2 illustrates the different waveforms that may be implemented on the current measurement system and shows the values of true RMS readings. In addition, a comparison is made in order to determine the percentage error reading experienced when using alternative measurement strategies.

Table 2-2 Comparison of techniques for AC current measurements (McEachern, 1993)

Wave Forms	Description	True RMS	Average RMS calibrated	Error %
	Sine wave	100A	100A	0%
	Square wave	100A	90A	10%
	Sawtooth Wave	100A	103.3A	3.3%

Here the effect of a pure sinusoidal waveform on the different measurement techniques is illustrated. Provided that the waveform does not become distorted, all of the above techniques are adequate for current measurements. When the input wave deforms, the average RMS calibrated error percentage increases. True RMS measurements are the most accurate, but are also the most expensive method (Fletcher, 2004) (Fletcher, 2012).

2.2.3 Available transformer monitoring systems

A list of devices available for this current monitoring application is shown in Table 2-3. The current range, accuracy, and operating life for the device are of utmost importance. The Fluke and CL600 loggers both have a large current operation range and are fairly accurate over the entire measurement range, making them suitable for transformer data monitoring applications. The first three devices have a built-in memory which can be useful. The fourth device has no internal storage capability, but uses an alternative powering method providing a longer operational lifespan. The Fluke is the most advanced and by far the most expensive meter of them all. However, it is not necessary to use such expensive metering equipment for current monitoring. The perfect solution will be the most cost-effective one, while still providing accurate measurements.

All of the meters in Table 2-3 are fairly reliable as current sensing devices. The EcoCT makes use of wireless communication to transmit the measured data from the installation point to an Encocean receiver approximately 30m away. This eliminates the danger of electric shock and falling from a ladder. In addition, it uses magnetic induction from the primary energy source (current carrying conductor) to generate its operational power, therefore eliminating the need for batteries and allowing it to operate in the field for a number of years before servicing or replacement is required.

Although the accuracy and value of the device is not specified, it is clear that WSN is in a league of its own and cannot be compared to manual measurement methods. WSNs and the development of a self-sustainable transformer condition monitoring system will therefore be the foci of this study.

Table 2-3 Transformer monitoring systems (Fluke, 2012) (Microdaq, 2012) (Ecologix controls ltd, 2012)

Device name	Fluke 43 B	(TOU) CT logger	C1600 AC current clamp	EcoCT
Device Description	Power quality analyser, MultiMate and Oscilloscope	Monitoring of electric loads	AC Current logger	Self powering wireless current monitor
Phases	Single	Single	Single	Single
Range	0 – 1400A rms 0 – 2000A DC	> 0.25 A	0 – 600A	1 – 100A
Accuracy	True-rms current (AC + DC) ± 1%	N/A	0 – 400A ± 2% 400 – 600A ± 5%	N/A
Storage Capacity	Records two selected parameters for 16 days	Stores 32 000 data points	Stores 240 000 data pointes	Transmits data every 1 – 30s
Data Interface	RS 232 interface with Power Log Software	USB interface with SMART view software	RS232 Simple Logger Software	Wireless telegram and Ethernet gateway
Wireless Communication	N/A	N/A	N/A	Available
Power Source	Battery powered	Battery powered	Battery powered	Induction powered
Price	\$5177 (US)	\$189 (US)	\$570 (US)	N/A

In Sections 2.1 and 2.2, it has been explained why condition monitoring devices and energy harvesting are the safest way to implement current monitoring on PMTs. Literature has suggested that average RMS calibration is a plausible solution for condition monitoring on PMTs in residential areas. According to the literature and field measurements, the average RMS calibrated current meter provides accurate current readings, within its limits. It has therefore been decided to design a cost-effective transformer condition monitoring system, which harvests energy from the current carrying conductor, and measures current via the average RMS calibrated method.

2.3 WSN – an alternative transformer monitoring solution

WSNs are best suited for applications with long operational lifetimes and can be applied in large densities for a considerably low cost (Polastre, et al., 2005). Each sensor node has an internal processing unit which allows the gathering of information from the environment. The device wirelessly transmits the gathered information to a receiving base station, which processes the received information and determines if any irregular occurrences have taken place over the monitoring period (Tian & Georganas, 2002). For all of these reasons WSN is considered the best solution for the condition monitoring of transformers. A list of typical WSN applications is shown in Figure 2-11.

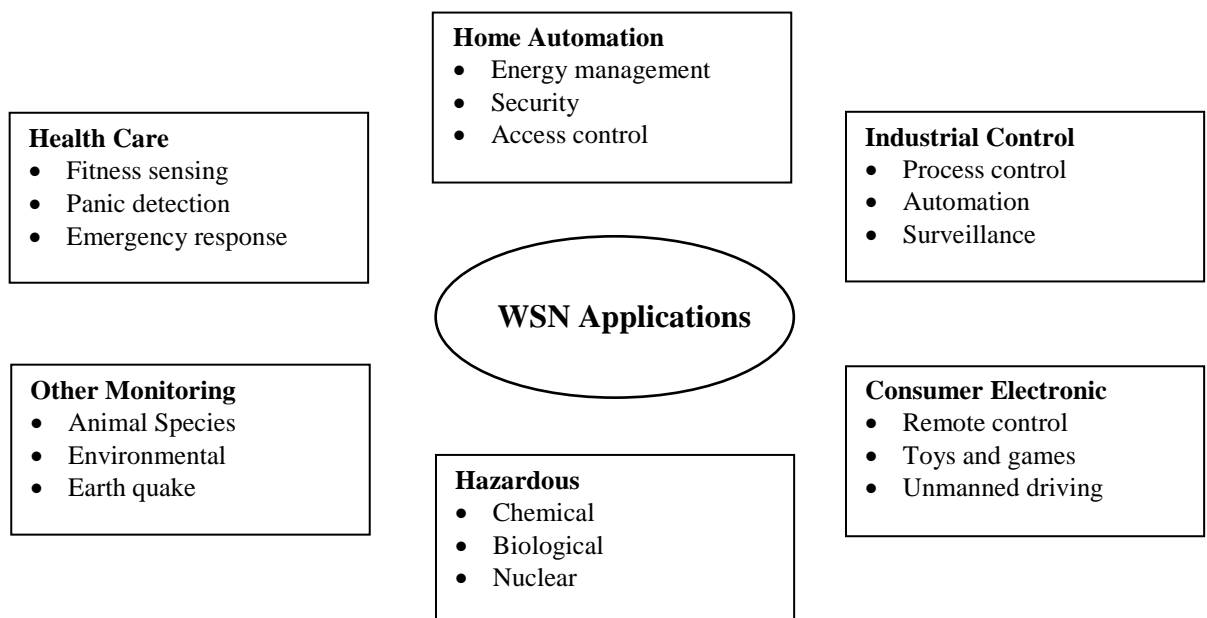


Figure 2-11 Typical WSN applications, as redrawn from (de Villiers, 2009)

2.3.1 Types of WSNs

A comparison of WSNs is shown in Table 2-4. These devices are able to communicate via the IEEE 802.15.4 international broadcasting standard, which enables the transmission and reception of information packages from additional nodes – in this case, the transmission of transformer data. A user-friendly interface allows for easy communication to the device. The USB interface enables the device to be powered from a computer which has two benefits – namely, the operator can easily access the data, and program the device. LV operation and high bit resolution ensures a cheap and easy power supply design and accurate readings to be taken from the analogue to digital converter (ADC). An important feature is the ability to use an easily accessible board layout, which allows the simultaneous use of multiple sensors, thereby harnessing the full potential of the microcontroller on the WSN platform.

The TelosB WSN is chosen as the operating platform for the condition monitoring of PMTs in this study. The explanation of this choice follows.

Table 2-4 WSN comparisons (Anon., 2012) (AE Sensors, 2012) (Anon., 2012)

WSN types	TelosB	3DM-Gx2	G-link - mXRS
Wireless properties	250 kbps 2.4 GHz IEEE 802.15.4 License	2.45 GHz IEEE 802.15.4 License	2.4 GHz IEEE 802.15.4 License
Micro controller	MSP 430	N/A	N/A
Integrated circuitry	ADC, DAC	ADC	ADC
Wireless Communication range	25 m Indoor 125 m Outdoor	70 m	70 m 2000 m
On-board sensor range	Humidity Temperature Light	Accelerometer, Gyro Magnetometer Temperature	Accelerometer Temperature
Bit resolution	16 Bit	16 Bit	12 Bit
Interface options	USB, UART, RS232	USB, RS232, RS422	USB, RS 232 Analogue, WSDA
External plug-in options	ADC, GIO, UART	N/A	N/A
Operating voltage	2.1 – 3.6 Vdc	5.2 – 9 Vdc	3.2 – 9 Vdc

Although the devices in Table 2-4 all appear to be in the same range, the TelosB seems to be the most suitable WSN for transformer monitoring. This device has:

- a sufficient data transmission range, enabling successful wireless monitoring,
- a 12 bit resolution, meaning that the ADC will provide an accurate data output,
- onboard access to general input output (GIO) pins, enabling the programmer to set certain pins of the microprocessor to a high or low state as required, and
- external ADC pins, allowing easy voltage conversions.

2.3.2 WSN framework

The development of wireless sensors was initiated at the University of California in 1999. WSNs consist of basic hardware units – namely, the processor, radio module, memory, power units and sensing unit, shown in Figure 2-12

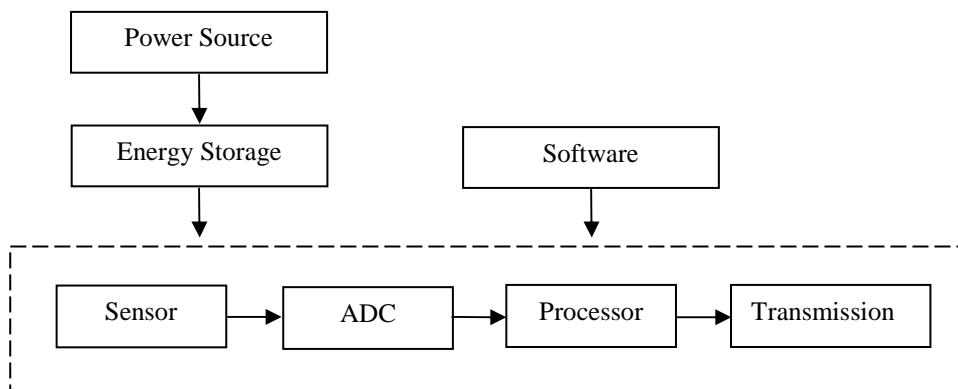


Figure 2-12 Basic construction of a WSN, as redrawn from (Jun Zheng, 2009)

The key components of the WSN will be used in the design procedure of a PMT condition monitoring system, and are explained by the following.

- The power unit supplies the power that keeps the WSN active. This power is harvested from various sources, e.g. solar, wind, piezoelectric, biochemical and magnetic flux.
- Energy storage allows the WSN to be continuously operational. This usually comes in the form of two AA batteries, providing the WSN with approximately 3V for its integrated electronics.
- Sensors are devices that retrieve information from the environment in the form of analogue data, and are found in all shapes and sizes. Typical sensor types used in WSN are temperature, sound, pressure, vibration and light.

- The ADC function is used to convert the analogue data from the sensor into twelve bit digital values for data processing.
- The processor is a low powered microprocessor designed for computational purposes. Forming the ‘brain’ of the device. It controls the program execution, radio protocols and sensor operation.
- Transmission of data is achieved by a communication radio system, enabling data packages to be transmitted and received wirelessly. This component has a drawback in that it is responsible for the energy loss in the WSN. Hence it is best to shut the radio down during periods when there is no data transmission.
- The memory consists of both random access memory (RAM) and read only memory (ROM). The former is used to store the data obtained from the sensor and the latter is used to store the program code which enables system operation (Labrador & Wightman, 2009).

2.4 WSN power consumption

Power consumption is an important factor to keep in mind when designing a data logging system to be implemented out in the field, where no external power source is available. It has been explained that battery power is unsuitable for WSN applications, and therefore a suitable power source must be selected, which can only be done when the power consumption of the device is known. Power control will be implemented in the design in order to create an efficient operating system. A typical WSN module consists of seven components, representing the core and platform of the module, as shown in Figure 2-12. The following section discusses the three components of the WSN that represent the load, and their typical power consumption characteristics.

2.4.1 The sensor

The TelosB platform comprises three on-board sensing units. However, these units are not used for transformer condition monitoring, and will therefore be disabled in order to minimise the loading of the device. It is therefore necessary to install another sensing unit on the WSN – namely, a CT.

These are extremely useful when the primary current becomes too high (for off-the-shelf metering equipment) to measure, providing a reduced output current that can indicate faults like over current, under current, peak currents etc. (Mclyman, 2004).

2.4.2 The processor

The ADC is an internal built-in function of the microprocessor which is used to measure the analogue voltage produced by the CT and convert it to digital data to be processed by the end user. The microprocessor functions in more or less the same manner as the central processing unit (CPU) of a computer. The CPU of a WSN comes in the form of a single integrated circuit (IC), being the size of a few cubic millimetres, with processing as its main function. It controls when and how information is gathered, as well as the dissection and storage of the information. Each IC is individually programmable to suit the requirements of the application.

The processor typically used for the TelosB platform is the MSP430 microcontroller, having 10kb of RAM, 48kB of flash memory and 128B of memory used for the storage of information gathered by the sensors. It consists of a sixteen bit reduced instruction set computing (RISC) processor, enabling effective operation by means of code and computing tasks. This device has extremely low power consumption during operation and a sleep function when not operational. As described by (David, et al., 2005) the typical operating voltage is between 2.7 – 3.6V, with operating current between 500 – 600 μ A while in sleeping mode it uses between 2.6 – 3 μ A. This leads to a power consumption of approximately 2.16mW in active mode and 10.8 μ W in sleeping mode.

2.4.3 The transceiver

As transmission is the biggest power consuming component in the WSN, a complete understanding of its function is necessary for optimum design efficiency of the device. Communication topologies comprise star, mesh and cluster tree configurations. Star networking topology is shown in Figure 2-13(A) and is efficient in the sense of its simplicity. The star network is a combination of information gatherers which transmit data back to the central WSN. The central node is in charge of transmitting this data via a General Packet Radio Service (GPRS) to a mainframe computer for storage.

This network topology is the easiest to implement, but is also the most vulnerable in the sense that all of the information gathered by the WSNs is transmitted to one central WSN. If this node were to fail, there would be no alternative way of transmitting the information to the mainframe computer.

Figure 2-13(B) represents a mesh network topology. This network is slightly more complex than its aforementioned counterpart, but is far more efficient. It also does not fully rely on the operation of one single central WSN, meaning that if one node ceases to function, an alternative route is used to transmit the information to the mainframe PC. However, the downside of this more reliable system is that it is more expensive, as it costs money to have extra nodes in the system which are able to transmit information. Both these systems are shown in Figure 2-13. The following section discusses the power consumption of the node, which will indicate whether or not the sensor node is a valid replacement for existing devices.

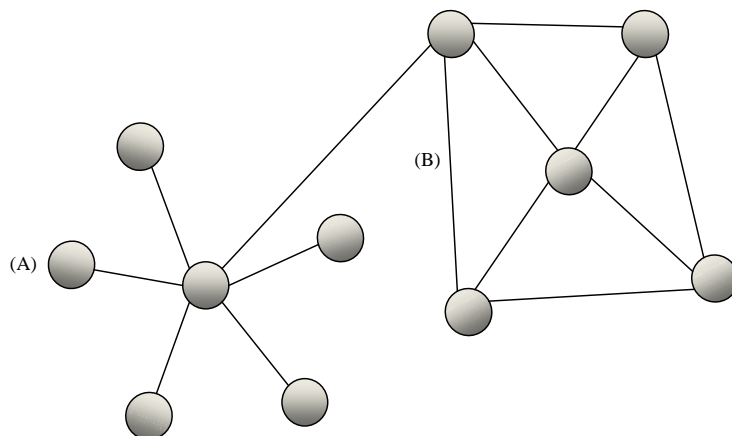


Figure 2-13 Star and mesh network topology, as redrawn from (de Villiers, 2009)

2.4.3.1 Radio control

The transmitter and receiver module (transceiver) used by TelosB is the CC240 which is a single chip device designed to operate on low power / voltage applications according to IEEE 802.15.4. It uses the Zigbee radio communication system, which is a flexible low cost solution operating in the 2.4GHz frequency band, requiring no licence, at between 2.1 – 3.6V.

The device runs on 18.8mA when in receiving mode, 17.4mA when in transmission mode, 426 μ A when in idle mode, 18.8 μ A when in shut down mode and requires 90 μ A to start up when in a non-operational mode. This leads to a power consumption of 67.68mW in receiving mode, 62.64mW in transmission mode and 66 μ W during idle, shut down and start up mode. In order to achieve further transmission distances, an external antenna may be mounted on the device. Practical tests in this regard have resulted in a 170m transmitting distance at a data rate of 250kbps, however, this test was only successful with line of sight operation.

2.4.4 TelosB typical power consumption illustration

Here the power consumption data from the TelosB data sheet is compared with measured data from a WSN, according to an experiment by de Villiers (de Villiers, 2009) which is shown in Figure 2-14. This illustrates the program running on the WSN. The device was attached to a transformer having a natural vibration caused by magnetomotive forces.

An accelerometer is mounted on the transformer and connected to the WSN, thereby allowing the WSN to sense the vibration, process these measurements and convert them to data packets. A total of ten measurements are taken per cycle and stored in the WSN's memory. When each cycle is complete the WSN activates its transmitter and broadcasts the data packets to a WSN base station. In order to gain a clear indication of the current demand of this device at a fixed voltage, an oscilloscope is connected to the WSN. This is done so that the power consumption can be calculated in order to design a suitable energy harvesting system to suit the application.

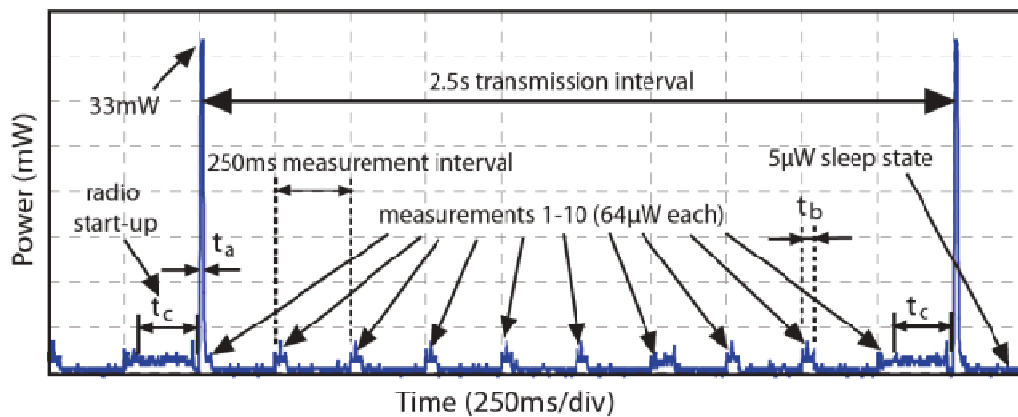


Figure 2-14 Measured power consumption of WSN (de Villiers, 2009)

According to (de Villiers, 2009) the average power consumption of the WSN was between $150 - 375\mu\text{W}$ depending on several duty cycles implemented in the program. This gives an estimated power consumption which is slightly different to that given by the TelosB data sheet, leading to specific design parameters for the energy harvesting system. This data will form the benchmark for this design, being the minimum energy required for the device to function.

A prudent approach would be to design the energy harvesting system to produce two or three times the required energy of the device, which can then be stored in energy reservoirs to be used when the energy harvesting system is offline. Therefore, the following section will look at energy storage reservoirs.

2.5 Energy storage

Modern day electronics depend on readily available energy, resulting in a great deal of interest being placed on energy management and storage. The need for renewable energy storage systems is influenced by factors such as sudden weather changes and other disruptions in the energy source. These storage systems have enormous potential in the reduction of energy consumption and cost (Dincer & Rosen, 2011). This section discusses potential storage facilities that can be used to power the transformer current monitoring device.

2.5.1 Batteries

The development of electrical energy storage (EES) systems has largely been based on chemical storage in the form of batteries, but is now struggling to keep up with modern day energy storage demands. Portable EES comes in various forms and sizes of rechargeable batteries, responsible for the powering of a wireless revolution incorporating global positioning systems (GPS), laptop computers, cell phones etc.

Typical problems attached to modern batteries are related to storage capacity and the number of recharge cycles available for long term applications. In order to improve the performance of a battery, the cell voltage and the amount of charge that the device can store must be increased, having a direct influence on its volume and weight(Goodenough, et al., 2007).

Focus therefore needs to be placed on new electrode development, which will improve thermodynamic stability and the charging rate; however, this tends to change the characteristics of the electrode material(Goodenough, et al., 2007).

Batteries and future developed cells will preferably possess the following characteristics:

- a high energy density,
- sufficient power production through the storage material, to support components as well as the structure of the cell,
- a long lifespan through electrochemical and material stability,
- robust design,
- be constructed of materials easily obtained from the manufacturing sector, and
- be safe to operate and have no toxic effects on the environment.

A single battery comprises singular or multiple electrochemical cells. These cells are connected in series or in parallel, depending on the required voltage and power the cell must deliver. There are two plates inside the battery, called the anode and cathode. The anode is the electropositive electrode, responsible for releasing electrons to power external components.

The cathode is responsible for releasing positive ions, which migrate inside the cells, while the electrons are forced to find an external path (Goodenough, et al., 2007). The electrolyte is the medium inside the battery in which the positive ions travel between the electrodes. This is a liquid solution containing dissolved salt. It is critical that the electrolyte remains stable between the two electrodes. Current collectors inside the battery are used for the transportation of electrons from the anode to the cathode.

Typically, anode electrodes are made of copper and cathode electrodes are made of aluminium. The electrodes also contain polymeric binders, enabling them to hold together the power structure of the battery and add a conductive substance like carbon black which dilutes the chemical mixture, increasing the batteries electronic conductivity properties (Goodenough, et al., 2007). The cell voltage is based on the energy made available by the chemical reaction taking place inside the battery.

An illustration of the internal structure of a lithium-ion battery cell is shown in Figure 2-15 in order to provide a better understanding of how a battery operates.

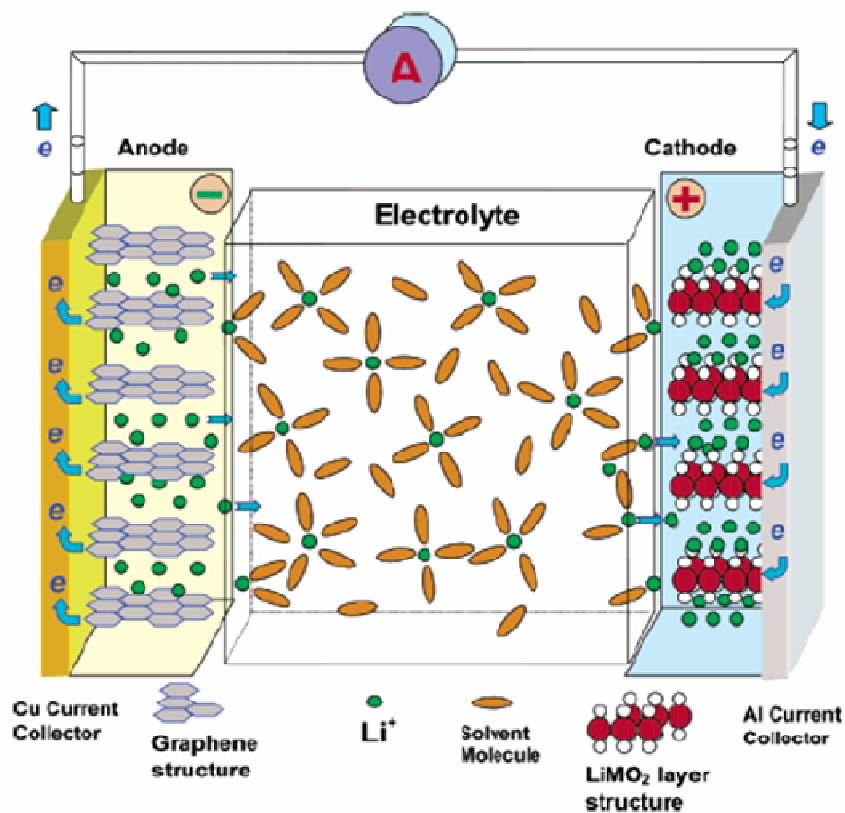


Figure 2-15 Layout of a lithium-ion battery cell (Goodenough, et al., 2007)

2.5.2 Capacitors

A capacitor is simply two conductive plates separated by a dielectric material. These plates store charge, the magnitude of which determines the capacitance (measured in Farads). This charge storage is nothing more than the accumulation of electrons on one of the plates, causing this plate to be more negative in relation to the other plate (Floyd, 1985). There are many types of capacitors – namely, mica, ceramic, tantalum, film, integrated circuit, Wima, paper, electrolytic, variable air and variable trimmer.

Some of these types are shown in Figure 2-16. The physical size of these devices gives some indication as to their charging capacity. The capacitors most superior in this regard are known as supercapacitors. These will be covered in more depth in the section to follow.

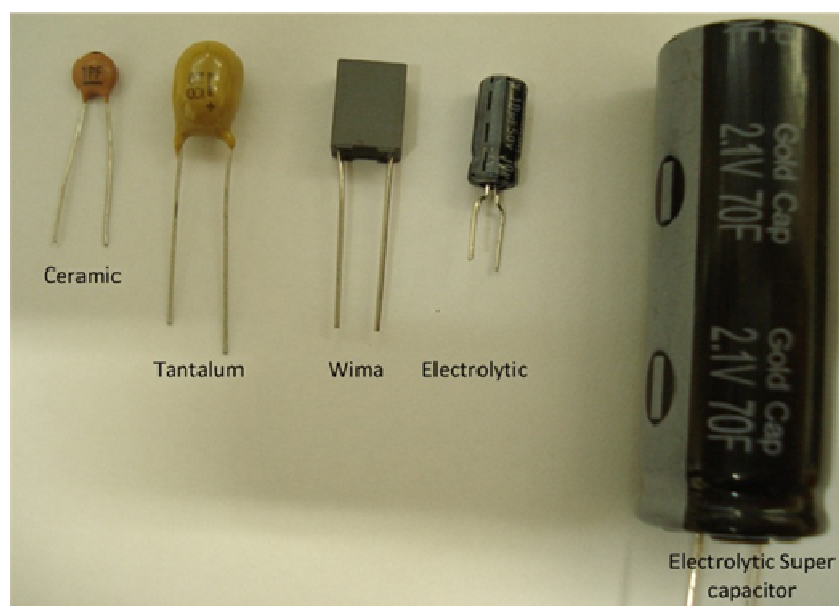


Figure 2-16 Some capacitor types and sizes

2.5.2.1 Supercapacitors

These capacitors are able to handle rapid and extreme changes in energy levels. When compared with batteries, supercapacitors have much lower energy densities, meaning that batteries have much longer run cycles. However, supercapacitors have higher power densities, meaning that they can be charged at high current levels without damaging their internal structure, and supply large currents in an instant, which batteries cannot (Johansson & Andersson, 2008).

This is because batteries rely on chemical reactions to produce and store energy, whereas capacitors use a process called charge separation. This causes capacitors to have longer life cycles than batteries which is very helpful when it comes to the maintenance of the device. Some information regarding the manufacturers and specifications of supercapacitors is shown in Table 2-5.

Table 2-5 Supercapacitors, their manufacturers and specifications (Sahay & Dwivedi, 2009)

Manufacturer	Specifications of Supercapacitors
Power Star China (Single Unit)	50F/ 2.7V, 300F/ 2.7 V, 600F/ 2.7 V, ESR less than 1 mΩ
Panasonic (Single Unit)	0.022 – 70F, 2.1 – 5.5 V, ESR 200 mΩ - 350 Ω
Maxwell (Module)	63F/ 125V, 150A ESR 18 mΩ 94F/ 75 V, 50A, ESR 15 mΩ
Vinatech	10 – 600F/ 2.3 V, ESR 400 – 20 mΩ, 3 – 350F/ 2.7 V, ESR 90 – 8 mΩ
Nesscap (Module)	15V/ 33F, ESR 27 mΩ 340V/ 51F, ESR 19 mΩ

Table 2-6 is an indication of capacitor development since 1996, giving some idea as to the costs of supercapacitors. This is done as the technology is fairly new and the associated costs are largely unknown, and more specifically to justify the use of this device as one of the aims of this study is to design the most cost-effective system.

Table 2-6 Supercapacitors, cost per Farad and KJ, as redrawn from (Sahay & Dwivedi, 2009)

Year	Cost/ Farad (\$)	Cost/ KJ (\$)
1996	0.75	281.55
1998	0.40	151.23
2000	0.01	32
2002	0.023	7.51
2006	0.01	2.85
2010	0.005	1.28

The associated power characteristics of the energy reservoirs considered for this study are graphically represented by Figure 2-17. The factors to consider when making a comparison are their energy densities and power densities. It can be seen by looking at the graph that batteries and fuel cells are able to supply energy over long periods of time, whereas capacitors and supercapacitors are able to supply large bursts of energy, but over shorter time periods.

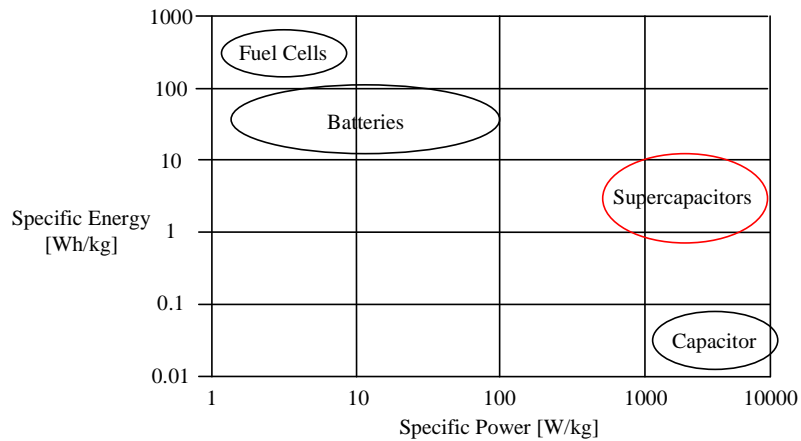


Figure 2-17 Energy and power properties of various power sources (Johansson & Andersson, 2008)

All the energy sources discussed in this section are able to energise the WSN. However, the ability to operate reliably over long periods of time in different environments is more important than the ability to last for a few days without being charged. This narrows the choice down to capacitors and supercapacitors. As the latter is able to supply an abundance of energy in a short period of time as well as provide a constant supply over a longer period of time, a supercapacitor will be used as the power reservoir for the WSN.

2.6 Energy harvesting techniques

2.6.1 Solar energy

Solar power is generated either from photovoltaic cells or by using the sun to heat up a liquid and converting this heat into energy. Liquid heating for energy generation is not normally implemented on a small scale; therefore, this section will focus on photovoltaic (or solar) cells. Solar cells operate on the basic principle of the photovoltaic effect.

A potential difference (voltage) develops when two types of material are joined (n-type emitter and p-type base) and this junction is exposed to light (photons). Light is absorbed by this junction and this energy is transferred to the electrons in the junction material. Charge carriers are then created which are separated at the junction of the two materials. These charge carriers are called electron-ion pairs when in an electrolyte and as electron-hole pairs when in a solid semi-conductive material (Patel, 2005).

An illustration of a photovoltaic cell is shown in Figure 2-18. Since the p- and n-junctions consist of semi-conductive material, electron-hole pairs are formed which are split into electrons and holes. The electrons are forced to the n-junction by the electric field generated by the metal contact, and the holes will stay at the p-junction. This forms a potential difference across the two materials, and when the n- and p-side is either short-circuited or a load is placed across the junction, a current will flow through the circuit, resulting in the electrons being reunited with the holes in a process that repeats itself (Flipsen, 2004).

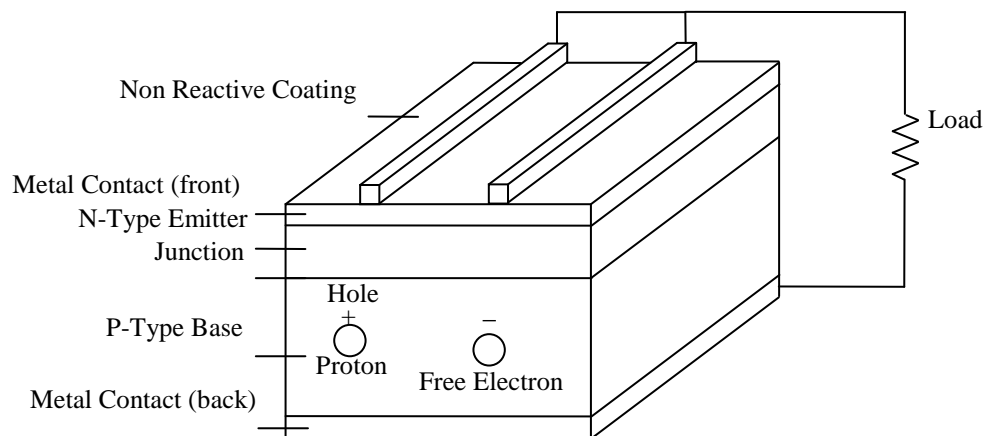


Figure 2-18 Solar photovoltaic cell, as redrawn from (Flipsen, 2004)

2.6.2 Wind energy

Modern day wind turbines operate on a similar principle to windmills, with the major difference being their ability to convert mechanical energy to electrical energy. The basic design of the wind turbine is based on the force that a volume of wind exerts on blades which causes them to start revolving. This rotation causes the shaft of the turbine to turn, and the associated kinetic energy is then converted to electrical energy.

The turbine is connected to a high speed shaft which derives its energy from a low speed shaft attached to a rotor. Due to an internal gearbox the shaft of the generator turns at a higher speed than the rotor. The problem with industrial wind turbines is their size, as they typically produce power in the megawatt range, with wing spans the size of a football field. However, there are smaller wind generators that produce in the region of tens of watts of power.

This relates to a current of around 1.4A when operating at full potential. This mini wind generator comprises three blades, spaced 120° apart, with a blade length of around 55cm (Shastalore, n.d.). This small-scale power generation is therefore a feasible option to be used in smaller applications. A cup anemometer can be used to measure the wind speed and harvest the wind energy. This is a relatively small device with an arm length of less than 10cm, making it a suitable device for mounting on the energy harvesting system(Shastalore, n.d.).

2.6.3 Vibration energy

The conversion of mechanical stress to electrical energy has been highly researched over the last decade. Piezoelectric materials generate an electric current when subjected to mechanical strain, known as the piezoelectric effect. One of the most common piezoelectric materials is polycrystalline, composed of randomly oriented crystallite. During its manufacture, this material is exposed to a large electric field which aligns the polar domains according to the orientation of the field, resulting in a macroscopic piezoelectricity. This causes the material to lengthen under an applied voltage or a voltage to be created under an applied mechanical stress (Roundy, 2003).

With the development of the piezoelectric cantilever, vibrations can now be converted to electrical energy. However, this technique would likely only harvest enough energy to power a WSN that is, for example, measuring temperature in a remote location with data transmission once a day (Townley, 2012).

2.6.4 Magnetic field energy

This concept is based on AC producing an alternating magnetic field which can be converted to electrical power via devices like CTs (Ahola, et al., 2008). As the CT was originally designed only as a metering device, the design must be adapted, allowing it to still accurately measure current while at the same time powering electronic circuitry. This technique will therefore have the benefit of fulfilling two required functions, i.e. measuring the phase current and acting as a low maintenance power source. In addition, its clamp-on ability allows for easy implementation (Ahola, et al., 2008).

CTs can deliver 12W of continuous power when supplied by a primary source of 100A, making it a suitable power source for the WSN. The implementation of a CT is shown in Figure 2-19.



Figure 2-19CT clamped onto a motor phase conductor(Ahola, et al., 2008)

2.6.5 Evaluation of energy harvesting techniques

Self-sustainable power sources have been discussed in this section as alternatives to the batteries typically used by WSNs. A comparison of these alternative power sources is shown in Table 2-7.

Table 2-7 Comparison between energy harvesting methods

Energy source	Solar	Wind	Piezoelectric	Magnetic
Source description	Solar panel	Wind Turbine	Cantilever with proof mass	Induction CT
Area needed for implementation	Small	Small to Large	Large	Small
Ease of installation	Moderately	Moderately	Moderately	Easy clamp on
Energy availability	Dependant on Seasons and Time of day	Dependant on Seasons	Dependant on Transformer load Transformer vibration	Transformer load
Maintenance	Little	High	Moderate	Little to none

It is obvious that solar energy is only sufficient during daylight hours, necessitating design considerations regarding the size of the solar panel and energy reservoir. A similar problem is presented by wind energy harvesting, as the energy source is not continuous and therefore unreliable.

It has therefore been decided to design an energy harvesting CT as the primary source of power to the WSN. As shown in Table 2-7, the energy harvesting CT is a small device which can easily be installed. Furthermore, it only has one variable when it comes to energy availability. Because the CT is dependent on the magnetic field around a current carrying conductor, the only major influence on the output power of the energy harvesting CT is the magnitude of the current in the primary conductor. Although this current may vary, the sustainability of this technique is far more reliable than its counterparts.

Wind turbines, for example, present an additional problem in their maintenance, as they are constructed of moving parts. If the mechanical side of this particular energy harvester were to fail, power would not be supplied to the WSN. CTs, however, do not have any moving parts, and therefore these devices are relatively maintenance free, making CTs a reliable energy source with an extended operational lifespan.

One consideration that must be kept in mind, however, is that the core of the CT must be properly aligned in order for optimum flux transfer to take place.

Energy harvesting CTs are therefore chosen as the power source for the WSN, due to all of the reasons mentioned above, and the abundance of magnetic field at the phase conductors of the transformer. The next chapter will focus on the design specifications for the monitoring system, including the relevant properties of the transformer to be monitored, and those of the energy harvesting and current measurement systems.

Chapter 3

Design considerations

Understanding the system structure is fundamentally important in the design process which makes use of first principles. First of all, the transformer to be monitored will be discussed, followed by the energy harvesting and current monitoring system.

3.1 The transformer

Based on the study done in the previous chapter, a 100kVA transformer has been selected, the technical specifications of which can be seen in Table 3-1. The design of the CT energy harvesting device in the section to follow will depend on the available power and usage pattern of the transformer.

Table 3-1PMT specifications(WBSEDCL, 2012)

Description	Specifications
Rated power	100kVA
Rated HV	11kV
Rated LV	433V
Connection HV, LV	Delta (Δ), Star (Y)
Flux density	1.55T
Current density	1.4A/sq.mm
Transformer losses	No load, 350W, Load, 1850W

3.1.1 Transformer current

Before energy harvesting is possible the line current of the transformer must be known. The secondary line current in the transformer or load current is shown by

$$I_{Load} = \frac{P}{\sqrt{3} * V_L} \quad (2)$$

The total secondary line current this transformer produces when operating at 100% capacity is 133A. However, transformers can operate at higher currents than their design specifications for short periods of time. With this in mind, the CT will be designed to withstand up to 125% of the rated transformer current, i.e. 166A per line.

3.1.2 Transformer cables

The secondary phase cables of distribution transformers are typically made of either copper, aluminium or silver, with the most common being copper. For CT design purposes, the cable dimensions must be known. According to (Mclyman, 2004), a general rule of thumb is used to determine the current density a specific cable can withstand, given by $J \approx 400\text{A}/\text{cm}^2$.

The diameter of the secondary phase cable of the transformer is shown by

$$d_{\text{Cable}} = \frac{I_{\text{load}}}{I_{\text{standard}}} \times \text{cm}^2 \quad (3)$$

A field inspection was conducted in order to observe the cable diameters used by utilities. It was found that the Matzikama Municipality uses 120mm² cables for their 200kVA transformers, meaning that these secondary phase cables can handle over 400A. This is considerably more than the 323A calculated above and indicates that extra precaution has been taken in the cable design for safety purposes. Hence, a clearance of 60mm² with the addition of insulation must be kept in mind when determining the size of the CT core for the 100kVA design.

3.2 The energy harvesting and current monitoring system

This system consists of two main building blocks. The first is the CT, used to convert magnetic fields into electrical energy, as well as provide a stepped down version of the transformer current for measurement purposes. The second is the electrical control and energy management circuit, used to guide the flow of energy and regulate the current measurements under pre-programmed conditions.

3.2.1 The CT

The CT is divided into five separate layers, which are explained below.

- Core material – the material properties control core magnetic flux handling capabilities.
- Current ratio – this determines the stepped down current and voltage of the CT.
- Core area – this controls the amount of flux transfer in the core.
- Saturation voltage – this relates to the ability of the magnetic field to produce operational voltage for energy harvesting.
- Performance – this evaluates the energy supply capability for sufficient power generation.

3.2.2 Electrical control and energy management

The electrical control and energy management circuit consist of seven separate layers – not including the CT source – which are explained below.

- Voltage conversion –the AC source is converted to a stable DC.
- Power regulation –the DC voltage is controlled for suitable charging capabilities.
- Power source – comprising units for energy storage.
- Voltage analysis – a decision making algorithm controlling energy harvesting current and measurements.
- Measurements – the current measurements are processed by the microprocessor and stored in the memory.
- Data transmission – the data packages are wirelessly transmitted to a receiving base station.
- Reception and analysis – data packages are received and analysed.

As shown in Figure 3-1, this system is in control of decision making parameters that are controlled by a pre-programmed microprocessor as well as integrated circuitry.

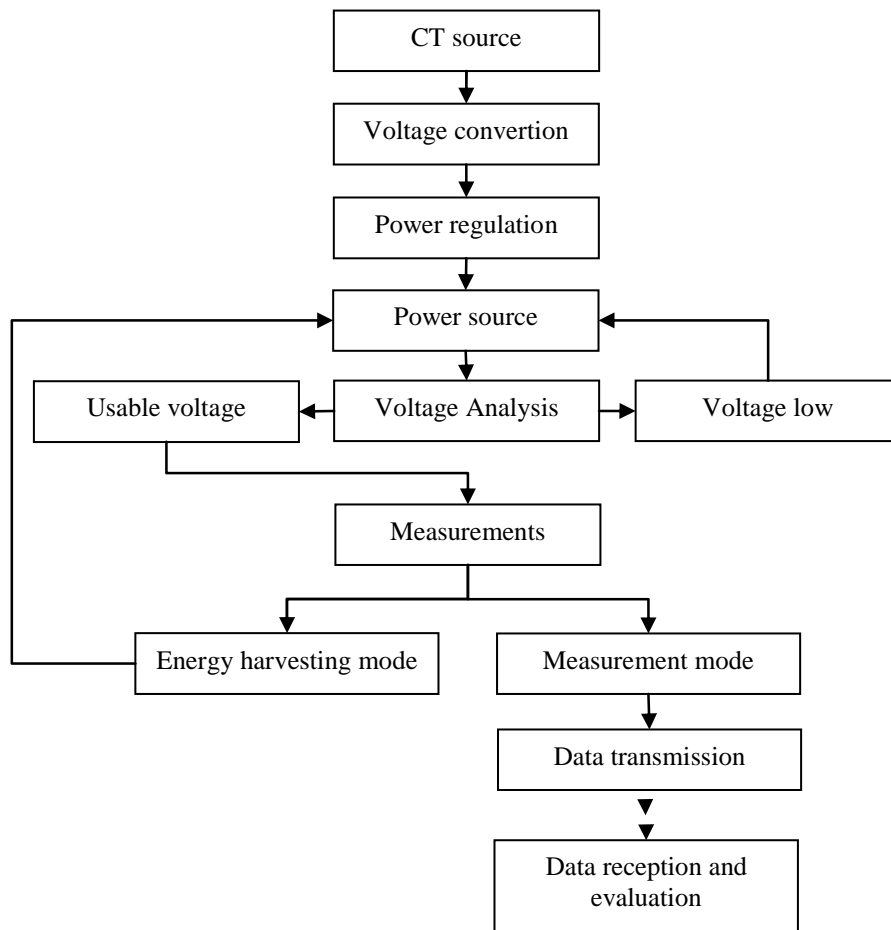


Figure 3-1 Block diagram of circuit for power management and current measurement

3.2.3 CT electrical specifications

The CT used for this application is not the same as a traditional CT used for the protection of industrial transformers at substations. It has two primary objectives – namely, to harvest enough power from a current carrying conductor to provide a continuous supply to a WSN, and to assist in the measurement of current.

The electrical design specifications of the CT, shown in Table 3-2, were obtained by means of South African power specifications, CT design specifications and further specifications determined by the topology.

Table 3-2CT Electrical design specifications

Description	Specifications
Supply Voltage (RMS)	433V
Supply Current (RMS)	5 – 200A
Load Voltage (Peak)	30V
Load Current (RMS)	5 – 200mA
Load Power (RMS)	2.5W (at Typical Supply current of 120A)
Primary Turns	1
Secondary Turns	1000
B_{max}	450mT
Frequency	50Hz
Efficiency	90%

3.2.4 Possible voltage and power expectations

The energy harvesting CT is expected to produce an output power of up to 2.5W and a peak operational voltage of 30V under optimum operating conditions. These conditions include optimum flux density in the transformer material, creating the highest voltage level before magnetic saturation occurs. Different loading conditions would result in different power and voltage outputs. Hence, if the device were to be heavily loaded, the power and voltage output would decrease.

In addition, the load impedance characteristics would change continuously as the microprocessor controls the energy harvesting, measurement and data transmission systems. During testing of the CT, a constant current is supplied to it at different loads. This shows how the power and voltage are influenced by a change in the load. Another factor affecting the power and voltage output of the device is the varying phase current levels of the transformer, making the estimation of the possible power and voltage outputs more complex.

3.2.5 Accuracy of current measurements

The accuracy of the current measurement device depends on the measurement technique used. As explained in the previous chapter, the average RMS calibration method is being used for current measurements. When a CT is subjected to sinusoidal waveforms, the results of the average RMS calibration method are expected to be the same as those obtained by true RMS measurements. However, the presence of harmonics in the PMT current distorts the sinusoidal wave to something resembling a sawtooth waveform. With this in mind, the CT will work with an error of 0 – 3.3% as shown in Table 2-2. Therefore, the accuracy of this device is specified to be within $\pm 5\%$. This will be put to the test when the finished product operates in typical field conditions.

Chapter 4

The current monitoring system

This chapter comprises three main sections. The first is based on the CT design, which discusses the magnetic properties, the development process and the testing phase of the CT. The second is based on the electronic development stage, which discusses the electronic circuit design, simulations, programming and calibration of the current measurement. The third is the final evaluation and testing phase of the device under laboratory conditions. A visual overview of the chapter is shown in Figure 4-1.

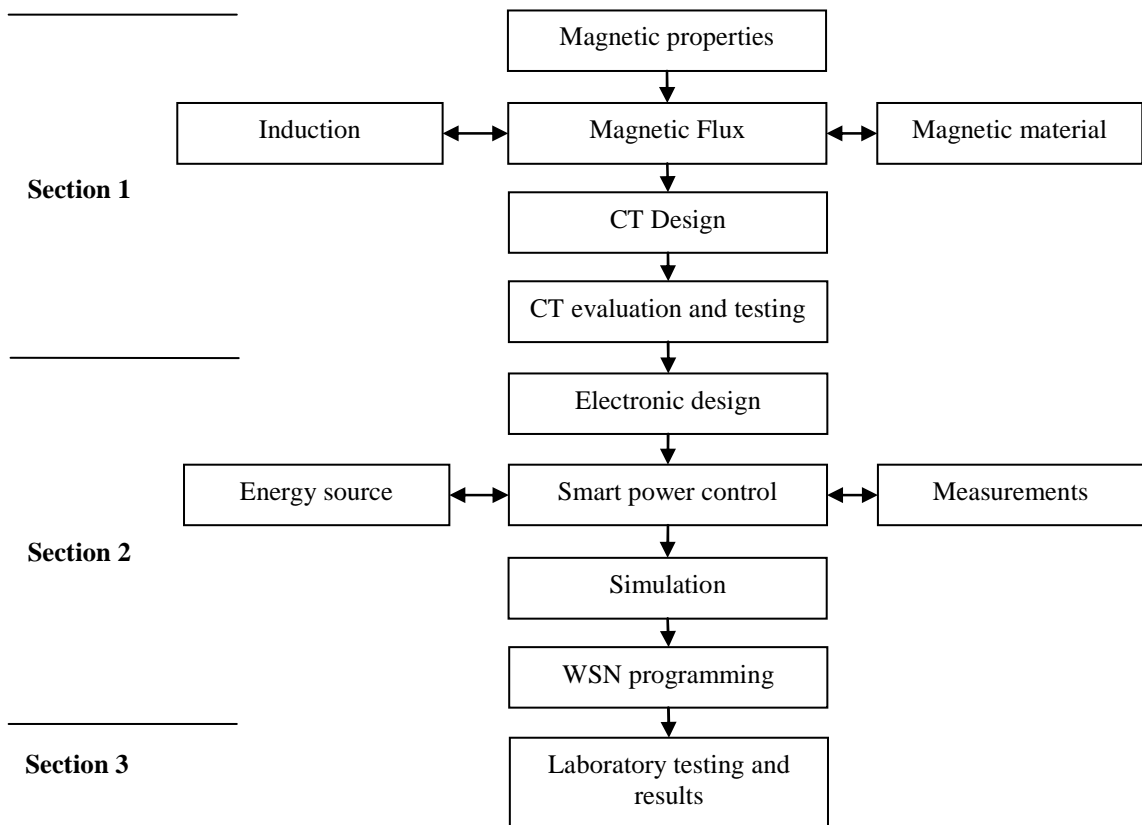


Figure 4-1 Overview of system structure leading to CT design

The following section will discuss the magnetic properties of the CT.

4.1 Electromagnetism

The magnetic field strength H is the magnetising force induced around a wire or surface that carries an electric current. This concept is illustrated in Figure 4-2.

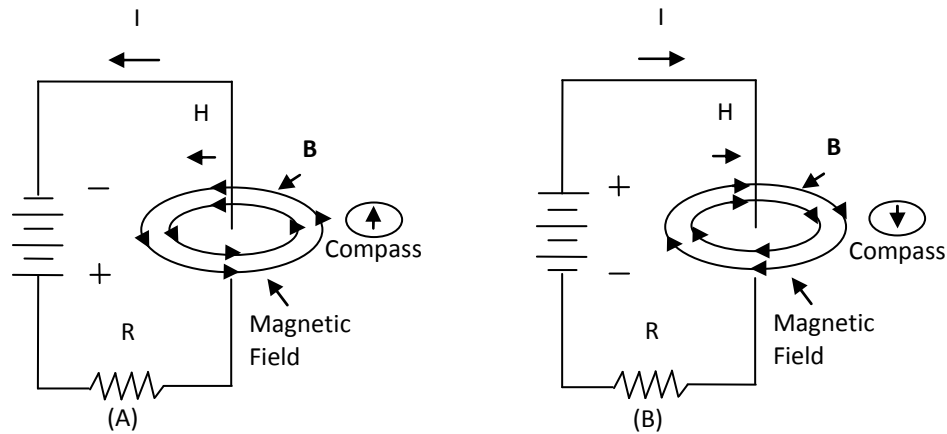


Figure 4-2 Magnetic field around current carrying wire, as redrawn from (Mclyman, 2004)

Figure 4-2(A) shows a DC source connected to a resistive load, producing current flow in the wire which in turn causes a magnetic field to be generated around it. By using the well-known right hand rule, it is clear that the direction of magnetisation changes direction when the DC excitation is reversed, causing the compass needle to deflect in the opposite direction, as shown in Figure 4-2(B). The magnetic field strength at a particular point is influenced by the magnitude of current that flows in the conductor as well as the distance this point is from the conductor surface. As the distance from the cable increases, the magnetic field weakens due to the flux lines being spaced further apart. Magnetic field strength is given by

$$H = \frac{I}{2 \pi r} \quad (4)$$

A magnetic circuit can be referred to as the space in which the magnetic flux is free to travel around the current carrying conductor. The field strength is determined by the amount of current and number of turns in the conductor. The flux density B is a product of the magnetic field strength and the permeability μ of the magnetic circuit, in this case μ_0 which is the permeability of air (Mclyman, 2004), given by

$$B = \mu_0 H \quad (5)$$

Therefore, μ_0 is the conversion factor between B and H, given by

$$\mu_0 = \frac{B}{H} \quad (6)$$

Figure 4-3 illustrates magnetic flux density B and total flux Φ enclosed by an area.

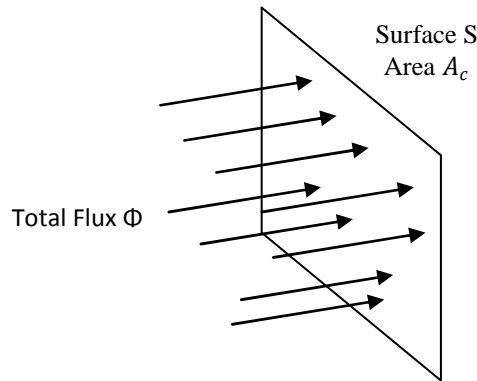


Figure 4-3 Flux density and total flux bounded by an area, as redrawn from (Erickson & Maksimović, 2004)

The total flux Φ can be seen as the amount of flux passing through a specific surface S of area A as illustrated in the above Figure. Therefore, it can be said that the total amount of flux passing through a surface is equal to the integral of the flux density over the specified surface dA, being the vector area element, given by

$$\Phi = \int_S B dA \quad (7)$$

The integral can simplify to a uniform flux distribution, given by

$$\Phi = BA \quad (8)$$

This shows that the total flux is equal to the flux density multiplied by the specified area. The flux density is linked to a change in current density J, and the total flux is linked to the current I. If a static current density of fixed magnitude passes through a given surface area, the current can be determined by (Erickson & Maksimović, 2004)

$$I = JA \quad (9)$$

The law of magnetic induction states that a current will be induced in a closed circuit if the circuit is subjected to a magnetic flux changing in time. This is also known as Faraday's law and is given by

$$\varepsilon = -\frac{d\Phi}{dt} \quad (10)$$

When a coil of wire is subjected to a changing flux, the formula is now given by

$$\varepsilon = -N\frac{d\Phi}{dt} \quad (11)$$

The reason for the negative sign in the above equation can be said to be due to Lenz's law, which states that the induced EMF in the circuit is directly opposed to the EMF that originally produced it.

4.1.1 Magnetic materials

Most materials have a very low permeability with regard to magnetic flux. Non-magnetic materials such as paper are regarded as having the same permeability as air or free space, i.e. 1. There are a few magnetic materials such as iron, nickel, cobalt and various alloys, such as steel, which have high permeabilities relative to that of air, some in the order of a few thousand. The air core in Figure 4-4 is used to transfer the flux from the first coil where it was generated to the second coil where it is used to induce an EMF. Magnetic field strength reduces in relation to $\frac{1}{r}$ so in order to counteract this reduction in field strength a magnetic core is placed inside the coil which acts as a pathway for the flux.

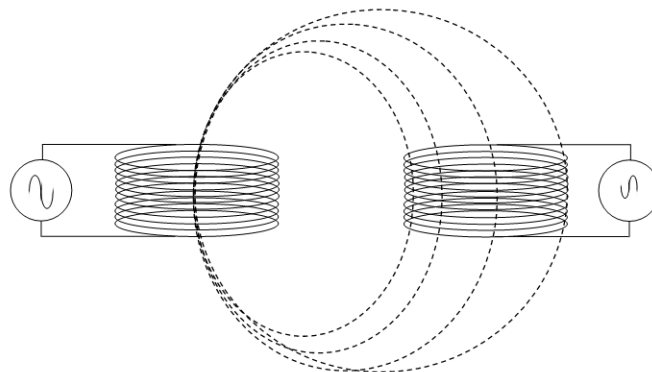


Figure 4-4 Magnetic field produced by an air core

As the induced voltage in the coil is linked to the magnetic field strength, by placing a magnetic core in the air gap this results in a better voltage, and therefore current, being generated by the flux (Mclyman, 2004). Figure 4-5 demonstrates what happens when a completely demagnetised core is then magnetised by a coil around it. The associated flux density B is measured as the magnetising force H is increased in small discrete steps, resulting in the B - H curve characteristic of the magnetic core material shown below. The point B on the curve is what is referred to as the knee point or the point where magnetic saturation begins to set in to the material. After this point has been reached the core is regarded as having the same permeability as air, as there is no more room for magnetic flux.

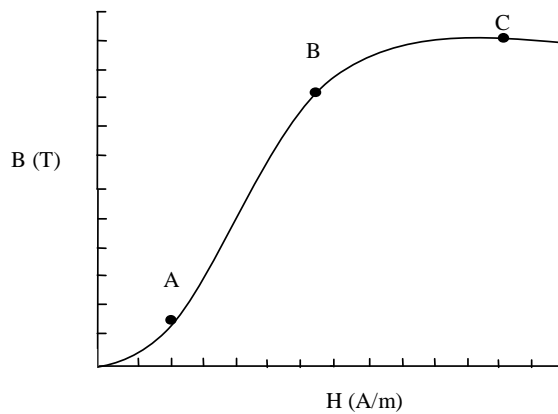


Figure 4-5 Magnetization curve, as redrawn from (Mclyman, 2004)

A cross section of a current carrying wire wrapped around a magnetic core is shown in Figure 4-6.

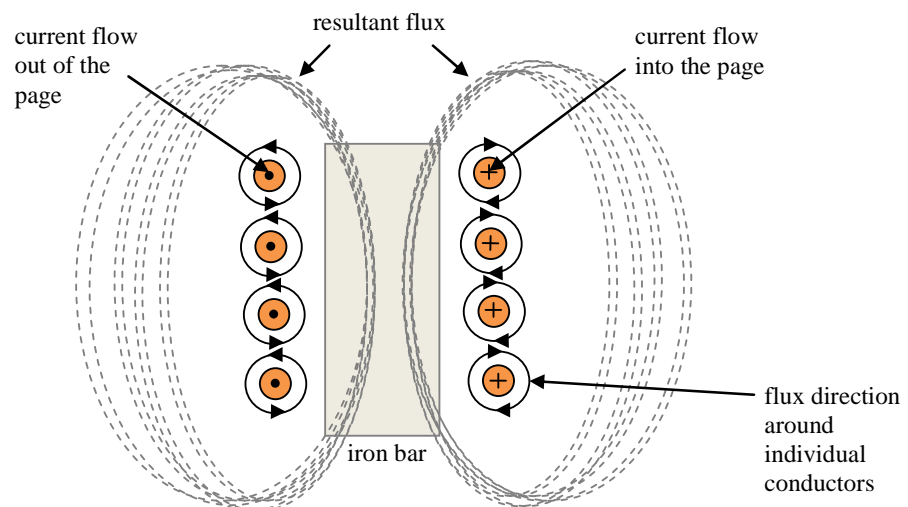


Figure 4-6 Flux in a magnetic core produced by a coil, as redrawn from (Mclyman, 2004)

When there is no core to guide the flux lines, they become spaced further apart from one another. This worsens as the distance increases from the conductors, thereby causing a reduction in field strength. Figure 4-7 shows why closed cores are used in transformer manufacturing, where the different magnetising stages of a square magnetic core with one wound limb can be seen.

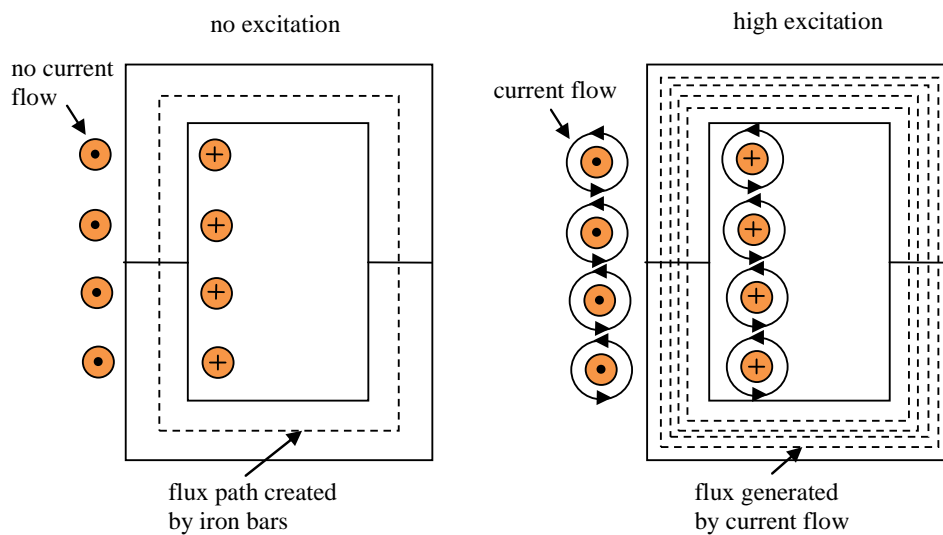


Figure 4-7 Different stages of magnetic core excitation, as redrawn from (Mclyman, 2004)

As soon as current flows in the wire, a magnetic field is generated around it which follows the path of the magnetic core. This represents a closed magnetic circuit. The solenoid shown in Figure 4-6 represents an open magnetic circuit, due to the flux lines exiting the core. In the closed circuit, the flux density remains constant throughout the length of the core and does not cause any reduction in the magnetising force, unlike the open circuit. It is shown that when no current flows in the conductors of the closed circuit, there is no flux in the core. When current flows, magnetising force is generated which produces flux in the core, becoming more dense as the force is increased, eventually resulting in magnetic saturation. The magnetising force can also be increased by increasing the number of turns in the coil.

4.2 CT design

This section focuses on a newly designed and developed CT, having the same measurement characteristics than that of a traditional CT; however, this design will enable power transfer to the WSN for wireless transformer monitoring purposes. Figure 4-8 illustrates the design procedure followed to produce a CT having the capability of energy harvesting as well as current measurement.

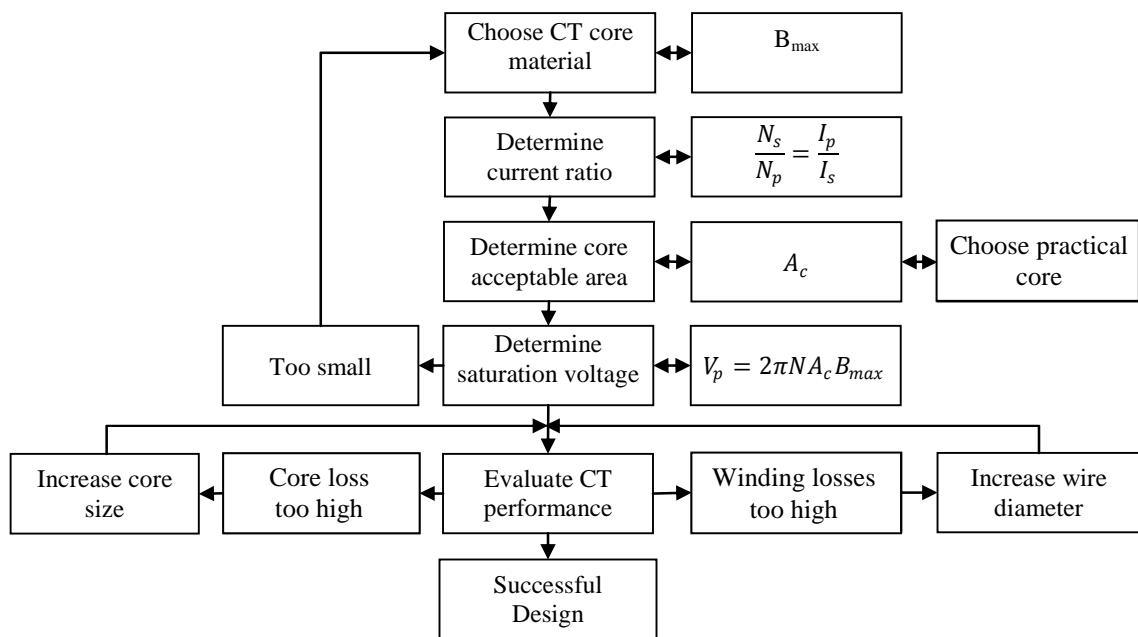


Figure 4-8CT design procedure

4.2.1 Core material

4.2.1.1 Permeability

A material's permeability rating is directly proportional to the ease at which the material can be magnetised at a given induction (Mclyman, 2004). The following equations show how permeability is calculated in terms of magnetic field strength and flux density.

$$\mu = \frac{B}{H} \quad (12)$$

$$\mu = \mu_r \mu_0 \quad (13)$$

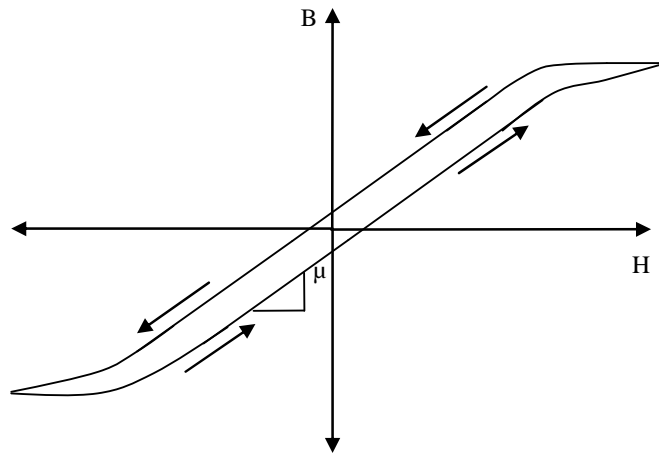


Figure 4-9 B-H characteristic curve of an iron core with sinusoidal excitation, as redrawn from (Erickson & Maksimović, 2004)

Figure 4-9 illustrates the B-H curve of iron when subjected to a high level of constant sinusoidal excitation. This shows that iron is nonlinear and experiences both hysteresis and saturation. As this is only a model, the shape is difficult to predict due to arbitrary waveforms which the iron may be subjected to. For theoretical purposes, the iron core in Figure 4-9 can be modelled by something called the linear or piecewise-linear characteristic. What this basically implies is that the iron core will still be subjected to the same magnetic environment but without hysteresis or saturation (Erickson & Maksimović, 2004).

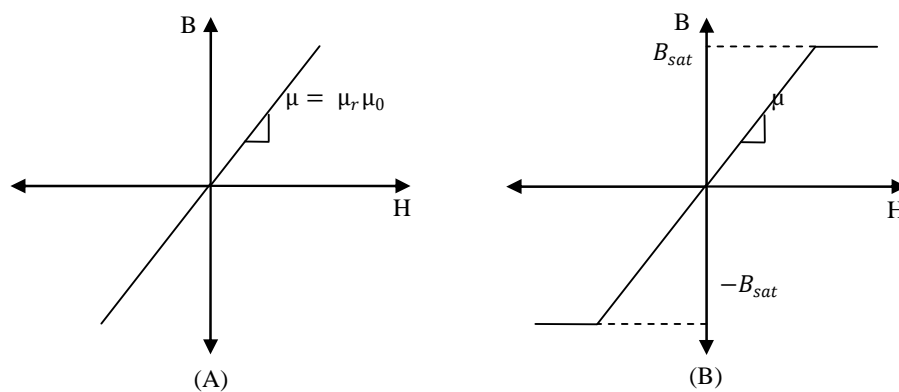


Figure 4-10 Estimated B-H characteristics of iron core (a) where hysteresis and saturation are neglected and (b) only hysteresis is neglected, as redrawn from (Erickson & Maksimović, 2004)

The permeability of core material varies and depends on the physical composition of the material. Softer materials tend to have higher levels of endurance with an increase in magnetic field strength, causing their permeability to decrease. Typical transformer cores are manufactured from silicon steel laminations. These types of metals can handle flux densities up to 2T. A powdered iron core's permeability is a bit higher than that of silicon steel, but can only handle up to 1T. Ferrite metals have high permeabilities but can typically only handle up to 0.5T. Their relative permeability values can range between 10^3 and 10^5 (Gupta, 1999). The B-H characteristics of ferromagnetic and soft ferrite material are shown in Figures 4-11 and 4-12 respectively.

CT core material plays a big role in the success of the transformers performance. The CT will not only be used for energy harvesting, but also to act as an instrument transformer, which requires exemplary accuracy. Therefore, the magnetising losses of the transformer must be kept to a minimum. For optimum design the H value on the B-H curve is important. The reason for this is that the material with the lowest value of H is most likely to produce the highest accuracy, because of minimal hysteresis losses.

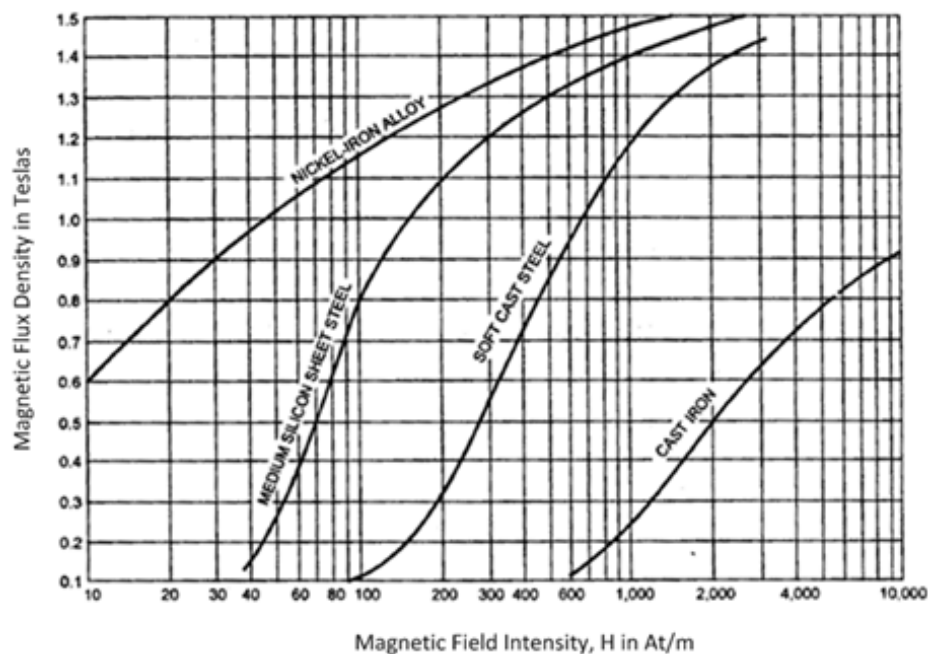


Figure 4-11B-H curve of ferromagnetic material(Gupta, 1999)

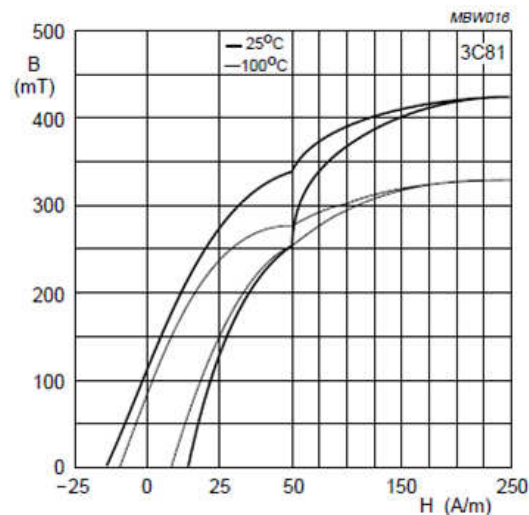


Figure 4-12 B-H curve of soft ferrite material (Ferrotec, 2012)

The material in Figure 4-11 is used in industrial distribution transformers; therefore it has high flux tolerances equivalent to or higher than 1.5T. The material in Figure 4-12 is typically used for high frequency applications, but can also be used in power applications at lower frequencies. The material in Figure 4-11 will magnetise at 40A/m whereas the material in Figure 4-12 will magnetise at 10 – 15A/m. Therefore, with the low magnetisation characteristics of the latter, a CT designed with this core material will be fairly accurate at low primary current values due to the low magnetising current required (Mclyman, 2004).

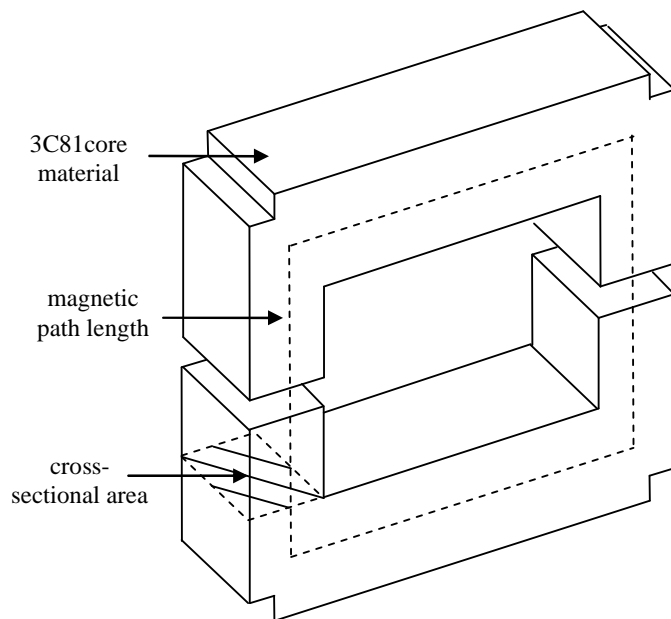


Figure 4-13 Illustration of CT core

The design criteria for a ferrite core material would require it to operate at a fairly low frequency for power transfer and be able to handle a wide range of currents without saturating. Therefore, the 3C81 material by Ferroxcube is chosen, having a relative permeability of 2570, a maximum flux density of 450mT and a magnetising force between 200 – 250A/m, which is relatively good for a ferrite material. The important characteristics of the CT core material will be calculated in the following section. Parameters like core permeability and minimum and maximum excitation current will determine whether or not this core will operate efficiently within the range of the primary transformer.

4.2.1.2 Permeability calculation

By performing these calculations it can be seen whether the supplier has provided the correct core material. According to Gupta (1999) the following calculations are used to determine the permeability of the 3C81 material provided by Ferroxcube.

$$B_g = \frac{F_g \times \mu_0}{l_g} \quad (14)$$

The flux density in the air gap of the CT with a given secondary current of 0.2A was calculated to be 1.361T (refer to Appendix A).

$$u_r = \frac{B_c \times l_{MP}}{u_0 \times F_c} \quad (15)$$

The relative permeability of the 3C81 core material was calculated to be 2677. According to the Ferroxcube datasheet, the relative permeability is 2700, hence, neglecting tolerances, the calculation holds true (refer to Appendix A).

4.2.1.3 Saturation and hysteresis

Hysteresis describes the energy lost in a magnetic core during magnetisation and demagnetisation. The most practical way of illustrating hysteresis losses is by conducting a field test, where a hysteresis loop will be plotted. This loop is generated by subjecting the core under test to a DC current, exerting a magnetising force on the core.

A typical hysteresis loop is shown in Figure 4-14, where the enclosed area is a measure of the total energy lost due to the properties of the core material during the magnetisation cycle(Mclyman, 2004).

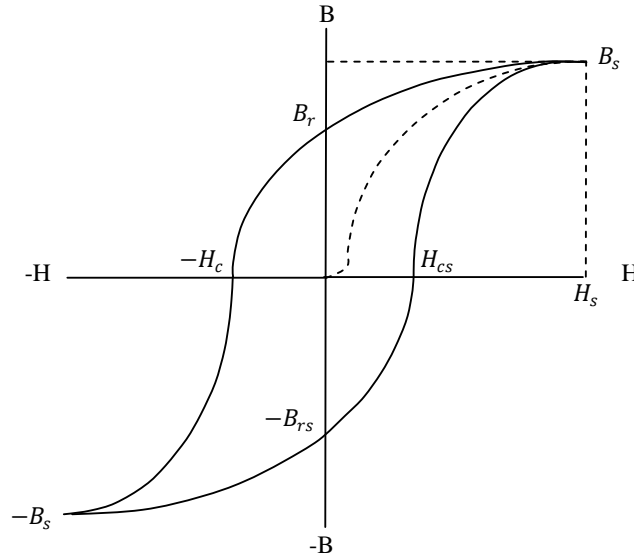


Figure 4-14 Hysteresis loop, as redrawn from(Mclyman, 2004)

When a magnetic core such as in Figure 4-13 undergoes a complete magnetising cycle, it is driven up to its positive as well as its negative saturation point. A neutral magnetic core is used for the test that is wound with a conductor, where the DC current is gradually increased, resulting in an increase in H . The corresponding increase in B is then plotted by the dashed line as indicated in Figure 4-14, until the maximum value is reached at B_s , being the positive saturation point. When H is decreased, the corresponding decrease in B does not follow the same curve as was plotted for the increase. This indicates that when H reaches zero the core is still magnetised, indicated by B_r on the graph which is referred to as the remanent flux. By reversing the polarity of H the coercive force does reduce B_r to zero, indicated by $-H_c$ on the graph, and by further decreasing H the core will once again be forced into saturation, indicated by $-B_s$ on the graph (Mclyman, 2004).

4.2.2 CT circuit analysis

A typical distribution transformer is shown in Figure 4-15, where N_1 is the primary and N_2 the secondary side of the transformer. When loading the transformer, current is supplied to the primary winding, generating an alternating magnetic field around the secondary winding, which induces a secondary voltage. When a load is connected across the secondary terminals, a current will flow in the secondary circuit. If an additional transformer is attached to the secondary winding, the same process will transfer energy to this transformer, which is the CT.

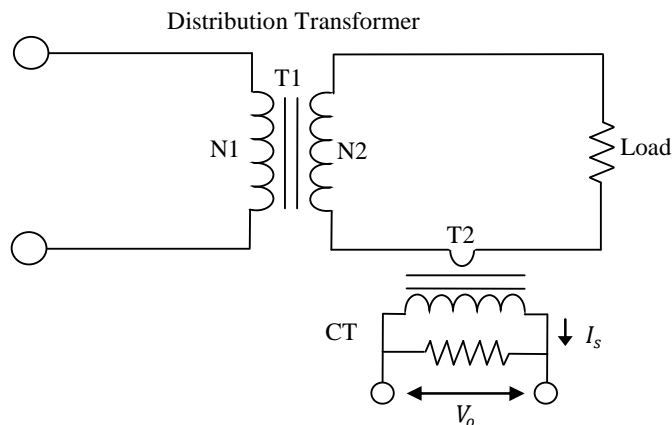


Figure 4-15 Secondary AC monitoring system, as redrawn from (Mclyman, 2004)

The equivalent circuit in Figure 4-16 is used to explain the key elements of the CT.

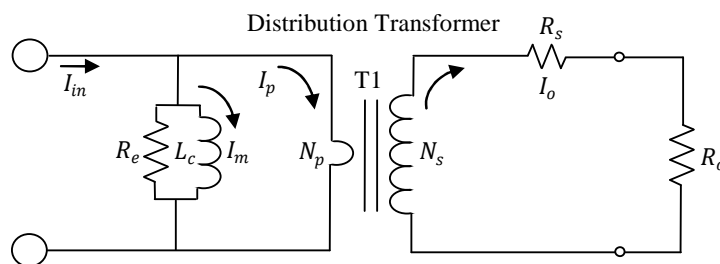


Figure 4-16 Equivalent circuit of CT redrawn from (Mclyman, 2004)

The input current is separated into two components – namely, I_m and I_p . The primary current I_p and primary turns N_p are responsible for driving the flux around the CT core. The ampere-turns $I_m N_p$ ensure maximum power transfer across the device. The magnetising current I_m and primary winding N_p are responsible for the losses in the core, represented by the magnetising ampere-turns $I_m N_p$ (Mclyman, 2004).

The magnetising current has a substantial influence on the efficiency of the transformer, being the portion of the primary current responsible for hysteresis and eddy current losses (Mclyman, 2004). Low core permeability influences the resistive and inductive components of the circuit, causing them to be low and the core loss to be high. A high core loss results in poor flux transfer, and only a portion of I_{in} will reach R_o (Mclyman, 2004). The following equation indicates the role that permeability plays on the inductance of the circuit.

$$L = \frac{0.4\pi N^2 A_c}{\ell_{MP} \times 10^8} \quad (16)$$

Therefore, an increase in core permeability is directly proportional to an increase in inductance, which effectively has a direct influence on the core losses. A simplified equivalent circuit is shown in Figure 4-17.

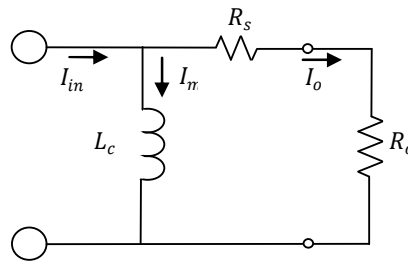


Figure 4-17 Relation between input and output current, as redrawn from (Mclyman, 2004)

By analysing the circuit in Figure 4-17, it can be seen that I_m is used to excite the core, and therefore the remainder of I_{in} (I_o) will be used to supply the load. To ensure the most efficient operation of the CT core, the magnetising current should be as low as possible. According to (Mclyman, 2004) this parameter can be determined by

$$I_m = \frac{H \ell_{MP}}{0.4\pi.N} \quad (17)$$

This gives the current required to magnetise the 3C81 ferrite material as 2.064A, meaning that the ℓ_{MP} requires a minimum secondary phase current of 2.064A before accurate measurements can be taken by the CT (refer to Appendix A).

According to (Gupta, 1999) the following equations can be used to determine the remaining key parameters of the 3C81 ferrite material.

$$B_{max} = \frac{\Phi}{A_c} \quad (18)$$

This gives the total flux in the CT core as 9.33×10^{-5} Wb (refer to Appendix A). The total magnetic reluctance \mathfrak{R} of the core can now be calculated, according to

$$\mathfrak{R} = \frac{\ell_{MP}}{\mu_0 \mu_r A_c} \quad (20)$$

This gives the total reluctance of the CT core as 1.169×10^6 At/Wb (refer to Appendix A) from which the MMF can now be calculated, according to

$$\Phi = \frac{\mathcal{F}}{\mathfrak{R}} \quad (21)$$

This gives the MMF in the magnetic circuit as 109.12At, which leads to the saturation current I_{sat} being calculated, according to

$$I_{sat} = \frac{\mathcal{F}_f}{N} \quad (22)$$

The primary side of the CT is a single cable, meaning that when a current of 109.12A flows in the secondary winding of the PMT, a flux of density 450mT will be produced in the core of the CT (refer to Appendix A).

4.2.3 Current ratio

The chosen current ratio is 1000:1. This will provide adequate voltage generation, and influence the size of the core as the number of secondary turns introduces a scaling factor with regard to the conductor diameter.

4.2.4 Core area

According to Wagener (2009) the following equation can be used to determine the core area, which is derived from Faraday's equation for electromagnetic induction.

$$A_c \cdot N_s = \frac{V_p}{2\pi F B_{max}} \quad (23)$$

When N_s is chosen as one, meaning that one primary and one secondary turn is used, the peak voltage V_p becomes 30V, which gives a core cross-sectional area A_c of 0.2122m^2 . If N_s is changed to a thousand turns this causes A_c to reduce to 212mm^2 .

Once this is known, a practical core size can be selected. As a clamp-on CT will be used, this simplifies the installation process and provides galvanic isolation, preventing any hazardous contact with the primary source. It was therefore decided to use a U core for the CT design, and it was found that Ferroxcube supplies U cores that are very close to the calculated A_c value. The chosen U core – namely, the U67/27/14 core, has a cross-sectional area of 204mm^2 (refer to Appendix A). This core is smaller than the calculated value, but is the closest available size.

4.2.5 Saturation voltage

In order to achieve the most accurate measurements, the secondary side of the CT must remain under the saturation voltage. The following calculation is done to determine the saturation voltage—associated with the core size, core material and operating frequency.

$$V_p = 2\pi F B_{max} A_c N_s \quad (24)$$

This gives a peak AC saturation voltage of 28.8V (refer to Appendix A).

4.2.6 Power output

Here an experiment is done to determine the power characteristics of the 3C81 ferrite core CT. Three different transformers were wound with three different wire diameters, 29, 27 and 25 AWG (American wire gauge), respectively. Once the CT was constructed, a test rig was built to generate the same amount of flux that it would be exposed to when operating in the field. The rig, illustrated in Figure 4-18, simulates a current flow of 120A rms, which is equivalent to a typical secondary current of a 100kVA transformer.

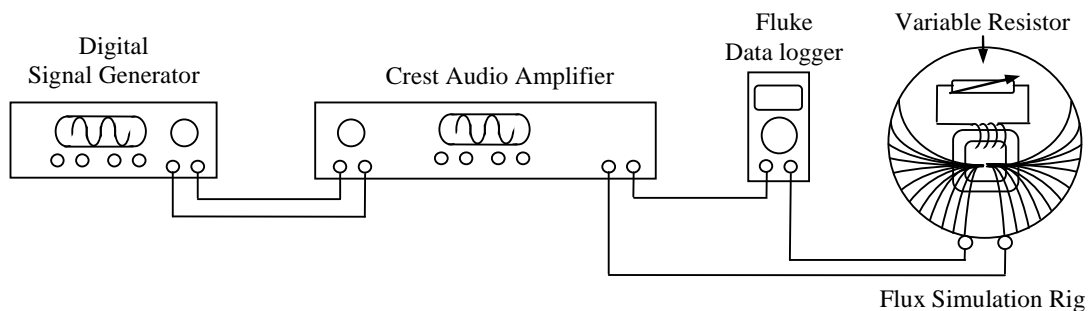


Figure 4-18 Current simulation rig

A 50Hz sinusoidal signal is generated by the digital signal generator, which is used as it has the ability to adjust the amplitude of the sinusoidal signal in small precise increments. However, it does not have the ability to deliver a high current magnitude; therefore, the signal is fed into a Crest audio amplifier. The Fluke data logger is used to monitor the accuracy of system parameters. The flux simulation rig is a flat, circular structure with copper wire looped from outside to inside, comprised of a total of forty loops. This number of turns reduces the primary current in the circuit. As the number of windings affects the amount of flux generated, the simulated primary current can be divided by a factor of forty. The CT will be tested with a primary current of 120A according to the secondary phase current of 120A in a 100kVA distribution transformer. This means that the flux simulation rig must be supplied with 3A.

In order to determine the power output of the CT cores, a variable load is connected to the output terminals of the CT. To monitor this operation, an oscilloscope is used to measure the voltage across a 1Ω resistor (connected in series with the load) as well as the current through it. The math function of the oscilloscope is then used to generate a power waveform.

By increasing the load from 1Ω to 1kΩ, the saturation point as well as the maximum power output of the CT can be determined. The following equation is used to determine the theoretical power output of the CT.

$$P_{o(rms)} = (V_{o(rms)} \cdot I_{o(rms)}) \quad (25)$$

This gives a theoretical power output of 2.5W with a peak voltage of 30V (21.2V rms) and output current of 120mA.

This result is then compared to results obtained by the current simulation tests. Figures 4-19 and 4-20 are screenshots taken from the oscilloscope used to monitor these tests. Figure 4-19 is the measurement done when the CT was subjected to a primary current of 120A rms. The load was then increased to 170Ω which is the point just below saturation, showing that the CT can produce a power output of 2.195W before becoming saturated. This is below the theoretically calculated value of 2.45W, which was due to early saturation of the core. Figure 4-20 is a screen shot taken when the CT was loaded with 390Ω. Here the voltage and current waveforms are completely saturated.

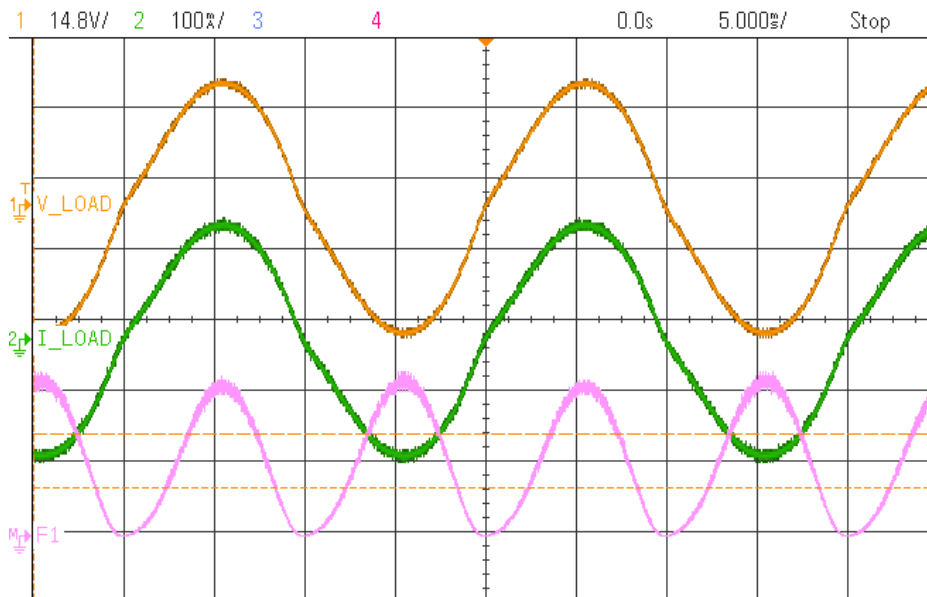


Figure 4-19 Measured voltage (V_LOAD), current (I_LOAD) and power (F1) before CT saturation

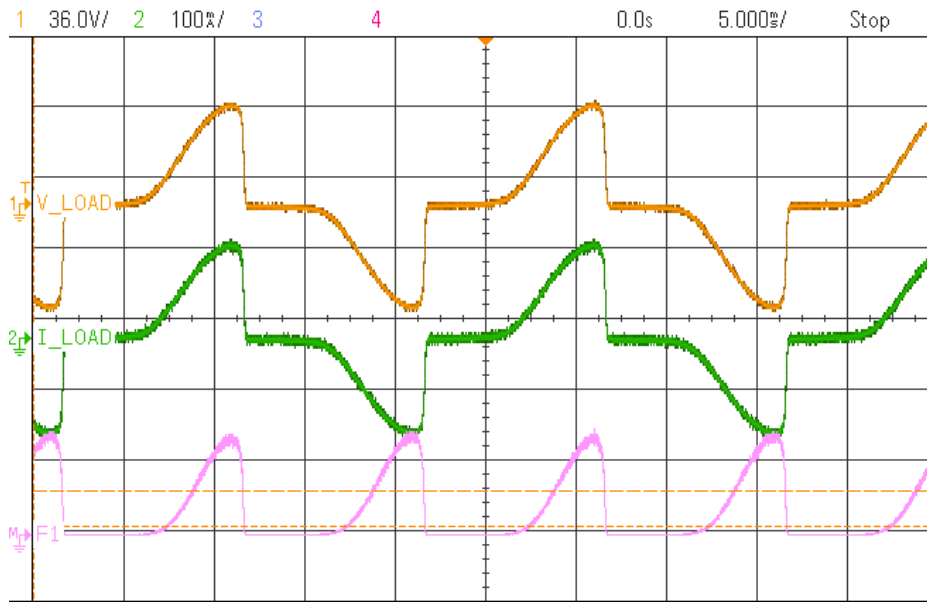


Figure 4-20 Measured voltage (V_LOAD), current (I_LOAD) and power ($F1$) at maximum power

4.2.7 Core losses

This section is a theoretical indication of the power loss in the CT core during energy harvesting and current measurement, according to (Mclyman, 2004). The following calculations only hold true when the CT is wound with 25 AWG wire. A core loss above five percent of the total power is considered to render the CT as inefficient for this application. This leads to the total core loss being not more than 122.4mW before saturation (refer to Appendix A). The following equation is used to calculate the allowable core loss of the CT.

$$LOSS_{mW/g} = \frac{P_{ce}}{W_{tfe}} \quad (26)$$

In order to determine the maximum loss in the core, one must first calculate the maximum flux density when the core is operating at peak voltage. Therefore, according to (Wagener, 2009) the following calculation is used.

$$B_{max} = \frac{V_p}{2\pi FN_s A_c} \quad (27)$$

The CT under test can operate at a peak voltage of 27.238V before saturation (refer to Appendix A), with associated flux densities of 425mT before saturation. Now that the flux densities at specific operating voltages are known, the theoretical power loss during operation can be calculated by using the following equation, according to (Mclyman, 2004).

$$Loss_{mW/g} = 0.000179 F^{1.48} B_{max}^{2.15} \quad (28)$$

The theoretical core losses that will occur during typical operation is 0.0093mW/g before core saturation (refer to Appendix A). The total core losses can then be calculated by the following equation, according to Mclyman (2004).

$$P_c = Wtfe \times Loss_{mW/g} \quad (29)$$

The total power loss in the core was calculated to be 1.58mW before saturation (refer to Appendix A). A maximum power loss of five percent was considered to be acceptable. According to the above calculations, the 3C81 ferrite core causes 0.072% of the total power to be lost before saturation. It is concluded then that this material will be highly efficient for use in the energy harvesting and current measurement application for which it is required.

4.2.8 Copper losses

According to (Mclyman, 2004), a 1cm² copper conductor can safely carry 400A, which is therefore the foundation for the following calculations. As the maximum secondary phase current of the distribution transformer is 200A, and the winding ratio of the CT is 1000:1, the current in the secondary winding of the CT is therefore 200mA, which will be used to determine the size of winding conductor. It was calculated that a 1mm² copper conductor (17 AWG) can safely carry 4A (refer to APPENDIX A).

A conductor required to carry 200mA will therefore have A_c 0.05mm² (30 AWG). However, to minimise heat dissipation by the conductor, A_c will be increased, giving a cross-sectional area of 0.064mm² (29 AWG).

For testing purposes, it was decided to wind three CTs with 25, 27 and 29 AWG conductor, which can safely carry 0.649A, 0.408A and 0.256A, respectively (refer to Appendix A).

The calculation of winding resistance will indicate whether the core is wound correctly and whether the correct size conductor has been used. The main reason this is done, however, is to determine the I²R losses for the CT. According to (Mclyman, 2004)the following equation is used to calculate the winding resistance.

$$R_s = \ell_{MTL} \times N \times \frac{\Omega}{\text{km}} \quad (30)$$

This gives a resistance of 6.221Ω for the 25 AWG conductor (refer to Appendix A) while the measured resistance of this conductor is 9.2Ω. A small cross-sectional area and long length of conductor results in a large resistance; therefore, the conductor must be as thick as possible to keep the winding resistance to a minimum. The following equation is used to determine the winding loss.

$$P_{cu} = (I_s)^2 \times R_s \quad (31)$$

This gives a total power loss in the windings of 132mW (refer to Appendix A).

4.2.9 Input power

In order to determine the efficiency of the CT, the input power is calculated according to (Mclyman, 2004)as

$$P_{in} = P_{cu} + P_{fe} + P_o \quad (32)$$

This gives the input power of the CT as 2.316W (refer to Appendix A).

4.2.10 Efficiency

By dividing the total output power of the CT by the total input power, the total core and winding loss can be seen as a percentage of the total power. According to (Mclyman, 2004) the following equation is used to determine the total efficiency.

$$\eta = \left(\frac{P_o}{P_{in}}\right) \times 100 \quad (33)$$

This gives an efficiency of 94.77% before saturation (refer to Appendix A). Figure 4-21 shows the efficiency of the CT plotted against the output power. The higher the load resistance of the CT, the more efficient it becomes.

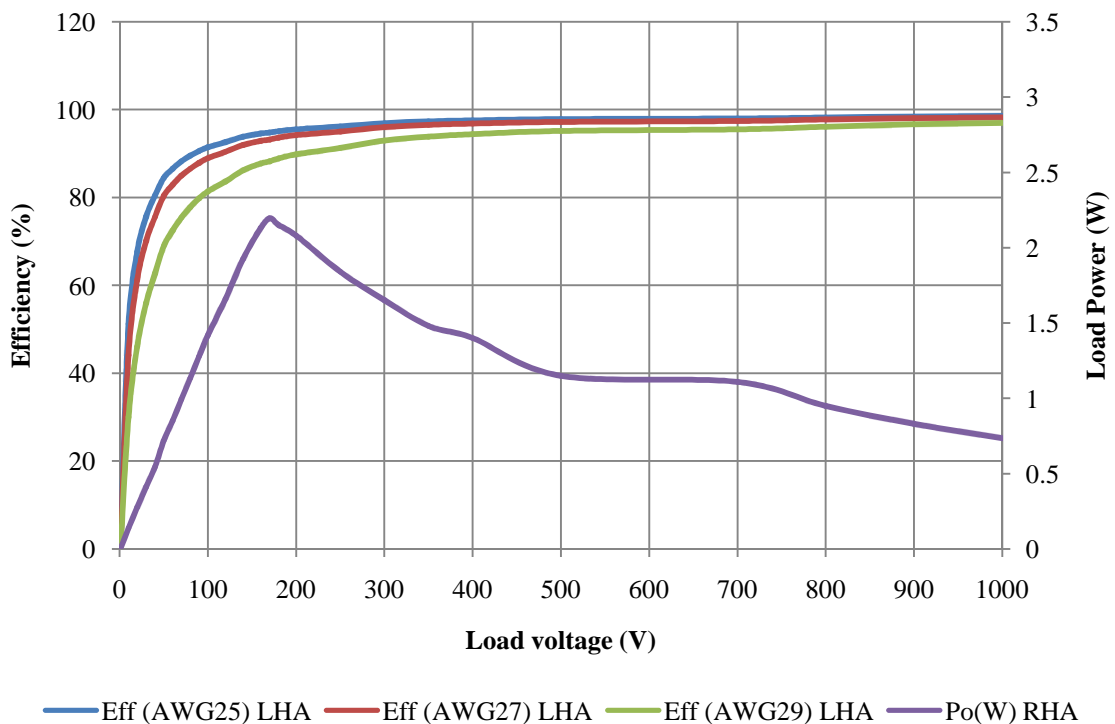


Figure 4-21 Calculated efficiency of CT

The design process was repeated to see what effect different conductor diameters will have on the CT. The same tests are therefore done on 25 AWG, 27 AWG and 29 AWG, respectively, using firstly 1Ω increments from 1Ω to 300Ω, and secondly 20Ω increments from 300Ω to 1kΩ. The results of these tests are shown in the following graphs.

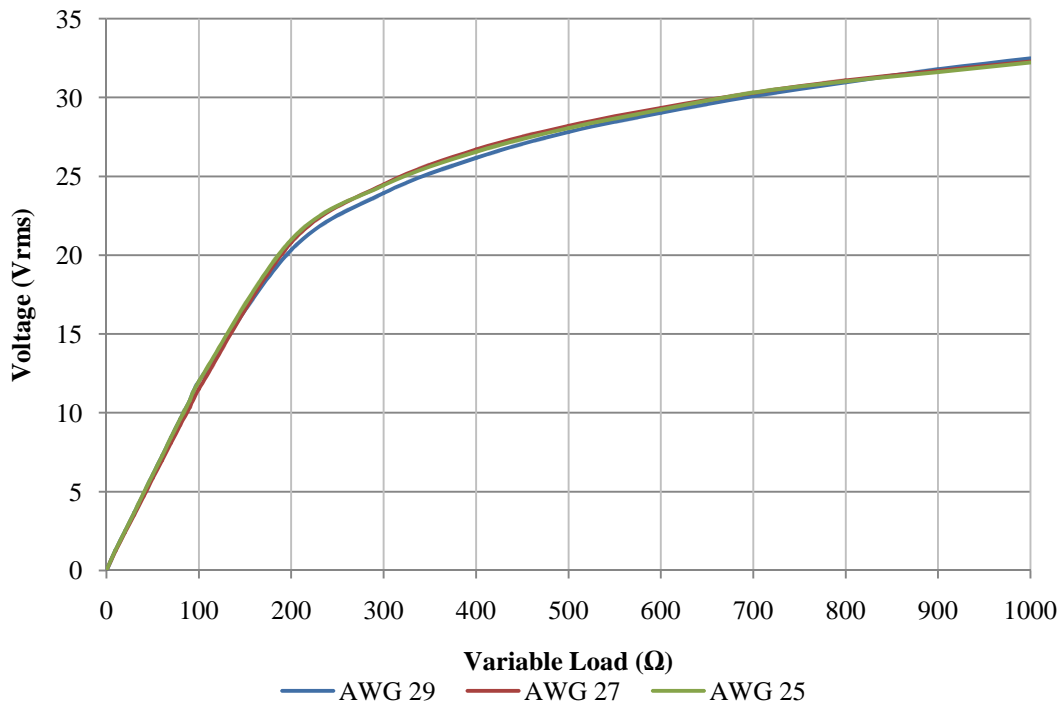


Figure 4-22 Voltage delivered by CT with change in load resistance with 120A primary current for different secondary wire gauges

Figure 4-22 shows the voltages generated by the three CTs under test. This illustrates that the wire diameter does not have a significant effect on the voltage. However, oscilloscope measurements indicate that when the transformers are operating at maximum power output, the voltages are 26.65V_{rms} (25 AWG), 27.26V_{rms} (27 AWG) and 26.19V_{rms} (29 AWG). These output voltages are relatively close, indicating that the CTs have been wound correctly; however, all of these voltages should theoretically be the same.

The difference in voltages can be attributed to various factors. According to (Wagener, 2009) the peak voltage is determined by a product of B_{max} and A_c as well as N . If the core permeabilities and cross-sectional areas are not identical, this will cause a difference in output voltages. The number of turns around each core also plays a role, this could make a significant contribution as the cores were wound by hand, introducing the possibility of human error.

Figure 4-23 shows the current outputs of the CTs when energised by a total flux associated with a current flow of $120A_{rms}$, as previously explained. With one thousand secondary turns, the CTs should theoretically produce a secondary current of $120mA_{rms}$. By looking at Figure 4-23, it can be seen that the output current changes in proportion to a change in load resistance. It was noticed that when the cores began to saturate, the output waveforms started to deform, resulting in only a portion of the original current being able to be measured. This can also be seen when looking at Figures 4-19 and 4-20. Therefore, in order to achieve accurate CT measurements, the load resistance across the CT must be as low as possible. This is discussed further in the electronic design section.

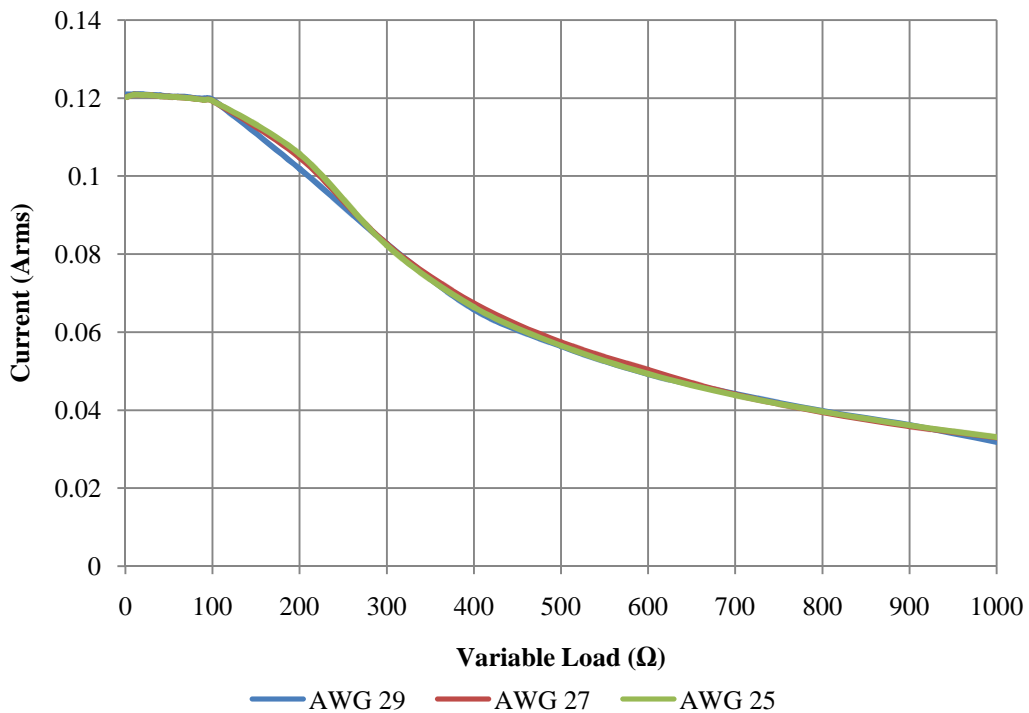


Figure 4-23 CT current output linked to changes in load resistance with $120A$ primary current for different secondary wire gauges

Figure 4-24 shows the power output of the CTs with different wire diameters. As expected, the 25 AWG performed the best because of low winding losses. This results in a power output of around $2.5W$ which is more than adequate to power the WSN in its operational state. Hence the design of the CT is considered to be a success.

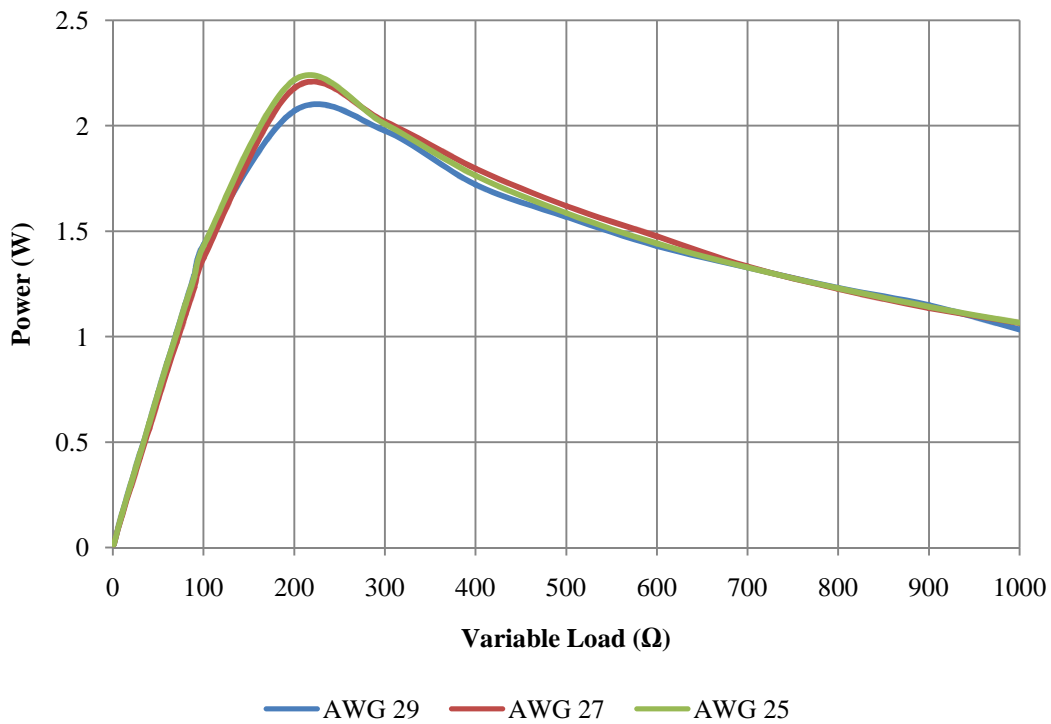


Figure 4-24 CT power output linked to changes in load resistance with 120A primary current for different secondary wire gauges

All the characteristics of the three CTs under test are shown in Table 4-1 with emphasis placed on their efficiency (the calculations can be found in Appendix A). Theoretically, the CTs wound with the thinnest conductor should have the lowest efficiency, according to the associated I^2R losses. The efficiency is seen to change with a change in conductor diameter – from 88.19% (29 AWG) to 94.77% (25 AWG).

Table 4-1 CT performance characteristics

AWG wires under test	29 AWG	27 AWG	25 AWG
Ω per Km	268.402Ω	168.821Ω	106.173Ω
Wire cost	5.61 \$/Kg	5.35 \$/Kg	5.12 \$/Kg
CT calculated impedance	15.72Ω	9.81Ω	6.221Ω
CT measured impedance	22.5Ω	12.2Ω	9.2Ω
Current handling capability	0.256A	0.408A	0.649A
P_{out} before saturation	2.071W	2.178W	2.217W
Efficiency before saturation	81%	89.56%	92.11%
Efficiency after saturation	88.18%	93.20%	94.77%

4.3 Electronic design

The CT designed in the previous section cannot function as a standalone unit. It needs electronic circuitry to convert the harvested power into a usable form to power the additional circuitry. This circuitry will be used to take the current measurements as well as wirelessly transmit the gathered information. The focus of this section is therefore on the development of the electronic circuit, with the design broken down into subsections for ease of explanation. A flow diagram of this process is shown in Figure 4-25.

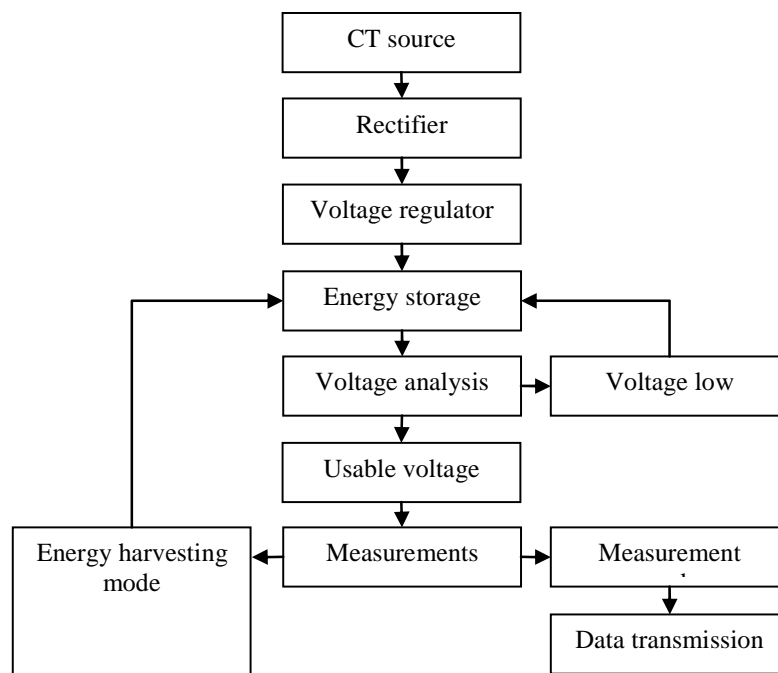


Figure 4-25 Design process for the electronic circuit

4.3.1 The rectifier

For the AC to DC conversion, it was decided not to use the traditional single unit bridge rectifiers, as these units exhibited a high voltage drop across the individual diodes. The AC source CT voltage is reliant on the primary current provided by the PMT. As this voltage can drop significantly, a decision was made to construct a full bridge rectifier, using PMEG201BEA Schottky diodes. These are used because of their low forward voltage drop (V_F) of between 280 – 330mV when operating at 120mA, and continuous forward current (I_F) of 1A. Therefore, in the event of a current spike, the diodes will not suffer any damage.

4.3.2 The voltage regulator

A voltage regulator must be implemented in the design in order to produce a stable and accurate voltage output for the energy storage unit. This is illustrated in Figure 4-26. The voltage needs to be precise in order to ensure that the WSN node will not be subjected to a voltage higher than its maximum of 3.6V DC.

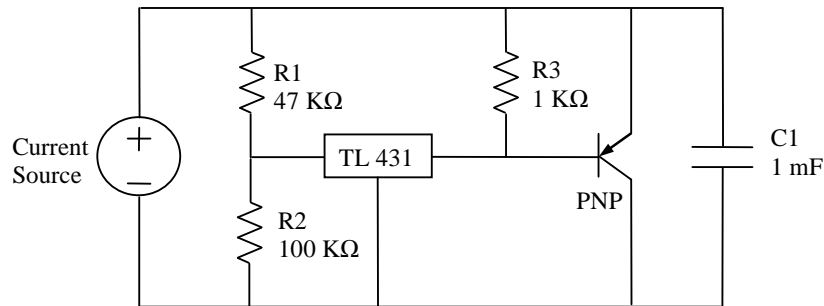


Figure 4-26 High current shunt regulator, as redrawn from (Texas Instruments, 2004)

The TL431CLP adjustable precision shunt regulator is used to regulate the output voltage of the CT. This is a three terminal device which regulates the output voltage to the load via a PNP transistor to between 2.5 – 3.6V, depending on the ratio of the resistors $R1$ and $R2$ and the reference voltage V_{ref} . If the voltage rises above the maximum output voltage, the transistor switches to sink current. A capacitor is used as the energy storage unit which is charged to the required output voltage and the TL431 IC switches on the transistor to sink the remaining charging current, therefore keeping the output stable.

According to (Texas Instruments, 2004) the following equation can be used to determine the output voltage of the precision regulator.

$$V_o = \left(1 + \frac{R1}{R2} \right) V_{ref} \quad (34)$$

Resistor $R1$ was calculated to be 47kΩ (E12 value) and resistor $R2$ to be 100kΩ (E12 value) (refer to Appendix A). With a reference voltage of 2.4V – obtained from the datasheet – the regulator will produce an output voltage of 3.528V DC. This voltage is slightly lower than the specified WSN operational voltage of 3.6V DC. This is attributed to the resistor and transistor tolerances, resulting in voltage fluctuations, and therefore the design will use the theoretical $R1$ and $R2$ values.

The TL431CLP is specified for an operational temperature range of 0 – 70°C. This is adequate for laboratory testing conditions; however, when designing this model for use in the field, the alternative TL43xx1 will be used, as it can operate at a temperature range of -40°C – 85°C, making this device a more robust choice for this application.

In order to show that the first design stage of the electronic circuit was correctly regulated, a simulation is done using an open source simulation software package called LT Spice. A current source of 120mA is chosen as it represents the current produced by the CT after rectification when the 100kVA transformer is operating at typical phase current capacity. The calculated E12 resistor values are used in order to obtain the most accurate simulated output. A 1mF supercapacitor is chosen, which is not the capacitance value used in the final design, however it is chosen purely for simulation purposes. Therefore, the time the capacitor takes to charge is irrelevant, and can be neglected.

The results of the simulation are shown in Figure 4-27. Here it can be seen that there are two different charging occurrences on the time axes. The first line, beginning at the origin ($V_{\text{voltage_regulation}}$), shows the voltage as the supercapacitor charges to its regulated maximum capacity of 3.3V. The second line ($I_{e(Q1)}$) shows the function of the transistor in the rectification circuit (see Figure 4-28). It can be seen that when the supercapacitor is at a lower voltage (between 0 – 3V), the transistor ($I_{e(Q1)}$) is not conducting any current. When the charging voltage reaches the dashed line, the voltage is approximately 3.2V DC. This indicates when the transistor begins to switch on and conduct current. As the charging voltage increases further, approaching the maximum theoretical voltage, the transistor conducts more current until it is fully switched on, finally sinking all the current when the capacitor reaches its maximum calculated voltage.

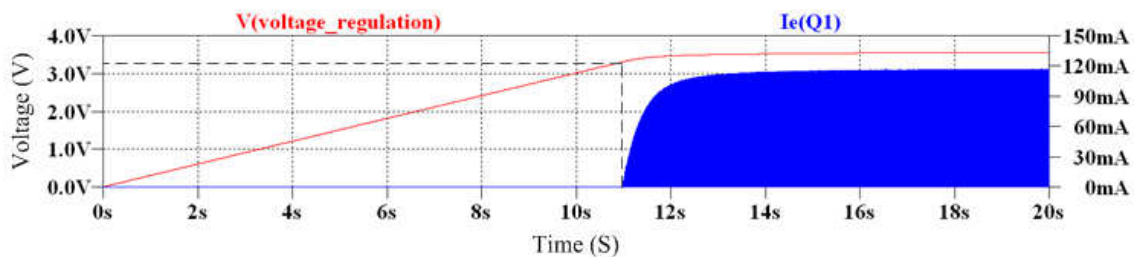


Figure 4-27 Simulation of voltage and current regulation

4.3.3 Energy storage

A standard HW series gold supercapacitor will be used, having a maximum storage capacity of 70F at a maximum voltage of 2.1V DC. As this voltage is not enough to power the WSN, two of these capacitors will be used in series. Two capacitors in series means the voltages add, giving 4.2V DC, but the total capacitance halves, giving 35F. This is illustrated in the circuit diagram in Figure 4-28.

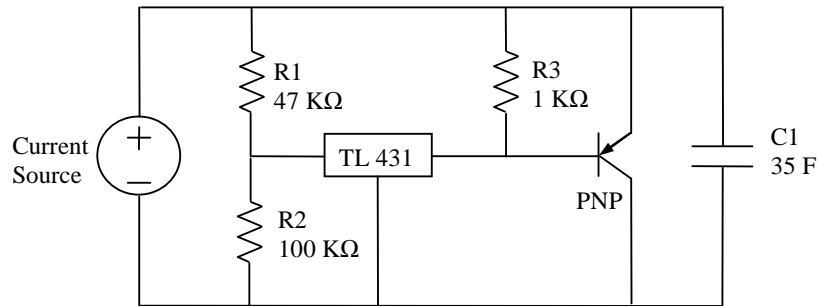


Figure 4-28 Voltage regulation circuit with actual circuit capacitance

A simulation was done to illustrate the time taken to charge the capacitor of 35F at a constant current of 120mA. As the LT Spice simulation program cannot support many data points the following equation (Floyd, 2005) is used to determine the theoretical charging time of the capacitor when the transformer’s primary current is 120A.

$$t = \frac{C V_c}{I_c} \tag{35}$$

This gives a theoretical time of 17minutes and 30 seconds to charge the capacitor from 0V DC to a peak voltage of 3.6V DC (refer to Appendix A).

4.3.4 Voltage analysis

It has been explained how the voltage input charges the supercapacitors to operational voltage, which does not exceed the maximum operational voltage of the WSN. However, when the primary transformer supplies a very low operational current, this may not satisfy the required magnetising current of the CT needed to produce stable operational energy, and therefore may not contribute toward charging the capacitors. When this happens, the WSN will still take current samples over that period of time, draining power from the supercapacitors that are now not being charged.

The capacitor's voltage will slowly decrease until such time as the WSN ceases to function, and this process may also result in the WSN taking inaccurate measurements. A voltage analysis will therefore be conducted on the output of the capacitor feeding the load (WSN). Figure 4-29 illustrates where the voltage analysis takes place in order for the most efficient impact on the load.

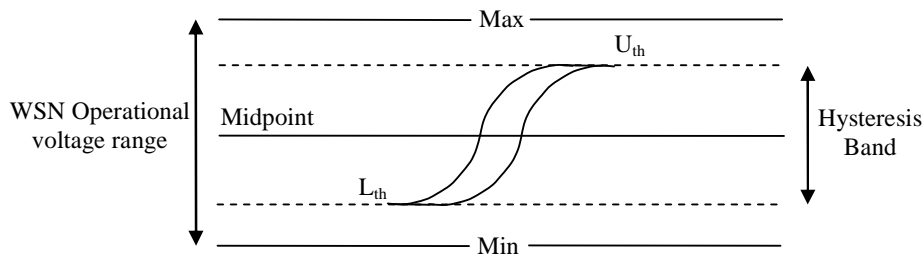


Figure 4-29 Illustration of hysteresis band

To reduce the possibility of inaccurate current measurements occurring, a function called hysteresis is implemented in the design. This provides the ability to create a specific voltage operation window, called the hysteresis band, as illustrated in Figure 4-29, in order to provide a stable and efficient output voltage to the load.

The hysteresis band allows full control of the voltage output to the load. When the electronic circuit is supplied with a sustainable current from the CT, it will charge the capacitors to the maximum value allowed by the voltage regulator. The hysteresis function will prevent any power from reaching the load until the capacitor voltage reaches the upper threshold U_{th} voltage. Once the capacitor's voltage reaches U_{th} the comparator will enable its output, causing the full voltage potential to appear across the load. If the input current from the CT decreases to the point where it can no longer charge the capacitor, the load will still stay operational as long as the capacitor voltage stays above the lower threshold L_{th} voltage. Once the capacitor voltage drops below L_{th} the comparator will disable its output, thereby decoupling the load from the capacitors, giving the capacitors time to charge to U_{th} again. The hysteresis function guarantees measurement accuracy as the WSN is always kept within its optimum voltage levels.

The MAX 931 ultra-low power comparator IC is chosen for the voltage analysis function. This was the best option due to its availability, low power consumption, low cost, built-in hysteresis function and ability to produce its own internal voltage reference, which effectively eliminates any design errors that may occur due to a drift in reference voltage.

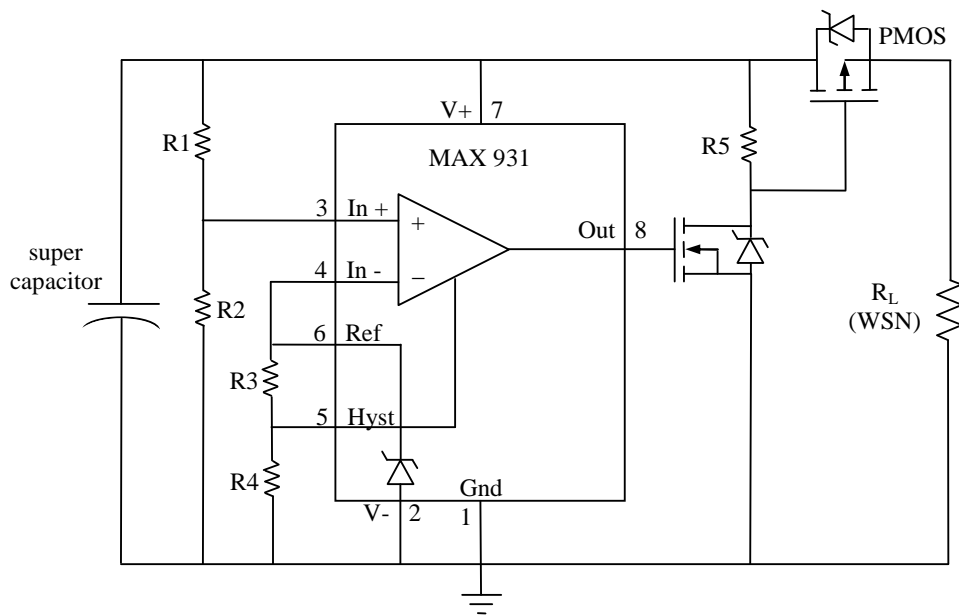


Figure 4-30 Threshold detector, as redrawn from (Maxim, 2012)

Figure 4-30 is a circuit diagram incorporating the hysteresis band used to ensure the optimum voltage range for the WSN. The Values of $R3$ and $R4$ are used to determine the hysteresis band of the circuit, and are therefore the first resistances to be calculated. According to (Maxim, 2012) the following equations can be used to calculate these values

$$R3 = \frac{V_{HB}}{2 I_{ref}} \quad (36)$$

$$R4 = \frac{(V_{ref} - \frac{V_{HB}}{2})}{I_{ref}} \quad (37)$$

This gives the value for $R3$ as $82k\Omega$ and the value for $R4$ as $2.2M\Omega$ (refer to Appendix A).

The datasheet shows that the MAX931 IC can provide a maximum hysteresis band of 100mV. Therefore, the resistors $R3$ and $R4$ have been calculated so to provide a lower hysteresis band of 85mV, being good design practice to operate the IC at its maximum value. The hysteresis band currently swings around the internal reference voltage 1.18V, which is impractical for the operational voltages of the WSN. Therefore, resistors $R1$ and $R2$ have been added to the circuit in order to increase the midpoint voltage and the hysteresis band. The following equations are used to determine the new voltage midpoint, the total hysteresis band, and the upper and lower threshold.

$$V_{Uth} = \frac{(V_{ref} + (\frac{V_{HB}}{2}))(R1 + R2)}{R2} \quad (38)$$

$$V_{Lth} = \frac{(V_{ref} - (\frac{V_{HB}}{2}))(R1 + R2)}{R2} \quad (39)$$

Once the values of $R1$ and $R2$ were determined, the new upper threshold voltage was calculated to be 3.06V and the new lower threshold value was calculated to be 2.848V (refer to Appendix A). The new hysteresis band is then calculated according to

$$V_{HB (new)} = V_{Uth (new)} - V_{Lth (new)} \quad (40)$$

Therefore, by the addition of these two resistors, the new hysteresis voltage was calculated to be 213mV (refer to Appendix A), allowing for longer operation of the WSN in the event of no energy being supplied by the CT.

This voltage analysis is simulated in order provide an indication of how the circuit functions with all of the calculated resistance values. Figure 4-31 illustrates four complete charge / discharge cycles. The time taken to charge the capacitor is irrelevant as the simulation is purely theoretical and done in order to indicate the functionality of the design. Two waveforms are present, the first shows the capacitor charging from 2.2V then discharging when the load is connected, and the second shows the voltage across the load. This voltage starts at 0V, and as soon as the capacitor voltage reaches U_{th} the load connects to the circuit via the threshold detector (shown in Figure 4-30).

The voltage across the load then increases from 0V to the capacitor voltage. However, when the capacitor discharges to L_{th} the load voltage drops once again to 0V, meaning that the load is disconnected from the capacitor, giving the capacitor time to recharge.

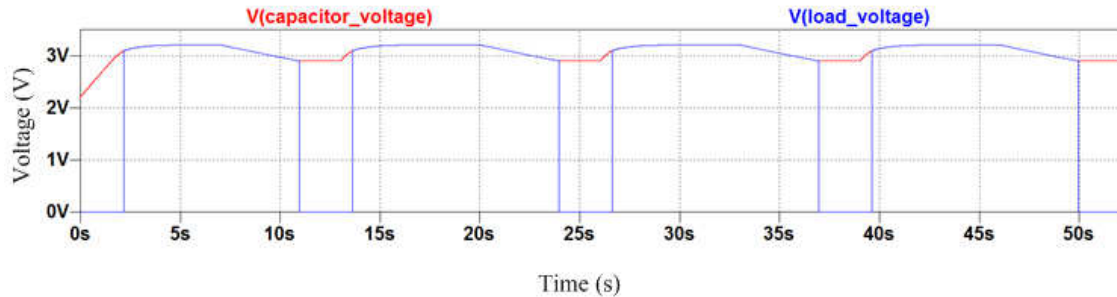


Figure 4-31 Simulation graph illustrating output voltage control across the load

Figure 4-32 is a close-up view of the first ten seconds of the charging cycle. This enables the upper and lower voltage bands and the hysteresis voltage to be more clearly seen. The simulation indicates that the voltage control circuit has an upper threshold voltage of 3.094V which closely relates to the calculated value of 3.06V. When the load discharges the capacitor, the lower threshold voltage of 2.9V is reached, which also relates closely to the calculated value of 2.848V. With these voltages known, the hysteresis band was calculated to be 194mV, which is 19mV lower than the calculated value.

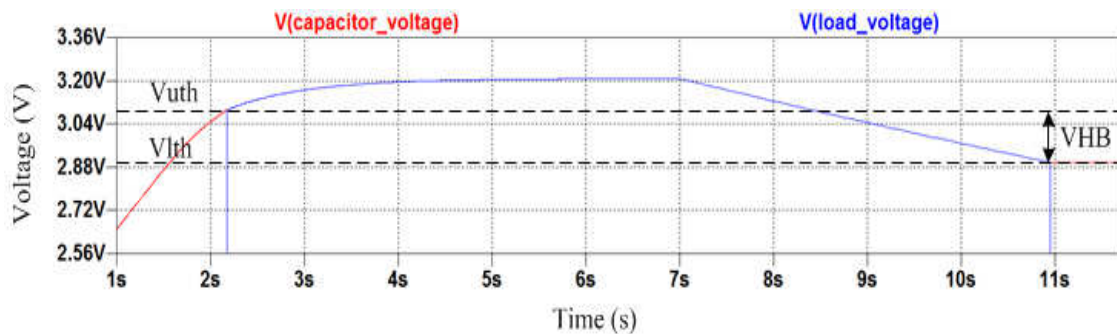


Figure 4-32 Simulation graph illustrating upper and lower threshold voltages

With this voltage control the load will be supplied with a voltage that will ensure the WSN operates in its optimum range when active, thereby providing reliable and accurate information. This leads to the next part of the design process which incorporates the load as well as the measurement component.

4.3.5 The load

The loading section of the design is crucial in terms of the output of the transformer current monitoring system, which comprises two main sections. The first is the WSN, responsible for the control of the electronic circuitry and the gathering, conversion and transmission of information. The second is the electronic circuitry responsible for the current measurement. These two sections cannot function individually and will therefore be explained as a unit.

Figure 4-33 shows the circuit diagram used to do the current measurements on the transformer. As this electronic circuit is controlled by the WSN, it is regarded as the brain of the circuit. The current flow in the circuit is one of the key parameters affecting the operation of the system. When the primary energy source (PMT) is operating at typical current potential ($120A_{rms}$) the CT provides a secondary current of 120mA which flows into the system at CTI_{in} . The current at CTI_{in} is then subjected to either energy harvesting mode or current measurement mode. A brief discussion on how these different modes function is therefore given in the following section.

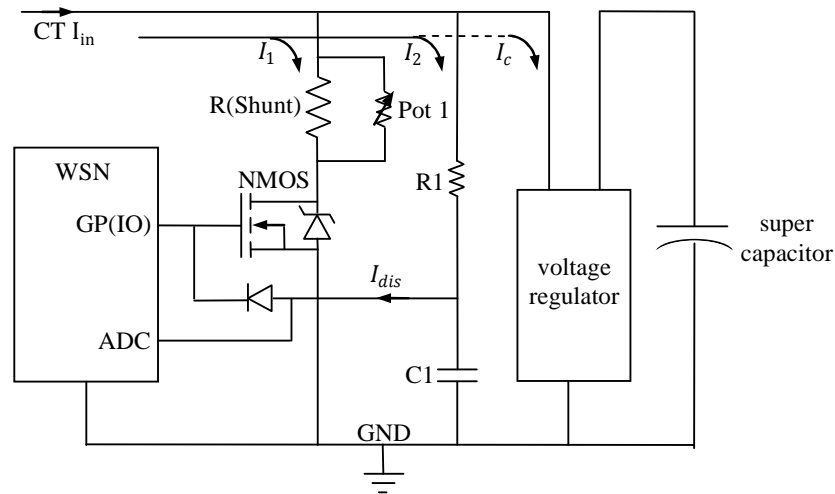


Figure 4-33 Current measurement circuit

4.3.5.1 Energy harvesting mode

When in energy harvesting mode, the general purpose input output [GP(IO)] pin of the WSN is programmed to 0V. The current at CTI_{in} is a rectified current (full bridge rectification) meaning that the CT current has a positive and negative cycle. When current passes through the rectifier, the output current (after rectification) has two positive halves. In energy harvesting mode, all the current bypasses the measurement section (I_1 and I_2) and flows into the supercapacitor, indicated by the dashed line I_c .

4.3.5.2 Current measurement mode

When in current measurement mode, the total current flows into the current measurement section (I_1 and I_2). In this mode the GP(IO) pin of the WSN is programmed to 3.094V. When the GP(IO) pin is set to a positive voltage, the N-channel MOSFET switches from an open to a closed state. When the N-channel MOSFET is closed, the current flows through the parallel combination of $R(shunt)$ and Pot 1. This causes a voltage to appear across the parallel resistance and ground, which charges the capacitor CI to that voltage.

The resistor and capacitor combination in the circuit is a crucial part of the design. The time taken for CI to charge to the maximum voltage (determined by the measurement current) and stabilise when the primary transformer is operating at its minimum current ($5A_{rms}$) is also important. This determines the maximum settling time the WSN needs to wait before starting to take current samples. Once the voltage of CI has charged to maximum and settled, the ADC of the WSN measures the voltage of CI .

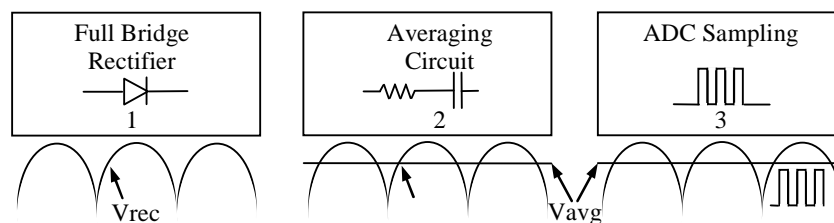


Figure 4-34 Waveform illustration for current measurement

Figure 4-34 shows the expected waveforms during the current measurements. The measurements consist of an average rectified wave created by the averaging resistor and capacitor combination (indicated by 2 in Figure 4-34). As the signal is rectified, the polarity of the negative cycle is changed to positive, thereby creating the rectified signal. As soon as the signal enters the averaging circuit, a steady DC voltage is formed, proportional to the average current and shunt resistance. Therefore, when $C1$ has charged to the average voltage and settled, the ADC is activated and samples the DC voltage (indicated by 3 in Figure 4-34). The following section explains how the electronic circuitry is controlled by the WSN.

4.3.5.3 WSN program

The program that operates the MSP430 processor in the WSN links the measurement circuit with the WSN. This section explains how the program functions are able to obtain certain output information. A full extended version of the program can be seen in Appendix D. A flow diagram indicating the individual functionalities of the WSN current monitoring program is shown in Figure 4-35.

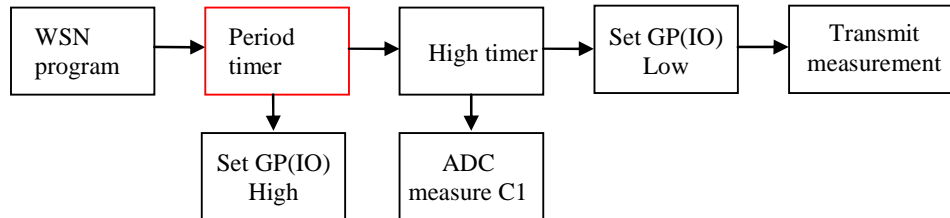


Figure 4-35 Flow diagram of WSN program layout

The foundation of the program is based on timers, the two most important being the periodical interval, or period timer, and the high interval, or high timer. The function of the period timer is to create a period in which the program will run; in this case a periodic interval of 60s is chosen, meaning that the program will run in a continuous loop which repeats itself every 60s. Consequently, a current measurement will be taken every 60s, leading to 1440 measurements every 24 hours. This sample rate is considered adequate in order to obtain the information needed for condition monitoring. To begin the process, the period timer is fired (started) which immediately sets GP(IO) pin 23 of the MSP430 to its high state.

When this pin is enabled, the energy harvesting circuit is disconnected (indicated by I_c in Figure 4-33), the current measurement circuit is enabled and the high timer is fired. The period of the high timer is based on the time taken for CI to charge to the average voltage (determined by the CT current). The maximum charge time of CI depends on the lowest specified current rating required to be measured by the WSN. Because of the size of $C1$, the maximum charge time is 519ms (refer to Appendix A).

It is therefore decided to make the high time interval 1s, giving CI 1s to charge to its maximum value and stabilise. When the high timer reaches the end of its period and CI is charged to the correct voltage, the current measurement function is activated. This enables ADC0 (pin 59) on the MSP430 which take a voltage measurement. Once this is done, GP(IO) pin 23 is reset to 0V. The electronic circuit is then switched back to energy harvesting mode. As soon as the pin is grounded, the WSN constructs the data packet and transmits the information to the base station. The period of the high and periodic timers will now be complete and the program will repeat itself. Figure 4-36 illustrates the timer intervals and how they are programmed to operate.

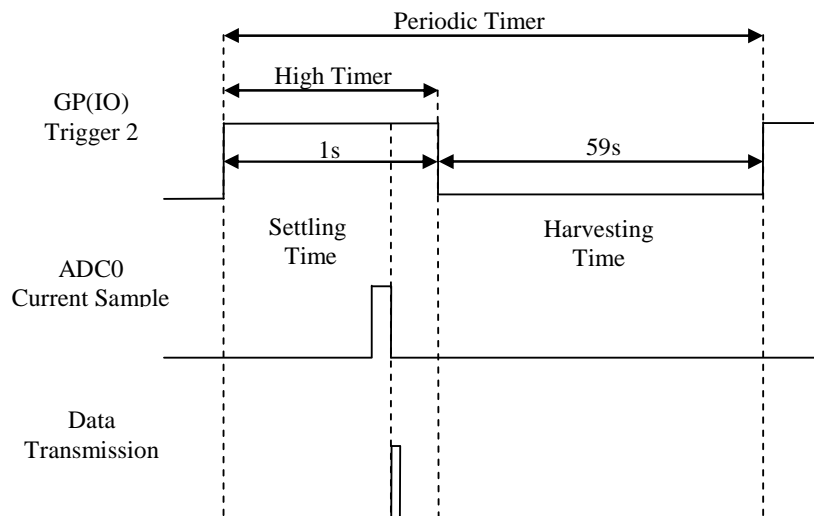


Figure 4-36 Timing structure of the WSN program

4.3.6 Testing the condition monitoring system

The condition monitoring system, comprising the CT, the electronic circuitry and the WSN, was assembled and connected to the current simulation rig shown in Figure 4-37 for testing. By supplying the rig, having forty turns, with a constant AC of $3A_{rms}$, an alternating magnetic flux is generated that is relative to the flux generated by a single conductor carrying an AC of $120A_{rms}$.

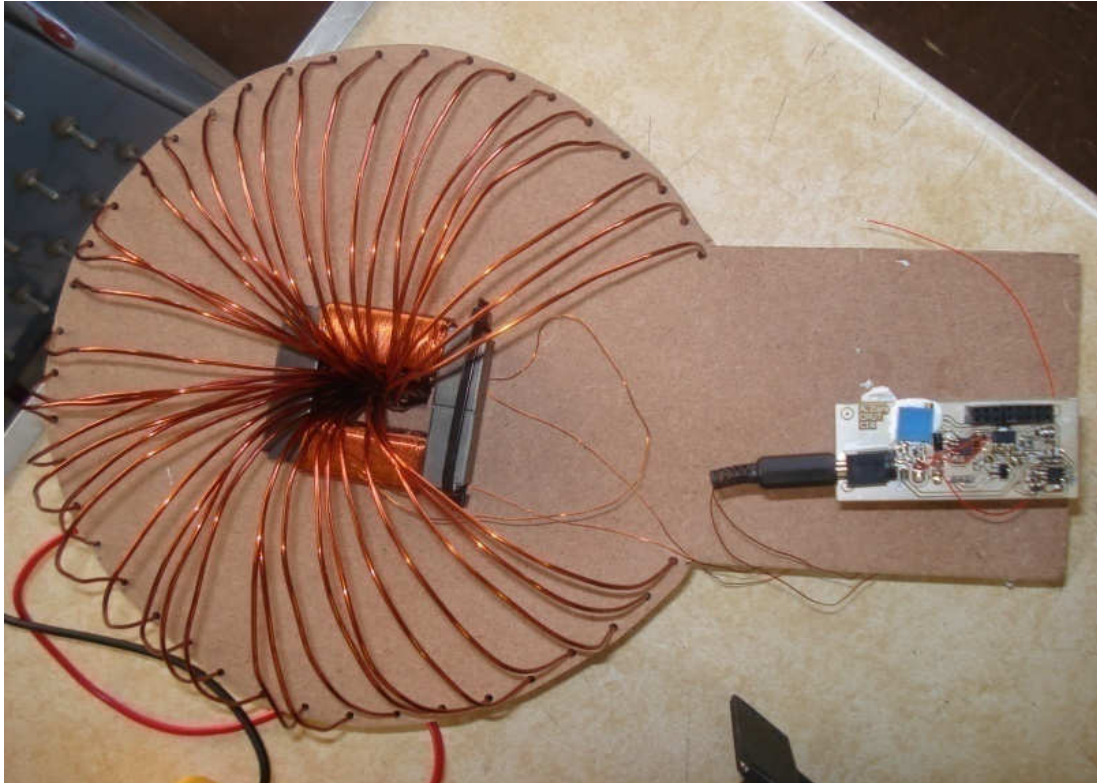


Figure 4-37 Condition monitoring system connected to test rig

An illustration of how the test was conducted is shown in Figure 4-38. The condition monitoring system harvested its energy from the current simulation rig, thereby charging the supercapacitors and powering the WSN which began to measure the current from the primary source (current simulation rig). These measurements were then wirelessly transmitted as data packages to the base station, which is directly connected to the local laboratory computer where the current readings are displayed.

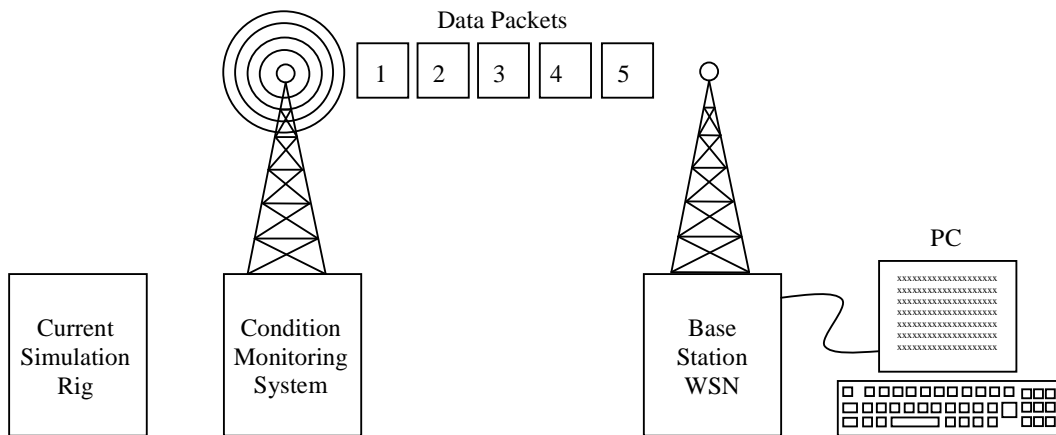


Figure 4-38 Transformer condition monitoring system laboratory measurement

When the first measurements were received it was found that the current readings were fluctuating and unstable and therefore no true reading could be established in order to calibrate the device. By further investigation it was found that a small voltage ripple (45.5mV) was occurring on *CI*, the measurement of which is shown in Figure 4-39.

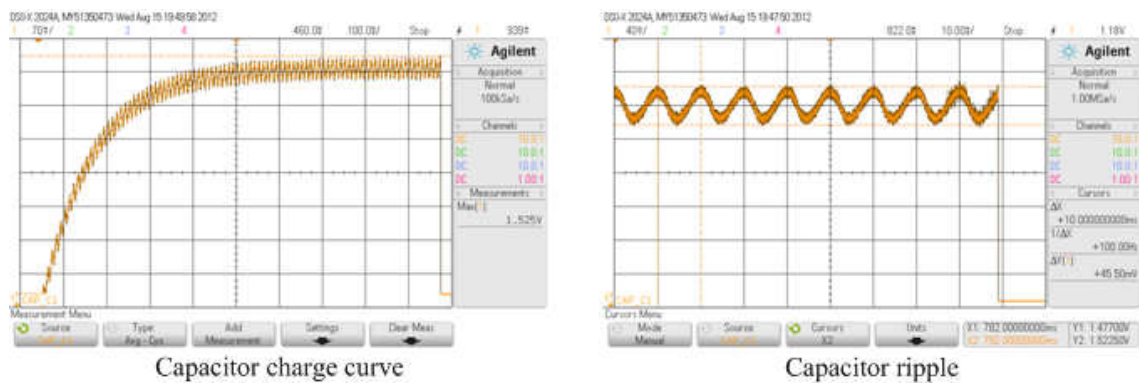


Figure 4-39 Capacitor charge cycle indicating voltage ripple

When the WSN reads the voltage on *CI*, it must fall between 0 – 2.5V, which is the internal reference of the WSN and is directly linked to a twelve bit value (4096). This twelve bit value is also directly linked to a current reading falling between 0 – 200A. The following equation was therefore developed to calculate the output current.

$$I_{prim} = \frac{V_{cap}}{V_{ref}} 200 \text{ (A)} \quad (41)$$

This gives a current swing (ripple) of approximately 3.6A associated with the 45.5mV voltage ripple (refer to Appendix A).

In order to eliminate the current ripple without having to change the hardware, an averaging circuit is introduced into the WSN program. The program will now be changed to take nine consecutive measurements, taking approximately 20ms to complete. The program then automatically sums the voltage measurements and determines the mean value. By doing this, the ripple experienced on $C1$ is averaged, thus providing a stabilised current reading. A flow diagram of the newly developed code is illustrated in Figure 4-40.

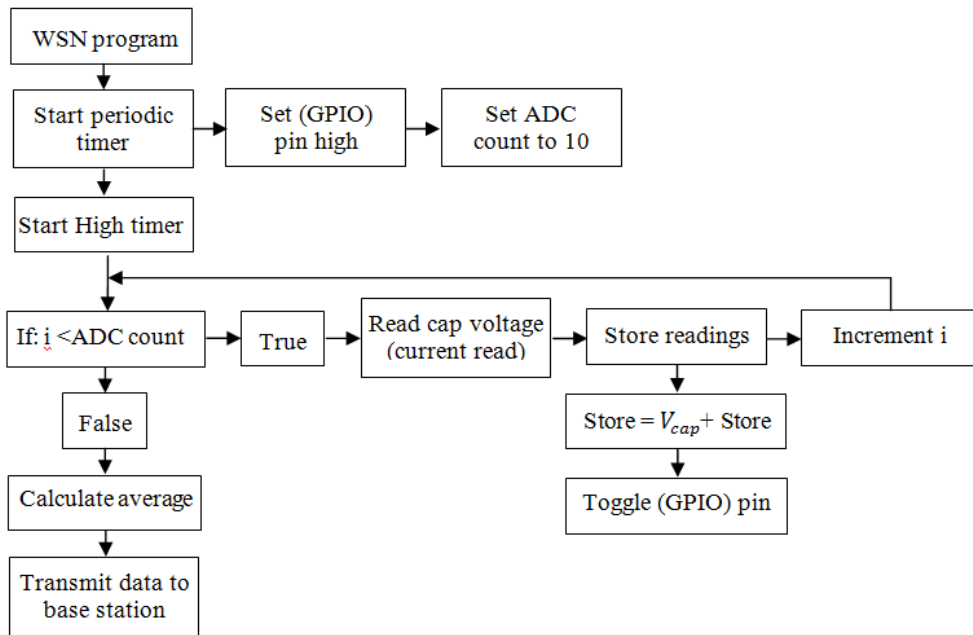


Figure 4-40 Flow diagram of WSN with ripple averaging

The same experiment illustrated in Figure 4-38 is repeated in order to see how the averaging method will commence. The results are shown in Figure 4-41.

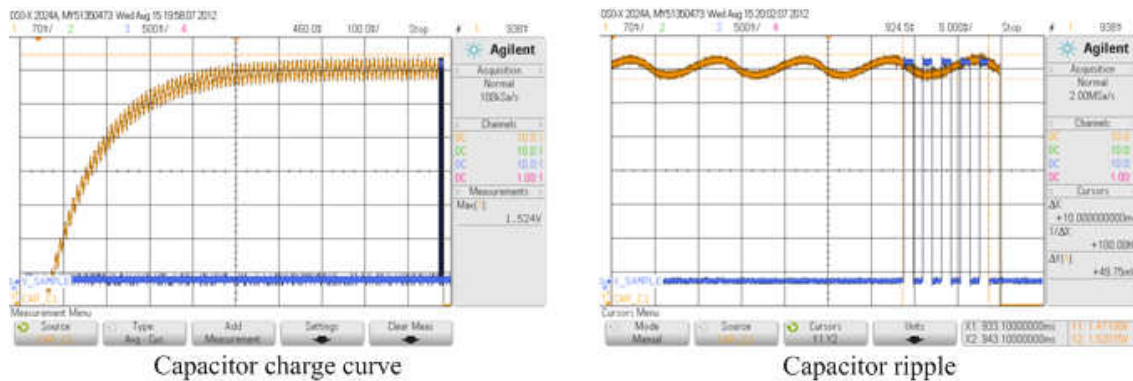


Figure 4-41 Capacitor charge curve indicating voltage samples taken on ripple

Here it can be seen that the voltage samples taken for one ripple cycle are approximately 20ms in length. A GP(IO) pin was programmed to switch its state from zero to maximum each time a voltage measurement is taken. Therefore, the five pulses indicate that a total of nine measurements were taken at the end of the capacitor charge cycle.

The flow diagram in Figure 4-40 illustrates the final WSN average RMS calibrated code that will be used to program the electronics on the printed circuit board (PCB). In order to filter out the ripple an 'if' statement is implemented in the original code, which will repeat itself until its conditions have been met. When the loop is complete, all the data will be fed into an averaging formula, where the result is constructed into a package and transmitted to the WSN base station. Now that the measurement section is complete, the following chapter will focus on how the device is calibrated and tested for accuracy.

Chapter 5

CT calibration

In order to ensure measurement accuracy from the current monitoring system, the CT is calibrated with a reference ampere meter. The current simulation rig shown in Figure 4-37 is connected in series to a calibrated Fluke 189 data logger to obtain precise true RMS current readings and to verify that the rig is producing a stable sinusoidal AC. As explained in Section 4.3.6 the rig of forty turns is adjusted to produce a current output of $3A_{\text{rms}}$ which generates a flux matching that produced by one phase of a 100kVA transformer carrying $120A_{\text{rms}}$. The current monitoring system is then connected to the rig and the output monitored.

As expected, the output (current reading) of the device was not initially accurate; however, the current was stable. Pot 1 in the current measurement circuit of Figure 4-33 is used to adjust the current reading to match the $120A_{\text{rms}}$ of the rig, after which the device was monitored to observe whether the measurements are accurate and repeatable.

After this calibration, a standard accuracy test is performed to determine the device's accuracy over its full measurement range. The output of the device is compared to readings obtained by a Fluke 43 power quality analyser with a 500A CT current clamp connected to the same current simulation rig.

The two devices were tested over the range 10 – $200A_{\text{rms}}$, beginning at 5A, and in measurement increments of 10A. The current monitoring system is programmed as in Section 4.3.5.3 therefore taking measurements every 60s. Five measurements were taken at each current interval and the averages of these were used to determine a total average error (maximum of 3% as shown in Figure 5-4) associated with each measurement device, which are then compared. This process is repeated five times in order to ensure accurate results (refer to Appendix C).

5.1 Results

The results of the calibration are shown in Figure 5-1. This graph compares the current of the current simulation rig with measurements taken by the average RMS calibrated meter. The measurements are taken at 10A increments beginning at 5A for the first current sample. The CTs are labelled from average RMS calibrated (ARC) CT1, being the first test, to ARC CT5, being the fifth test. The high and low limits shown on the graph are determined by the allowable percentage error specified in the beginning of the design stage. The two dashed lines on the graph indicate the allowable calculated current error according to design specifications, giving the current values which the readings may not exceed. This graph shows that the ARC CT exhibits a linear response to the current increments over the full measurement range and indicates good repeatability and consistent accuracy over the five tests.

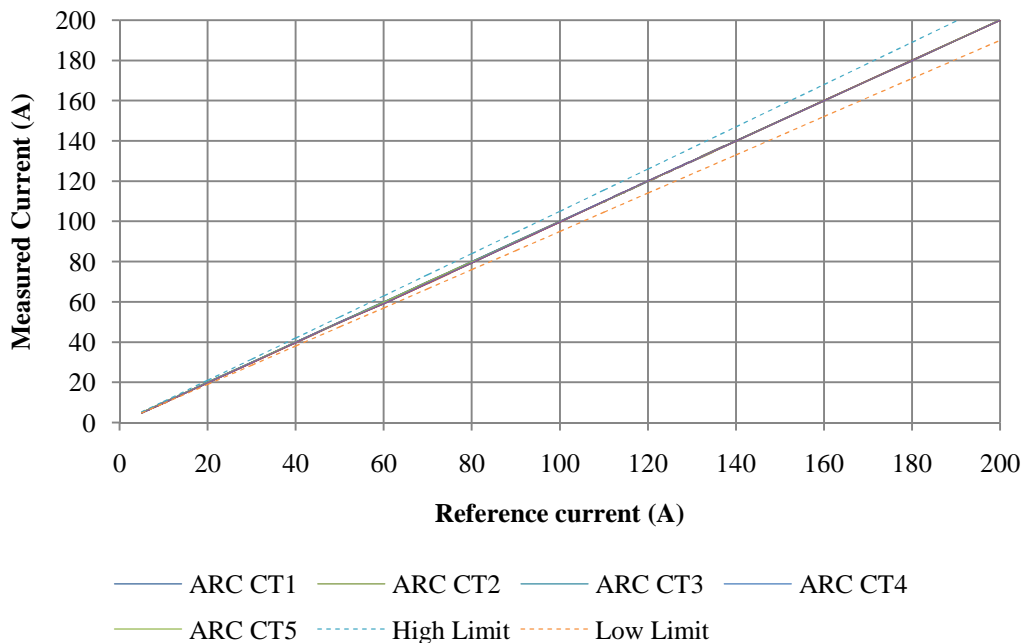


Figure 5-1 Accuracy of current monitoring system over full measurement range

Figure 5-2 shows the measured error values of the ARC CT over the operational current range. All the test results show that the device is operating well below the five percent error allowed in the design specification. It can also be seen that the error increases as the current is decreased to the minimum value of $5A_{rms}$, which is attributed to magnetising losses associated with the magnetising current in the core of the CT, as previously explained.

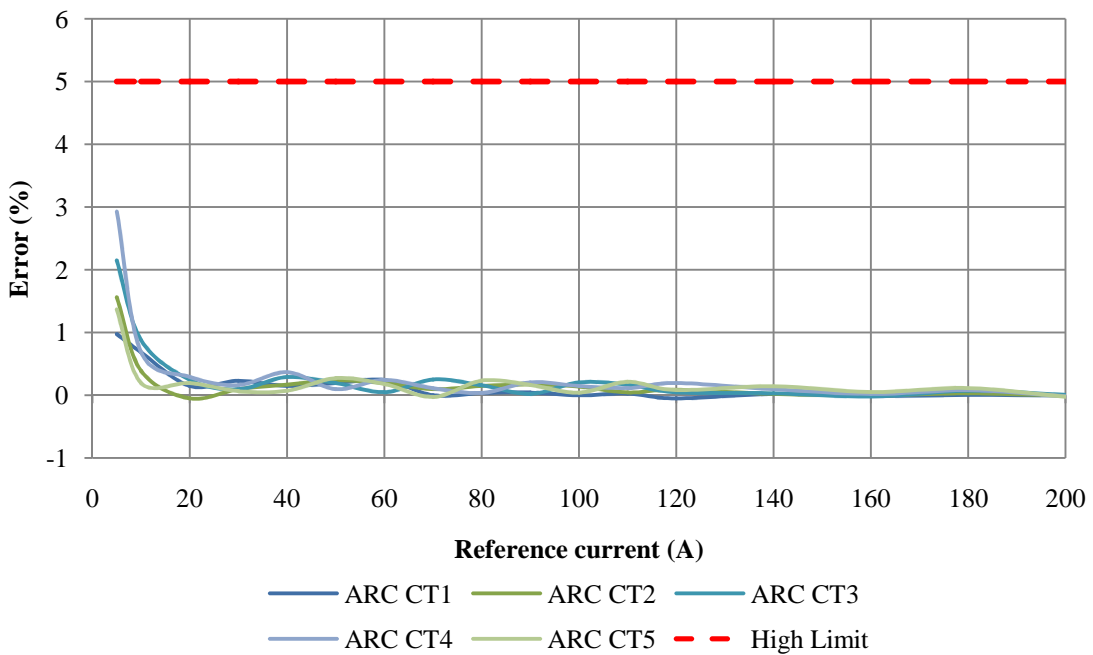


Figure 5-2 Error measurement on current monitoring system

Figure 5-3 shows the error percentage results of both the ARC CT and the OTS CT. Both devices are shown to be operating well below the five percent error allowed in the design specification. In addition, it can be seen that the ARC CT performs better when subjected to a perfectly sinusoidal signal.

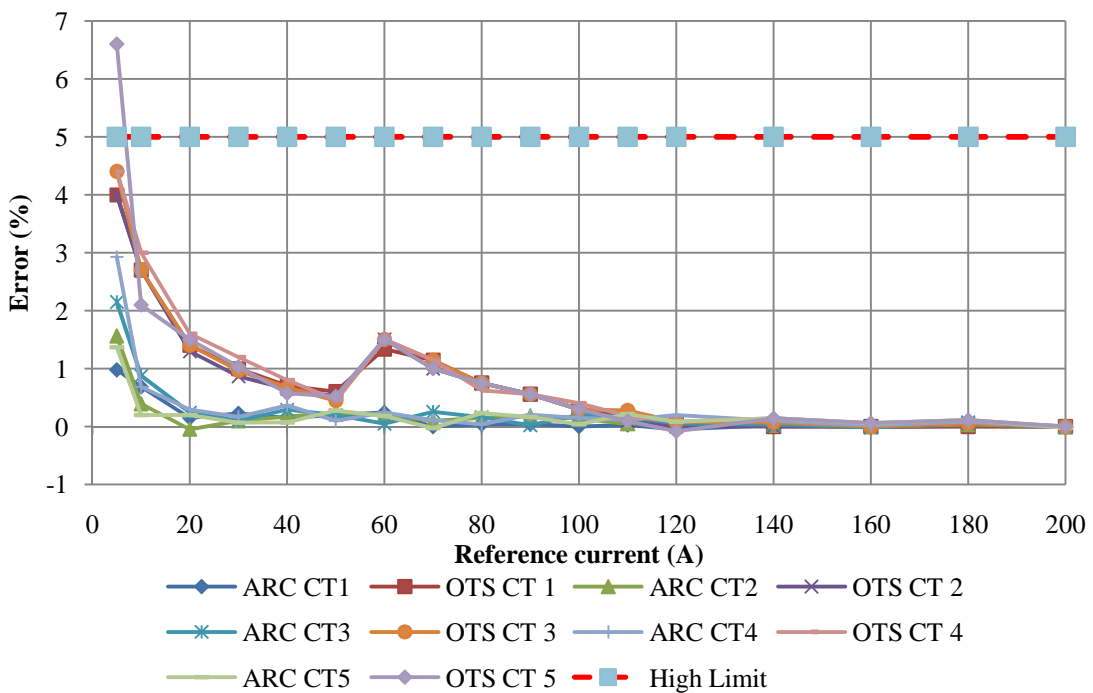
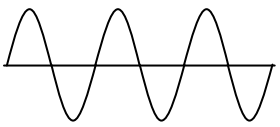
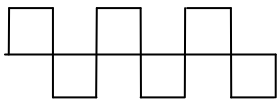
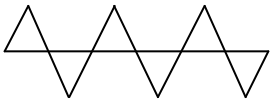


Figure 5-3 Error measurement comparison between ARC CT and OTS CT

By looking at Figure 5-3, a constant rise in error readings can be seen associated with the OTS CT at 60A. This is considered to be due to a phenomenon called the quantisation error. This is known to occur with digital meters when the meter fails to provide the correct digital representation of an analogue value as it is limited to discrete incremental values. The actual value may fall anywhere between the two discrete values, thereby introducing an error in the reading(Carr, 2002). This current change could also be due to the fact that the OTS Fluke 43 meter has an auto scale function which changed from the 50 A scale to the 100 A scale during calibration.

As previously mentioned, all the tests were conducted under laboratory conditions with purely sinusoidal waveforms. Two additional tests were performed to observe what happens when a waveform becomes distorted. In the first test, a square wave was supplied to the current simulation rig at $100A_{rms}$ and a total error of 7.91% was measured with the ARC CT when compared to the true RMS reading of the OTS CT. However, in reality, this type of waveform is highly unlikely to occur. In the second test, a sawtooth wave was supplied to the current simulation rig at $100A_{rms}$ and a total error of 3.2% was measured with the ARC CT when compared to the OTS CT. In reality, this type of waveform is more likely to occur in the system than the square wave due to harmonics being introduced on the consumer side. The results of these tests are shown in Table 5-1.

Table 5-1ARC CT results compared with OTS CT results as measured at $100A_{rms}$

Waveforms	Description	OTS CT Error	ARC CT Error
	Sine wave	0.32%	0.105% (0%)
	Square wave	0.4%	7.91% (10%)
	Sawtooth Wave	0.1%	3.2% (3.3%)

Chapter 6

Field testing

Field tests are conducted in order to show that the energy harvesting current monitoring device has the ability to produce accurate sustainable current readings when facing actual currents affected by different residential loads. These tests were performed in Paarl at a mini substation supplying power to a residential area. This mini substation comprises five connection points each having the same current rating of the current monitoring device. Two of the five points were monitored over a period of one hour.

The current measurements were done by connecting an OTS CT (with a Fluke 43 power quality analyser) to one incoming phase. The Fluke 43 is used as it has the ability to take true RMS current measurements and determine THD. The energy harvesting current monitoring system was then connected to the same incoming phase as the OTS CT and programmed to take current samples every 60s.



Figure 6-1 Internal layout of mini substation in Paarl

The internal layout of the mini substation is shown in Figure 6-1. The several outgoing LV phase cables shown supply power to various regions of the residential area. A number of tests will be conducted on these phases. The first test will take measurements on the red phase which supplies the local OK Minimarket kiosk, as indicated by the right circle in Figure 6-1. This is done in order to observe what influence a commercial building has on the current monitoring system, the results of which are shown in Figure 6-2.

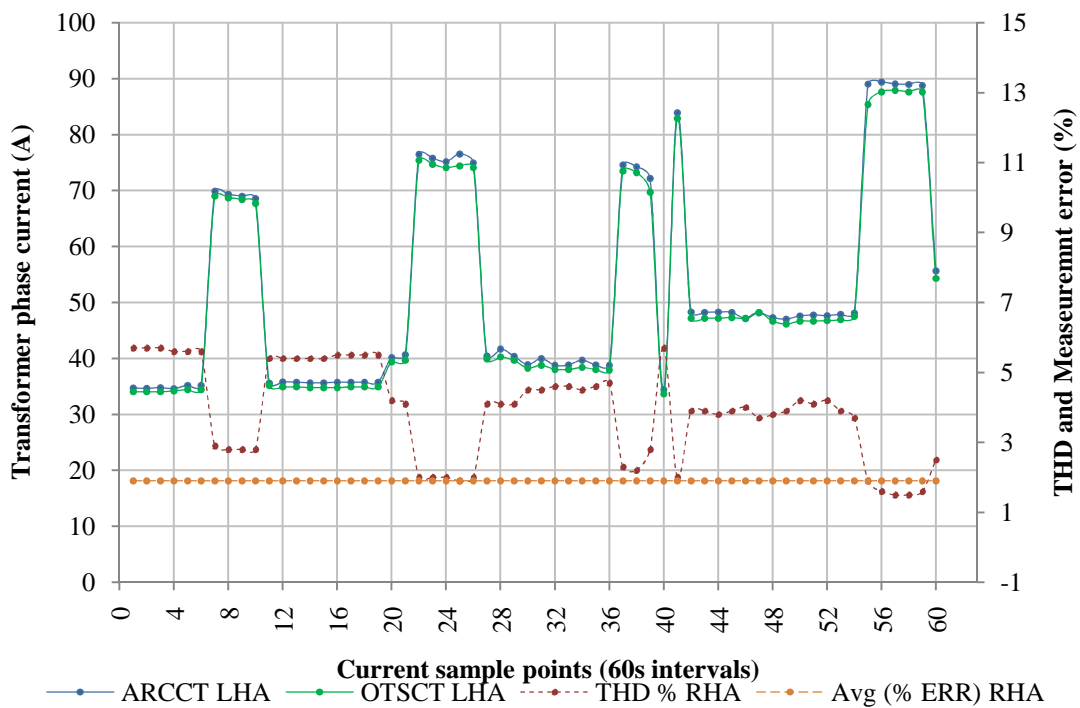


Figure 6-2 OK Minimarket phase current tests

As shown on the graph, the results of the ARC CT are compared with the results of the OTS CT (with the Fluke 43 power quality analyser). The brown line represents the THD on the phase, measured by the Fluke 43, and the orange line represents the average difference between the two measurement results. The minimarket load comprises lighting, PCs, cashier tills, refrigerators and a bakery. The biggest current consumer is therefore the ovens in the bakery. When the ovens are switched on, this causes a current inrush of 90A, during which time the harmonics of the system decreases from 5% THD to around 2.5% THD.

When this load is switched off, the current reduces to between 35 – 40A, and the harmonic distortion returns to around 5% THD. However, this does not have a significant influence on the measurements when comparing the OTS CT to the ARC CT.

The second test will take measurements on the blue phase which supplies Mash Street, as indicated by the left circle in Figure 6-1. This represents a typical residential load associated with the PMT phase current that the transformer monitoring device is designed to measure. Figure 6-3 is a close-up of the two measurement instruments connected to the blue phase supplying Mash Street.



Figure 6-3 Close-up of current monitoring devices on blue phase feeding Mash Street

Figure 6-4 shows the measurements of transformer phase current supplying Mash Street. It can be seen that the THD on this phase is greater than that of the phase supplying the OK minimarket. This is considered to be due to these measurements being done in the off-peak period when few household resistive loads were switched on. However, the current measurements of the average RMS calibrated system are still relatively accurate compared to the results of the Fluke power quality analyser. As seen in Figure 6-4, the total average error between the OTS CT and the ARC CT measurement results is well below the five percent allowable limit.

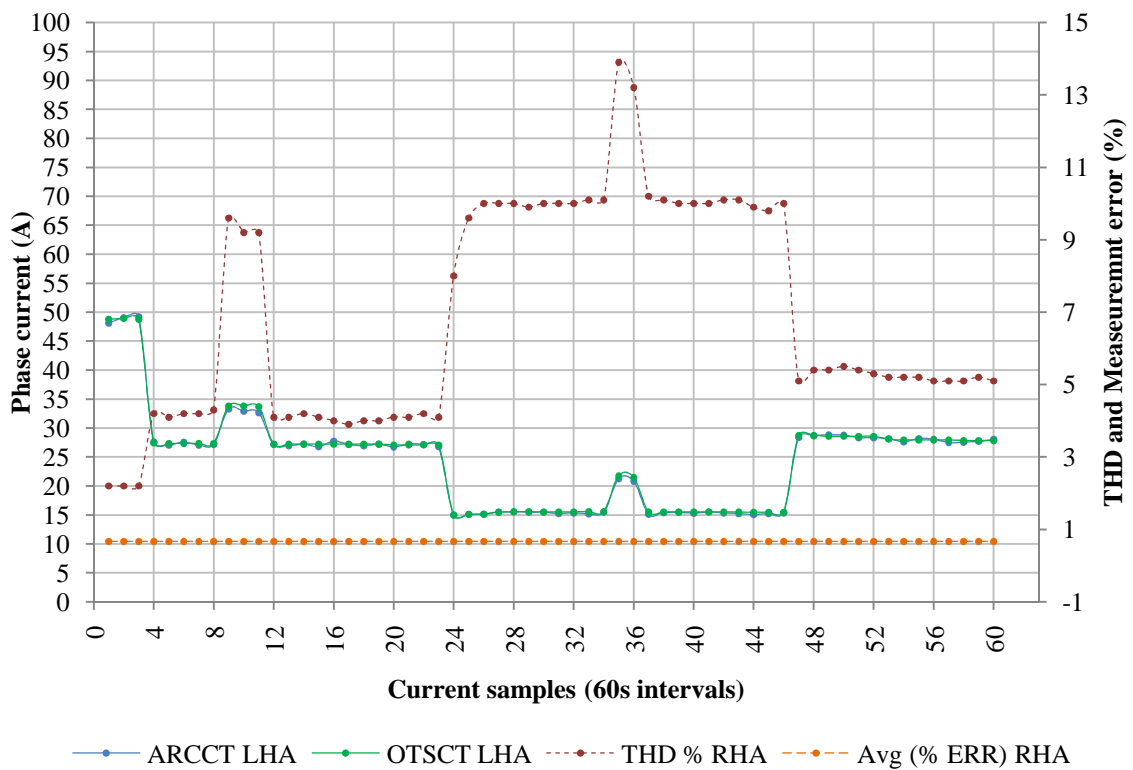


Figure 6-4 Measurement of transformer phase current supplying Mash Street

By looking at Figures 6-2 and 6-4 it can be seen that the major difference between the two measurement results is the harmonics present in the system of Figure 6-4. It was expected that the transformer phase with the most harmonic content will have the least accurate readings; however, this was not the case.

The magnitude of error between the OTS CT and the ARC CT is considered due to differences in the calibration of these devices. As previously explained, the ARC CT was calibrated in the laboratory. It was not possible to use the same OTS CT meters for the field tests, resulting in these meters being of the same quality but not calibrated to the ARC CT.

Chapter 7

Conclusions

The proposed transformer condition monitoring system was divided up into sections. The first section focused on the requirement of the device being self powered, using energy available from its environment. An energy harvesting system was therefore designed and developed which used the magnetic flux around the current carrying conductors of the transformer being monitored. A CT was designed with two purposes in mind – namely, to harvest energy from the flux to power the current measurement device, and to step down the transformer phase current to a practical value for measurement. This ensured a cost-effective energy harvesting and current measurement technique to perfectly fit the requirements of this study.

In order to prolong the lifespan of the current monitoring device, a study was conducted on the various types of energy reservoirs that are available. Supercapacitors were found to have the ability to supply sufficient energy to the current monitoring system while having a longer operational lifespan than that of the more traditionally used batteries.

An optimised smart electronic energy controlling system was designed and developed in order to control the energy harvesting as well as the current measurement process. This system ensured that the energy harvested by the CT was stored in the supercapacitors to enable current measurements and that the minimum and maximum demand required by the load was regulated. The design of the entire system enables it to operate at 4% of the rated transformer current. This enables the device to operate for extended periods of time without charging the supercapacitors.

For safety reasons, a wireless communication system was designed, using an off-the-shelf WSN powered by the energy harvesting system. The WSN was programmed to accumulate data which is wirelessly transmitted to another WSN serving as the receiver unit or base station.

Referring back to Problem Approach in section 1.2, it was established that the normal operational conditions of a PMT is between 0A and 133A. However as indicated in section 2.1.1, transformers can be driven past their 100% operational current. It was also possible to develop an accurate current measurement device (CT) for the specified PMT transformer. Furthermore it was found that the TelosB WSN was suitable for this project accompanied by low power consumption as mentioned in section 2.4. In order to provide the energy needed for this project, it was decided to harvest energy by means of magnetic induction at the transformer phase cables. This process proved to be sufficient and it was able to charge the supercapacitors under full operational condition of the WSN in the laboratory as well as at the mini substation when the field measurements were done. Finally with the field tests done, it proved that the ARC CT was able to do current measurements accurately in the field when compared with OTS CT commercial products.

7.1 Problems encountered

Energy harvesting forms the backbone of the transformer condition monitoring system's functionality. The manner in which energy is harvested via magnetic flux is directly linked to the system performance of the PMT. During off-peak periods, the secondary phase current of the transformer can be quite low. The energy harvesting system is not able to harvest more energy than that which is consumed by the condition monitoring system. Therefore, depending on the load characteristics, there is a chance that the supercapacitors may run out of energy to supply to the condition monitoring system due to these periods of low secondary PMT phase current.

With reference to the calibration results in Section 5.2, distorted waveforms were shown to introduce errors in the measurement system. These waveforms do occur out in the field; however, according to the study done in Section 2.2.1, it was found that the regions supplied by PMTs are less rich in harmonic content when the PMTs are subjected to an increase in load (peak period). This is due to the fact that during such periods the largest portion of the residential load is purely resistive resulting in a near sinusoidal waveform.

7.2 Proposed future work

A study can be conducted on simultaneous three phase current monitoring and in addition continuous monitoring could be done instead of using sample intervals. The condition monitoring system would be able to take RMS measurements if a stronger microcontroller were to be implemented in the design or if a RMS IC were to be used.

For the wireless transmission of data, an alternative system could be designed using less operational power and having a broader transmission range than the WSN used in this study. Improvements can also be made to the program which controls the operation of this system. An alert protocol could be developed which sends out a warning signal if the transformer is subjected to currents falling outside its specified operational range. The system could also be linked to a GSM modem, enabling a utility to connect to the transformer being monitored and review its operational current at any given time.

Finally, a smart end program could be developed to convert all the data obtained from the system into graphs. These would show the operational health of the transformer over time and whether it has been subjected to any hazardous loading conditions that may result in damage or even failure of the device.

References

ABB, 2013. *DistribuSense current and voltage sensors LVS outdoor low voltage split-core current transformer*, North Pinetops: s.n.

AE Sensors, 2012. *3DM-GX2*. [Online]

Available at: http://www.aesensors.nl/pdf/Microstrain/3dm-gx2_datasheet_v1.pdf

[Accessed 23 August 2012].

Ahola, J. et al., 2008. Design Considerations for Current Transformer Based Energy Harvesting for Electronics Attached to Electric Motor. *International Symposium on Power Electronics*, pp. 901-905.

Analog Devices, 2012. *High Precision, Wideband RMS-to-DC Converter AD637*.

[Online]

Available at: http://www.analog.com/static/imported-files/data_sheets/AD637.pdf

[Accessed 03 August 2012].

Anand, M. M. S., 2006. *Electronic instruments and Instrumentation technology*. New Delhi: Prentice-Hall of India Private Limited.

Anon., 1977. *Basic Electricity*. Washington: Headquarters, Department of the Army.

Anon., 2012. *Microstrain*. [Online]

Available at: http://files.microstrain.com/G-LINK_MXRS_Datasheet_Rev_1.02.pdf

[Accessed 23 August 2012].

Anon., 2012. *Moteiv*. [Online]

Available at: <http://www2.ece.ohio-state.edu/~bibyk/ee582/telosMote.pdf>

[Accessed 23 August 2012].

Arrillaga, J. & Watson, N. R., 2003. *Power System Harmonics, Second Edition*. In: Chennai: John Wiley & Sons, pp. 77-83.

Atikol, U., Dagbasi, M. & Güven, H., 1999. Identification of residential end-use loads for demand-side planning in northern Cyprus. *Energy* 24, pp. 231-238.

Bakshi, U. A., Bakshi, A. V. & Bakshi, K. A., 2008. *Electronic Measurement Systems, First Edition*. Pune: Technical Publications Pune.

Brittian, L. W., 2012. *Electrical trades pocket manual*. New Jersey: John Wiley & Sons.

Carr, J. J., 2002. *Practical Radio Frequency Test and Measurement: A Technician's Handbook*. s.l.:Newnes.

Catrinu, M. D. & Nordgård, D. E., 2010. *Methodology for Risk-Informed Maintenance and Reinvestment Decisions*. Singapore, s.n., pp. 372 - 377.

Catrinu, M. D. & Nordgård, D. E., 2010. *Methodology for Risk-Informed Maintenance and Reinvestment Decisions..* Singapore, s.n., pp. 372-377.

Chambers, A., 1999. *Natural Gas & Electric Power, in nontechnical language.*, s.l.: Penn Well.

Cyganski, D. et al., 1989. Current and Voltage Harmonic Measurements and Modeling at the Gardner Photovoltaic Project. *IEEE Transactions on Power Delivery*, 4(1), pp. 803-806.

David, A., Nino, A. F., Danko, K. & Jelena, S., 2005. *Constructing a wireless sensor network*. [Online]

Available at: <http://www.astro.hr/s3/2005/project4.php>

[Accessed 21 May 2012].

de Villiers, D., 2009. *Hybrid Energy Harvesting system for a Condition Moitoring Mote.* , s.l.: s.n.

Deyer, S. A., 2001. *Survey of Insrumentation and Measurement*. New york: john Wiley & Sons.

Di Tian, D. T., 2002. *A Coverage-Preserving Node Scheduling Scheme for Large Wireless Sensor Networks*. New York, s.n.

Dincer, I. & Rosen, M. A., 2011. *Thermal energy storage systems and applications*. Chichester: John Wiley & Sons, Ltd.

Ecologix controls ltd, 2012. *(EcoCT) Current Transformer*. [Online]
Available at: www.enocean-alliance.org/uploads/tx.../Ecologix_EcoCT_G1.pdf
[Accessed 21 August 2012].

Emanuel, A. E., Orr, J. A., Cyganski, D. & Gulachenski, E. M., 1993. A Survey of Harmonic Voltages and Currents at the Customer's Bus.. *Transactions on Power Delivery*, 8(1), pp. 1-11.

Erickson, R. W. & Maksimović, D., 2004. *Fundamentals of Power Electronics Second Edition*. Boulder: Kluwer Academic Publishers.

Eskom, 2011. *Trimming 10% is easier than you think*. [Online]
Available at: <http://www.eskom.co.za/content/10pcavingsBrochure.pdf>
[Accessed 5 September 2012].

Ferroxcube, 2012. *Ferroxcube*. [Online]
Available at: <http://www.ferroxcube.com/>
[Accessed 9 July 2012].

Fletcher, G., 2004. *Residential Construction Academy House Wiring*. New York: Delmar Learning.

Fletcher, G., 2012. *House Wiring, Third Edition*. New York: Delmar, Cengage Learning.

Flipsen, S., 2004. *Alternative Power Sources for Portables & Wearables*. s.l.:Delft University of Technology.

Floyd, 2005. *Electronic Devices, Seventh Edition*. Upper Saddle River: Pearson Prentice Hall.

Floyd, T. L., 1985. *Principles of Electric Circuits 2nd edition*. Ohio: Charles E. Merrill Publishing Co.

Fluke, 2012. *Fluke 43B Series Power Quality Analyzer*. [Online]
Available at: <http://www.fluke.com/fluke/uken/Power-Quality-Tools/Single-Phase/Fluke-43B.htm?PID=56081>
[Accessed 21 August 2012].

Gapta, D. A., Lilien, D. L. & Yang, D. Z., 2004. *Wise(Wireless Sensornets) Laboratory*. [Online]
Available at: <http://www.cs.wmich.edu/wsn/>
[Accessed 5 June 2012].

Gaunt, T. et al., 2012. *Informal Electrification in South Africa.*, Cape Town: Sustainable Energy Africa.

Goodenough, J. B., Abruna, H. D. & Buchanan, M. V., 2007. Basic Research Needs for Electrical Energy Storage: Report of the Basic Energy Sciences Workshop on Electrical Energy Storage.. In: s.l.:U.S. Department of Energy, pp. 1-7.

Govindarajan, S. N., Cox, M. D. & Berry, F. C., 1991. Survey of Harmonic levels on the Southwestern Electric Power Company System. Transactions on Power Delivery. In: s.l.:s.n., pp. 1-7.

Gupta, J. B., 1999. *Theory and Performance of Electrical Machines*. Delhi: S.K. Kataria & Sons.

Hemming, L. H., 2012. *Electromagnetic Shielding Handbook A Design and Specifications Guide*.. New York: IEEE Press..

Hong, Y., 2009. Prediction of remaining life of power transformers based on left truncated and right censored lifetime data.. In: *The Annals of Applied Statistics*. s.l.:s.n., pp. 857-879.

Johansson, P. & Andersson, B., 2008. *Comparison of Simulation Programs for Supercapacitor Modelling*.. Gothenburg, Sweden: s.n.

Jones, P. E., 2008. *Pump Station Design, Revised Third Edition*. United Kingdom: Elsevier Inc..

Judd, M. D., Yang, L. & Hunter, I. B. B., 2005. Partial discharge monitoring of power transformers using UHF sensors. Part I: sensors and signal interpretation .. In: *Electrical Insulation Magazine*. s.l.:s.n., pp. 5-14.

Khawaja, R. H., Kim, E. S., Ariastina, W. G. & Blackburn, T. R., 2013. *The Effect of High Temperature on Partial Discharges In Oil-Impregnated Insulations*. s.l., Universities Power Engineering Conference (AUPEC) 2010.

Kim, T., Adeli, H., Stoica, A. & Kang, B., 2011. *Control and Automation, and Energy System Engineering*. New York: Springer.

Labrador, P. M. & Wightman, P. M., 2009. *Topology Control in Wireless Sensor Networks*. s.l.:Springer Science and Business Media B.V..

Maxim, 2012. *Ultra-Low-Power, Open-Drain, Single/Dual-Supply Comparator*.

[Online]

Available at: datasheets.maxim-ic.com/en/ds/MAX931-MAX934.pdf

[Accessed 27 July 2012].

McEachern, A., 1993. *Voltage, Current, Power Factor, and Spectrum Measurements on Non-Sinusoidal AC Power Circuits*, Washington: Federal Construction Council.

Mclyman, C. W. T., 2004. *Transformer and Inductor Design Handbook, third edition*. s.l.:Marcel Dekker, Inc.

Microdaq, 2012. *Datalogger store*. [Online]

Available at: http://www.microdaq.com/dent_instruments/ct-logger.php

[Accessed 21 August 2012].

Mughal, O., 2008. *The Daredevil Electricians of Pakistan*. [Online]

Available at: <http://fbarea.wordpress.com/2011/09/01/the-daredevil-electricians-of-pakistan/>

[Accessed 04 July 2013].

Patel, M. R., 2005. *Spacecraft Power Systems*. Florida: Florida: CRC press.

Polastre, J., Szewczyk, R. & Culler, D., 2005. *Telos: Enabling Ultra-Low Power Wireless Research*. Fourth International Symposium on Information Processing in Sensor Networks, s.n., pp. 364 -369.

Roundy, S. J., 2003. *Energy Scavenging for Wireless Sensor Nodes with a Focus on Vibration to Electricity Conversion*. Berkeley: The University of California.

Saha, T., 2003. Review of modern diagnostic techniques for assessing insulation condition in aged transformers. *Dielectrics and Electrical Insulation, IEEE Transactions on (Volume:10 , Issue: 5)*, pp. 903 - 917.

Sahay, K. & Dwivedi, B., 2009. Supercapacitors Energy Storage System for Power Quality Improvement: An Overview.

Shastalore, n.d. *Portable 12 Volt 17 Watt Wind Generator with Automatic Furling*. [Online]

Available at: <http://www.instructables.com/id/Portable-12-Volt-17-Watt-Wind-Generator-with-Autom/>

[Accessed 4 June 2012].

Shuter, T. C., Vollkommer, H. T. J. & Kirkpatrick, T. L., 1989. Survey of Harmonic levels on the American Electric Power Distribution System.. *Transactions on Power Deliver*, Volume 4, pp. 1-10.

- Stefanidis, A., 2006. *The Emergence of GeoSensor Networks*. [Online]
Available at: <http://lbs360.directionsmag.com/articles/printer.php?articleid=2100>
[Accessed 15 June 2012].
- Sumper, A. & Baggini, A., 2012. Electrical Energy Efficiency: Technologies and Applications. In: New Delhi: John Wiley & Sons, LTD, p. 148.
- Suresh, P. R. & Elachola, S., 2000. *Distribution Loss of Electricity and Influence of Energy Flows: A Case Study of a Major Section in Kerala*, s.l.: s.n.
- Swarztrauber, S. & Shafrir, D., 2012. *Patent (20120313620)*, s.l.: s.n.
- Texas Instruments, 2004. *Precision Programmable Reference*. [Online]
Available at: <http://www.ti.com/lit/ds/symlink/tl431.pdf>
[Accessed 5 July 2012].
- Tian, D. & Georganas, N. D., 2002. *A Coverage-Preserving Node Scheduling Scheme for Large Wireless Sensor Networks*. New York, WSNA '02 Proceedings of the 1st ACM international workshop on Wireless sensor networks and applications.
- Townley, A., 2012. *Vibrational Energy Harvesting Using MEMS Piezoelectric Generators*, s.l.: s.n.
- Voss, G., Mattatia, S. & Bajog, G., 2005. *Interaction between power electronic components and distribution transformers - risk evaluation and mitigation techniques..* Turin, Italy, CIRED 2005. 18th International Conference and Exhibition, pp. 1-3.
- Wagener, J. C., 2009. *Design of a magnetically isolated DC-DC converter for use in cell balancing*. Cape Town (Western Cape): s.n.
- Wang, M., Vandermaar, A. J. & Srivastava, K. D., 2002. *Review of condition assessment of power transformers in service*. s.l., s.n., pp. 12 - 25.
- WBS&DCL, 2012. *TECHNICAL SPECIFICATION FOR 33/0.4KV, 100 KVA STATION SERVICE TRANSFORMER*. [Online]

Available at:

<http://www.wbsedcl.in/irj/go/km/docs/internet/webpage/techspec/33%20KV-100%20KVA-Stn%20Service%20-%20Dist.Tr-Specification.pdf>

[Accessed 15 June 2013].

Werle, P., Wasserberg, V., Borsi, H. & Gockenbach, E., 2000. *A New Protection and Monitoring System for Dry Type Transformers Based on Innovative Sensor Technologies..* Anaheim, IEEE International Symposium on Electrical Insulation, 2000, pp. 255-258.

Williams, J., 2012. *Linear Technology*. [Online]

Available at: <http://cds.linear.com/docs/Datasheet/1967f.pdf>

[Accessed 3 August 2012].

Ye, W., Heidemann, J. & Estrin, D., 2004. Medium access control with coordinated adaptive sleeping for wireless sensor networks.. *IEEE/ACM Transaction on Networking*, pp. 493-506.

Appendices

Appendix A–CT Design

Permeability calculations

The following equations from (Gupta, 1999, pp. 21-22) were used to calculate the permeability of 3C81 ferrite U-core material.

Calculating magneto motive force

$$\mathcal{F} = N_s \times I_s = 200At$$

\mathcal{F}	Magneto motive force	
N_s	Number of secondary windings	is 1000
I_s	Current in secondary winding	is 0.200A

Ampere turns provided for ferrite path

$$\mathcal{F}_f = 0.35 \times \mathcal{F} = 70At \text{ (Assume that the ferrite path takes 35\%)}$$

\mathcal{F}_f	Magneto motive force of ferrite material	
\mathcal{F}	Magneto motive force	is 200At

Ampere turns of air gap between U cores

$$\mathcal{F}_g = \mathcal{F} - \mathcal{F}_f = 130At$$

\mathcal{F}_g	Magneto motive force of air gap	
\mathcal{F}	Magneto motive force	is 200At
\mathcal{F}_f	Magneto motive force of ferrite material	is 70At

Calculating flux density in air gap

$$B_g = \frac{\mathcal{F}_g \times \mu_0}{\ell_g} = 1.361T = B_f$$

B_g	Flux density in the air gap	
\mathcal{F}_g	Magneto motive force of air gap	is 130At
μ_0	Permeability of free space	is $4\pi \times 10^{-7} H/m$
ℓ_g	Length of the air gap between two U core	is $0.12 \times 10^{-3} m$
B_f	Flux density in ferrite material	

Area of core calculation

$$A_c = \ell_c \times W_c = 207.35 \times 10^{-6} m^2$$

A_c	Core cross sectional area	
ℓ_c	Core length	is 0.0143 m
W_c	Core width	is 0.0154 m

Magnetic flux in the CT core can be calculated by the following formula:

$$\Phi = B_g \times A_c = 0.282mWb$$

Φ	Total flux	
B_g	Flux density in the air gap	is 1.361T
A_c	Core cross sectional area	is $207.35 \times 10^{-6} m^2$

Calculating core relative permeability

$$\mu_r = \frac{B_f \times \ell_{MP}}{\mu_0 \times \mathcal{F}_f} = 2676.679$$

μ_r	Relative permeability	
B_f	Flux density in ferrite material	is 1.361 T
ℓ_{MP}	Magnetic path length of U core	is 0.173 m
μ_0	Permeability of free space	is $4\pi \times 10^{-7} \text{ H/m}$
\mathcal{F}_f	Magneto motive force of ferrite material	is 70 At
μ_r	Theoretical value from datasheet	is 2700
μ_r	Calculated value	is 2677

Magnetising current

The following equation from (Mclyman, 2004, p. 34) was used to determine the magnetising current needed to magnetise the standard 3C81 ferrite material.

$$I_m = \frac{H \times \ell_{MP}}{0.4 \times \pi \times N_p} = 2.064 \text{ A}$$

I_m	Magnetising current	
H	Magnetic field intensity	is 15 A/m
ℓ_{MP}	Magnetic path length of U core	is 0.173 m
N_p	Number of primary windings	is 1

Maximum current or saturation current that will energise the core B_{max}

In order to calculate the saturation current of the transformer core, there is a sequence of calculations that have to be done to determine the current. Therefore first, known factors have to be manipulated to provide the total flux value. The following equation from (Gupta, 1999, pp. 22-24) was used to determine the core saturation current.

$$\Phi = B_{max} \times A_c = 9.330 \times 10^{-5} \text{ Wb}$$

Φ	Total flux	
B_{max}	Maximum flux density	is 0.450 T
A_c	Core cross sectional area	is $207.35 \times 10^{-6} \text{ m}^2$

Now that the flux value is known, the reluctance of the two ferrite cores and the reluctance of the air gap between them have to be calculated:

Reluctance of two identical ferrite cores are:

$$\mathcal{R}_c = \frac{\ell_{MP}/2}{\mu_0 \times \mu_r \times A_c} = 123.223 \times 10^3 \text{ At/Wb}$$

\mathcal{R}_c	Core reluctance	
ℓ_{MP}	Magnetic path length of U core	is 0.173 m
μ_0	Permeability of free space	is $4\pi \times 10^{-7} \text{ H/m}$
μ_r	Relative permeability	is 2700
A_c	Core cross sectional area	is $207.35 \times 10^{-6} \text{ m}^2$

Reluctance of the air gap between ferrite cores:

$$\mathfrak{R}_g = \frac{2\ell_g}{\mu_0 \times A_c} = 923.105 \times 10^3 \text{ At/Wb}$$

\mathfrak{R}_g	Reluctance of air gap	
ℓ_g	Length of the air gap between two U core	is $0.12 \times 10^{-3} \text{ m}$
μ_0	Permeability of free space	is $4\pi \times 10^{-7} \text{ H/m}$
A_c	Core cross sectional area	is $207.35 \times 10^{-6} \text{ m}^2$

Total reluctance of the magnetic circuit:

$$\mathfrak{R}_t = 2\mathfrak{R}_c + \mathfrak{R}_g = 1.169551 \times 10^6 \text{ At/Wb}$$

\mathfrak{R}_t	Total Reluctance	
\mathfrak{R}_c	Core reluctance	is $123.2 \times 10^3 \text{ At/Wb}$
\mathfrak{R}_g	Reluctance of air gap	is $923.1 \times 10^3 \text{ At/Wb}$

Now that the total magnetic circuit reluctance is known, the MMF (magneto motive force) of the circuit can be determined with the following equation

$$\mathcal{F} = \mathfrak{R}_t \times \Phi = 109.12 \text{ At}$$

\mathcal{F}	Magneto motive force	
\mathfrak{R}_t	Total Reluctance	is $1.169 \times 10^6 \text{ At/Wb}$
Φ	Total flux	is $9.330 \times 10^{-5} \text{ Wb}$

Now that the MMF is known, the saturation current can be calculated:

$$I_{sat} = \frac{\mathcal{F}}{N_p} = 109.12 \text{ A}$$

I_{sat}	Saturation current	
\mathcal{F}	Magneto motive force	is 109.12 At
N_p	Number of primary windings	is 1

With the above calculations, it has been determined that a current of 109.12A that flows in a single winding will produce enough current to saturation a 3C81 Ferrite core.

CT core area calculation

In order to design a current transformer that will provide a certain operational voltage, the frequency as well as the Flux density of the CT material has to be chosen first. When these parameters are known, the following equation from (Di Tian, 2002, p. 22) was used to determine the core area

Calculating the ferrite core area needed to produce an output voltage of 30V

$$A_c = \left(\frac{V_p}{2\pi \times F \times B_{max}} \right) / N_s = 0.2122 \text{ m}^2$$

A_c	Core cross sectional area	
V_p	Peak voltage	is 30V
F	Frequency	is 50Hz
B_{max}	Maximum flux density	is 0.450T
N_s	Number of secondary windings	is 1

This core will be to large, therefore more windings have to be added to reduce this area

$$A_c = \left(\frac{V_p}{2\pi \times F \times B_{max}} \right) / N_s = 212.206 \times 10^{-6} m^2 \text{ or } 212 mm^2$$

A_c	Core cross sectional area	
V_p	Peak voltage	is30V
F	Frequency	is50Hz
B_{max}	Maximum flux density	is0.450T
N_s	Number of secondary windings	is1000

From Ferroxcube a practical core was chosen with a cross sectional area of:

$$A_c = 204 mm^2 (U67/27/14)$$

New voltage calculation

$$V_p = 2\pi \times F \times B_{max} \times A_c \times N_s = 28.84 V$$

V_p	Peak voltage	
F	Frequency	is50Hz
B_{max}	Maximum flux density	is0.450T
A_c	Core cross sectional area	is204 $\times 10^{-6} m^2$
N_s	Number of secondary windings	is 1000

$$V_{rms} = 0.707 \times V_p = 20.39 V$$

V_{rms}	Maximum RMS voltage	
V_p	Peak voltage	is 28.84 V

According to the above formula, when using a Ferrite 3C81 core with a cross sectional area of 204 mm² will produce an output voltage of 28.84 V_(peak)

Power output of CT wounded with AWG 25

The power output of this CT was determined by providing the CT with a constant primary source current of 120A_{rms}. With variation in the load magnitude, different power outcomes have been noticed.

$$R_{max} = \frac{V_{rms}}{I_{rms}} = 169.92 \Omega$$

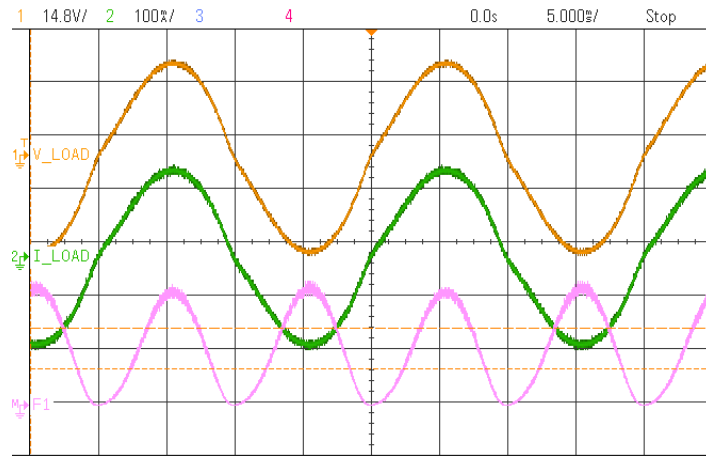
R_{max}	Maximum load resistance	
V_{rms}	Maximum RMS voltage	is20.39 V
$I_{s(rms)}$	Typical secondary RMS current	is 0.12A

The following section focuses on two of those outcomes, the first being the power output at a load of 170Ω. This load was chosen because it indicates the CT power output before the core saturates.

$$P_{170\Omega} = (I_{s(rms)})^2 \times R_{170\Omega} = 2.448W$$

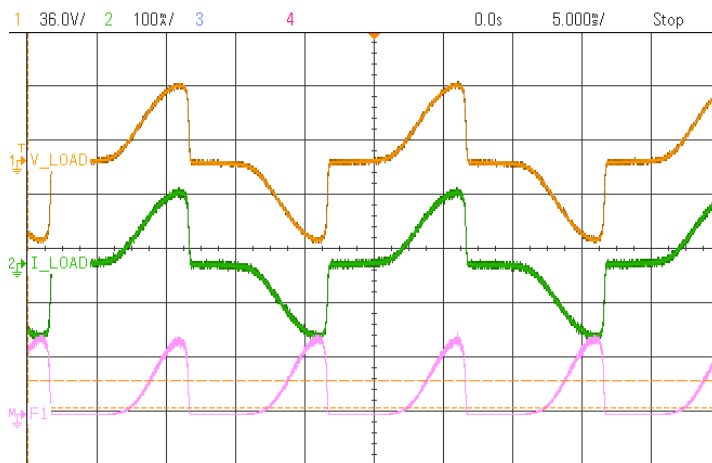
According to the equation above, the maximum theoretical power at 120A_{rms} that the transformer should deliver is $P_{170\Omega} = 2.448W$.

Consequently the measured V_{rms} before saturation is 19.26V, $I_{s(rms)}$ is 114.11mA and Power is 2.195W, notice that the two powers are similar and the voltages and currents are almost sinusoidal, however does show signs of saturation due to a reduction in the load current from 120mA.

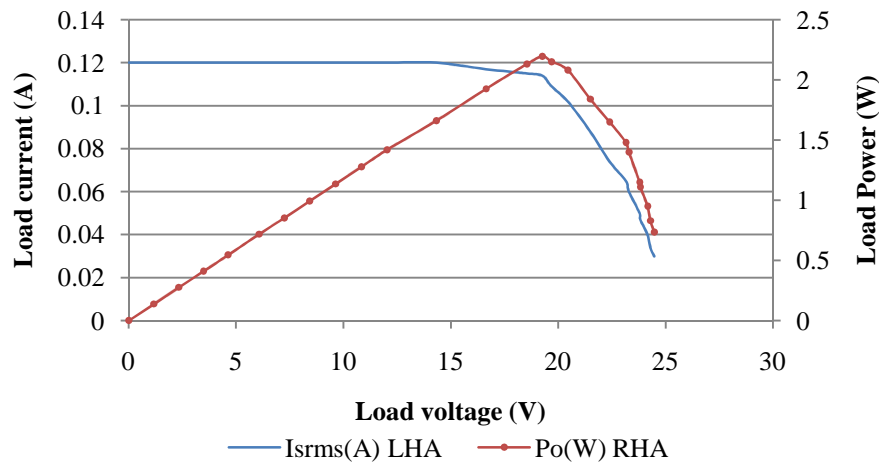


After saturation

After saturation the power output of this CT started to reduce due to the distortion of the output current as shown below



Actual measured Load voltage, current and power



Acceptable core losses

The following section from (Mclyman, 2004) is an indication of the theoretical power that will be lost when the CT is in its operational state.

$$P_{fe} = P_o \times \frac{5}{100} = 122.4mW$$

P_{fe}	Acceptable core losses	
P_o	Power output	is 2.448W

According to the top equation, the allowable power loss in the core at maximum power was calculated to be 122.4mW. Now that the estimated amount of power loss was calculated at 5%, the theoretical power loss can be calculated to know whether the core is efficient enough for this energy harvesting process.

The following equation will be used to determine acceptable power loss according to the weight of the CT core material.

$$Loss_{mW/g} = \frac{P_{fe}}{Wt_{fe}} = 0.72mW/g$$

$Loss_{mW/g}$	Power loss according to the weight	
$P_{fe_{Bs}}$	Acceptable core losses before saturation	is 122.4mW
Wt_{fe}	Core mass	is 170 g

Flux density calculated

$V_{p_{new}}$ is the peak voltage when the CT has a 170Ω load on it, therefore the voltage is reduced from the open source voltage which means that with a lower voltage B_{max} will also decrease. The equation from (Di Tian, 2002, p. 22) was used to determine the new B_{max} value.

According to CT tests with 120A_{rms} primary current and a 170Ω load, the tests indicated a V_{rms} of 19.26V. To apply this voltage to the flux density equation, it must first be converted to V_p .

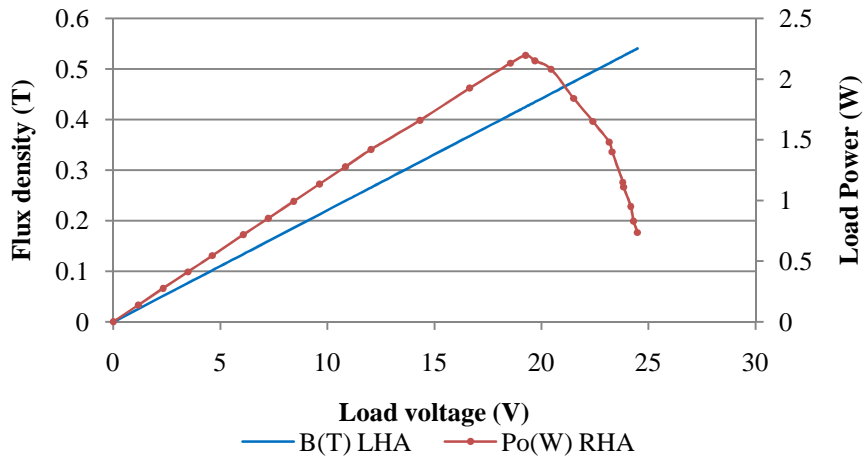
$$V_{p_{Bs}} = V_{rms} \times \sqrt{2} = 27.238V$$

$V_{p_{Bs}}$	Peak voltage before saturation	
V_{rms}	RMS voltage	is 19.26V

$$B_{Bs} = \frac{V_{p_{Bs}}}{(2\pi \times F \times N_s \times A_c)} = 425 mT$$

B_{Bs}	Flux density before saturation	
$V_{p_{Bs}}$	Peak voltage before saturation	is 27.238 V
F	Frequency	is 50Hz
N_s	Number of secondary windings	is 1000
A_c	Core cross sectional area	is $204 \times 10^{-6}m^2$

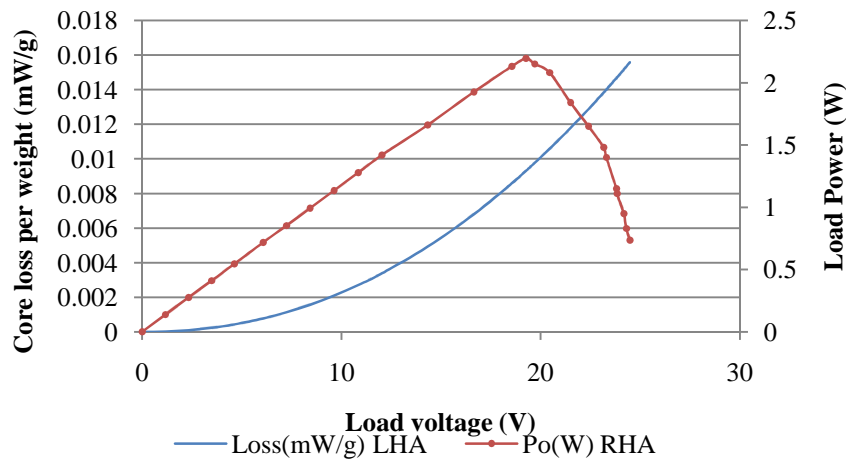
Using these equations and the measures data the same can be done for the rest of the measurements, resulting in the graph that follows



Now that the flux densities at specific operation voltages are known, the theoretical power that will be lost during operation can be calculated using the equation from (Mclyman, 2004, pp. 444-445).

$$Loss_{mW/g} = 0.000179 \times F^{1.48} \times B_{max}^{2.15}$$

$Loss_{mW/g}$	Core power loss according to the weight	
F	Frequency	is 170 g
B_{max}	Maximum flux density	

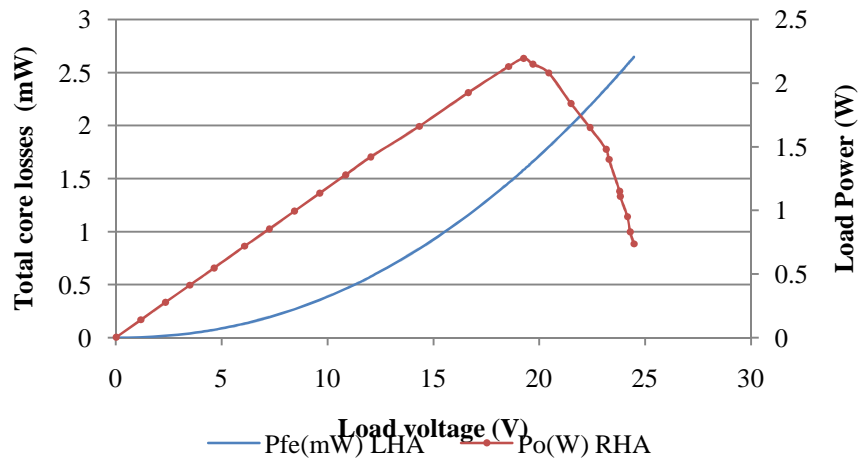


Total core losses P_{fe} in Watts

This calculation will indicate the total theoretical power loss in watts caused by the core in operational state.

$$P_{fe} = Wtfe \times Loss_{mW/g} = 1.440mW$$

P_{fe}	Core losses	
$Wtfe$	Core mass	is 170 g
$Loss_{mW/g}$	Core power loss according to the weight	



Induced core error

Before saturation:

$$\text{Core losses induced error} = \left(\frac{Pfe_{Bs}}{Po_{Bs}} \right) \times 100 = 0.07198\%$$

Pfe_{Bs}	Core losses before saturation	is 1.58mW
Po_{Bs}	Power output before saturation	is 2.195W

In the beginning of this calculation it was estimated that a total power loss of 5% would be tolerable, however with the calculations above, it was determined that the 3C81 ferrite material would cause 0.072 % of the total power to be lost before the core is saturated. The core losses are exceptionally low. This is likely related to the low frequency at which they are excited at. Therefore the 3C81 ferrite material will be an effective material to use for this energy harvesting CT design.

Wire calculations

Calculating the wire thickness of the CT and the amount of current that it will be able to handle. According to (Mclyman, 2004, p. 504), a 1 cm^2 will be able to handle continuous current flow of 400 A. The following calculations were based on the above statement.

$$J = \frac{I}{A} = 4 \times 10^6 \text{ A/m}^2$$

J	Current density	
I	Electric current	is 400A
A	Area	is 0.0001m^2

The following equation will determine the wire diameter that will be able to withstand a current flow of 0.2A.

$$A_c = \frac{I}{J} = 50 \times 10^{-9} \text{ m}^2 \text{ or } 0.05\text{mm}^2$$

A_c	Area of conductor	
I	Rated electric current	is 0.2A
J	Current density	is $4 \times 10^6 \text{ A/m}^2$

Looking at the standard AWG, the gauge factor that is the closest to the calculated value is the AWG 30, which has a A_c of 0.03203 mm^2 .

Hence with a wire with a A_c of 0.0509 mm^2 will be able to handle a current of 200 mA .

To ensure that the wire will not add additional heat to the transformer, the A_c has to be increased. In order to save cost on the project it was decided to use the copper wire with AWG values of 29, 27, and 25 to wind three current transformers for testing purposes.

CT winding resistance

The CT that was wined with AWG 25 was used to calculate the winding resistance as well as the copper losses that the transformer endures.

$$R_s = \ell_{MTL} \times N \times \frac{\Omega}{\text{km}} = 6.222\Omega$$

R_s	CT resistance	
ℓ_{MTL}	Mean length in, turn per m (Ferroxcube datasheet) is $58.6 \times 10^{-3} \text{ m}$	
N_s	Number of secondary windings	is 1000
$\frac{\Omega}{\text{km}}$	Resistance per kilometre	is $106.173 \Omega/\text{km}$

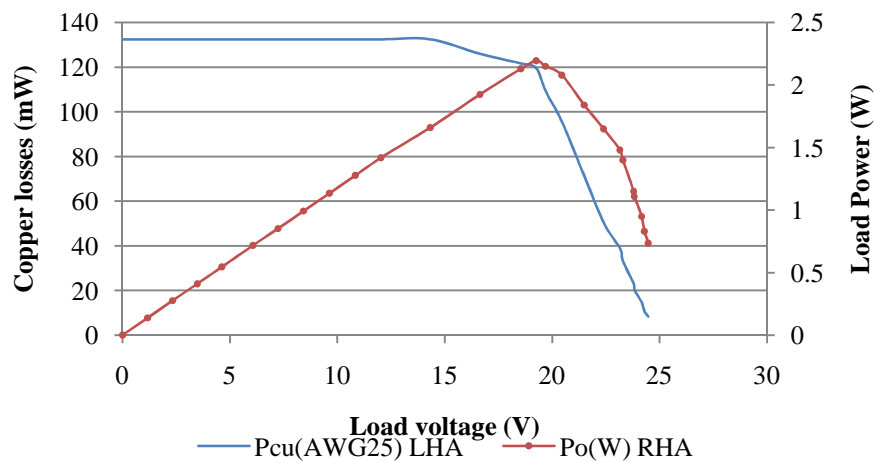
The theoretical impedance of the CT was calculated to be 6.221Ω and measured value was 9.2Ω

Copper Losses

The copper losses will be calculated according to the measured impedance of the CT. and the measures currents

$$P_{cu} = (I_s)^2 \times R_s$$

P_{cu}	Total power lost in transformer windings	
I_s	RMS secondary current	
R_s	Resistance per kilometre	is 9.2Ω



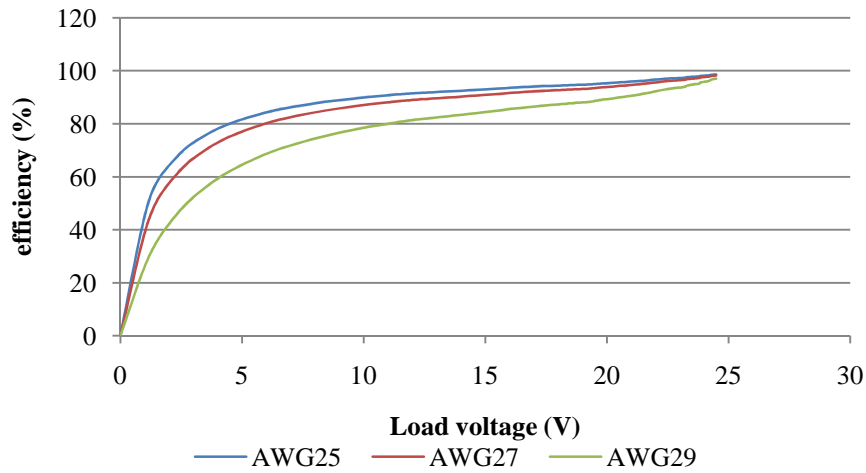
The maximum copper losses in the CT is 132 mW , which can be reduced by using thicker wire. The previous equations were repeated for AWG 27 with a resistance of

12.2Ω and AWG 29 with a resistance of 22.5Ω to determine the power and efficiency characteristics for CT's using the same core but different wire diameters.

$$P_{in} = P_{cu} + P_{fe} + P_o$$

$$\eta = \left(\frac{P_o}{P_{in}} \right) \times 100$$

P_{in}	Input Power
P_{cu}	Total power lost in transformer windings
P_{fe}	Core losses
P_o	Power output
η	Efficiency



Voltage regulator

The output voltage of the TL431CLP high current shunt regulator was determined by the following equation obtained from its datasheet.

$$R1 = \left(\frac{V_o}{V_{ref}} - 1 \right) \times R2 = 50k\Omega$$

$R1$	Unknown Resistor value	
V_o	Output voltage	is 3.6V
V_{ref}	Reference voltage	is 2.4V
$R2$	Chosen Resistor value	is 100kΩ

The closest E12 resistance value to 50 kΩ is 47 kΩ. Therefore by using a 47 kΩ resistor in the equation, the theoretical output voltage of the precision regulator should be:

$$V_o = \left(1 + \frac{47k\Omega}{100k\Omega} \right) \times 2.4V = 3.528 V$$

With the above calculation done, it was determined that the theoretical output voltage of the precision regulator should be 3.528 V.

Storage capacitance calculation

The following calculation illustrates the capacitance magnitude when capacitors are placed in series with one another.

$$C_{total} = \frac{1}{\frac{1}{C_1} + \frac{1}{C_2}} = 35F$$

C_{total} Total capacitance
 C_1, C_2 Capacitance is 70F

With the use of the above equation it was determined that the capacitance magnitude changes to 35 F when two capacitors with an initial magnitude of 70 F are placed in series.

Charge time calculation

The following section is a theoretical capacitor charge estimation, when a capacitor is charged with a charge current of 0.12 A_{rms} from the CT. The following equation form (Floyd, 2005, p. 666) was used to determine the charge time of the capacitor.

$$Q = I_c \times t, \quad Q = C \times V_c, \quad I_c \times t = C \times V_c$$

$$t = \frac{C \times V_c}{I_c}$$

Q Capacitor charge
 I_c Charging current (A)
 t Time (s)
 C Capacitor capacitance (F)
 V_c Capacitor voltage (V)

The maximum charge time was calculated when the primary transformer would be operating at a theoretical current per phase which is 120 A_{rms} . Hence the CT would produce 0.12 A_{rms} to charge the capacitor with:

$$t = \frac{35 \times 3.6}{0.12} = 1050 \text{ s or } 17\text{min and } 30\text{sec}$$

The minimum current that will be measured by the CT, is when the primary transformer is delivering 5 A_{rms} on its primary winding. Consequently the CT will produce a charging current of 0.005 A_{rms} to charge the capacitor with.

$$t = \frac{35 \times 3.6}{0.005} = 25200 \text{ s or } 420\text{min}$$

According to the above equations it will take 17min and 30 sec to charge the capacitor at a constant current of 0.120 A_{rms} , however when charging the capacitor with the

absolute minimum current of 0.005 V it will take 7 hours not considering any losses to charge the capacitor from 0V to the 3.6 operational voltage.

Hysteresis band calculation

The following equations from (Maxim, 2012, p. 10) were used to calculate the hysteresis band of the electronic circuit.

$$R_3 = \frac{V_{HB}}{2 \times I_{ref}}$$

R_3	Resistor value
V_{HB}	Voltage of the Hysteresis band
I_{ref}	Reference current

For equation 41, V_{HB} can be any value between 0 and 100 mV, therefore a value of 85mV was chosen. I_{ref} can have any value between 0.4 μA and 4 μA . Therefore it was decided to use 0.5 μA as I_{ref} .

$$R_3 = \frac{85 \text{ mV}}{2 \times 0.5 \mu A} = 85 \text{ k}\Omega$$

Because 85k Ω is not in the E12 range, it was decided to choose the closest resistance to it. Hence $R_3 = 82 \text{ K}\Omega$

$$R_4 = \frac{(V_{ref} - \frac{V_{HB}}{2})}{I_{ref}}$$

R_4	Resistor value
V_{HB}	Voltage of the Hysteresis band
I_{ref}	Reference current

According to the datasheet of MAX931 (Maxim, 2012, p. 9) the reference voltage of the IC is at a fixed value of 1.182 V.

$$R_4 = \frac{1.182 - \frac{85 \text{ mV}}{2}}{0.5 \mu A} = 2.279 \text{ M}\Omega$$

The calculated value of R_4 is not a E12 value therefore the closest value of 2.2 M Ω was chosen for R_4

Upper and lower threshold voltage calculation

It was decided that an upper threshold voltage of 3.1V will be adequate for the electronic design. With this chosen value, a voltage divider between R_1 and R_2 was done to determine a value close to the original upper threshold value.

$$V_{Uth (original)} = V_{ref} + \left(\frac{V_{HB}}{2}\right) = 1.182 + \left(\frac{85 \text{ mV}}{2}\right) = 1.224 \text{ V}$$

Now that this value is known, the resistive values can be determined.

$$V_{Uth (new)} = \frac{V_{Uth (original)} \times (R1+R2)}{R2}$$

With the top equation, all of the variables are known except for the 2 resistance values. It was therefore decided to choose $R2$ to be $1M\Omega$, to solve the equation to determine $R1$.

$$\begin{aligned} R1 &= \left(\frac{(V_{Uth (new)} \times R2) - V_{Uth (original)} \times R2}{V_{Uth (original)}} \right) \\ &= \left(\frac{(3.1 \times 1 M\Omega) - (1.224 \times 1 M\Omega)}{1.224 V} \right) = 1.53M\Omega \end{aligned}$$

With the top equation, it was determined that $R1$ will have to have a value of $1.53 M\Omega$ to provide a $V_{Uth (new)}$ of $3.1 V$. The closest E12 value to the calculated value is $1.5M\Omega$, therefore the new $R1$ will be $1.5M\Omega$. With this change in $R1$, the new $V_{Uth (new)}$ was calculated to be $3.06 V$.

Now that the values of $R1$ and $R2$ are known, the lower threshold can be calculated. The same procedure has to be followed for $V_{Lth (new)}$.

$$\begin{aligned} V_{Lth (original)} &= V_{ref} - \left(\frac{V_{HB}}{2} \right) = 1.182 - \left(\frac{85 mV}{2} \right) = 1.139 V \\ V_{Lth (new)} &= \frac{V_{Uth (original)} \times (R1 + R2)}{R2} = \frac{1.139 V \times (1.5 M\Omega + 1 M\Omega)}{1 M\Omega} = 2.848 V \end{aligned}$$

With the calculation above, $V_{Lth (new)}$ has been determined to have a value of $2.848 V$. Now that both the upper and the lower threshold values are known, the new Hysteresis band can be calculated.

$$V_{HB (new)} = V_{Uth (new)} - V_{Lth (new)} = (3.06 - 2.848) = 0.213 V$$

From this calculation notice that by adding in the resistor divider, the Hysteresis band increased from $85mV$ to $213mV$ which leaves a bigger operational band for the WSN.

Capacitor C1 charge time calculation

The following calculation was done to determine the total charge time it will take for capacitor $C1$ to charge to its maximum potential with the minimum and maximum currents the current monitoring system was designed for.

The maximum current that will flow into the current measurement section when the transformer is operating at a typical potential, is $120 A_{rms}$. Therefore the first charge time will be calculated by using $0.120 A_{rms}$ (CT out at a primary current of $120 A_{rms}$).

The maximum voltage the capacitor should charge too can be determined with Ohms law.

$$V = I \times R$$

$$V_{C1} = (R_{shunt} // Pot1) \times I1$$

To calculate the highest voltage the capacitor C1 will be charged to, it will be assumed that $Pot1 = 0\Omega$. Therefore $R_{shunt} = 15\Omega$.

$$V_{C1} = (R_{shunt}) \times I1 = 15 \times 0.12 = 1.8 V$$

To calculate the minimum voltage that V_{C1} will be charged to, $Pot1$ will be at its maximum of $1K\Omega$.

$$V_{C1} = (R_{shunt} // Pot1) \times I1 = (15 // 1K) \times 0.1 = 1.7734 V$$

Note that there is a difference of 26.6 mV between these two calculated values. This voltage difference will be used to calibrate the current measurement device.

In order to calculate the time the capacitor will take to charge to its potential, the following equation was used from (de Villiers, 2009, p. 19).

Charge time to 1.8 V when $R = 15\Omega$

$$V(c) = V(1 - e^{-\frac{t}{RC}})$$

$$t = -RC \times \ln\left(1 - \frac{V(c)}{V}\right) = -100K\Omega \times 1\mu F \times \ln\left(1 - \frac{1.79}{1.8}\right) = 519 s$$

$V(c)$	Instantaneous voltage across capacitor
V	Applied voltage
R	Charging resistance
C	Capacitance

Ripple calculation

The following calculations were done to indicate the effect the capacitor voltage ripples has on the current output reading. The WSN has an internal reference voltage that is programmed into the device. This reference voltage is directly proportional to a 12 bit value as well as the output current from 0 to 200A.

$$WSM_{Vref} = 2.5V$$

$$12 \text{ bit value} = 2^{12} = 4096$$

Therefore measuring between 0 and 2.5 V is directly proportional to the ration 0 to 4096.

$$\text{Bit value} = \frac{V_{cap}}{V_{ref}} \times 4096$$

The voltage or bit value measured is directly proportional to 0 to 200A. The following equation therefore illustrates how the current measurement is achieved.

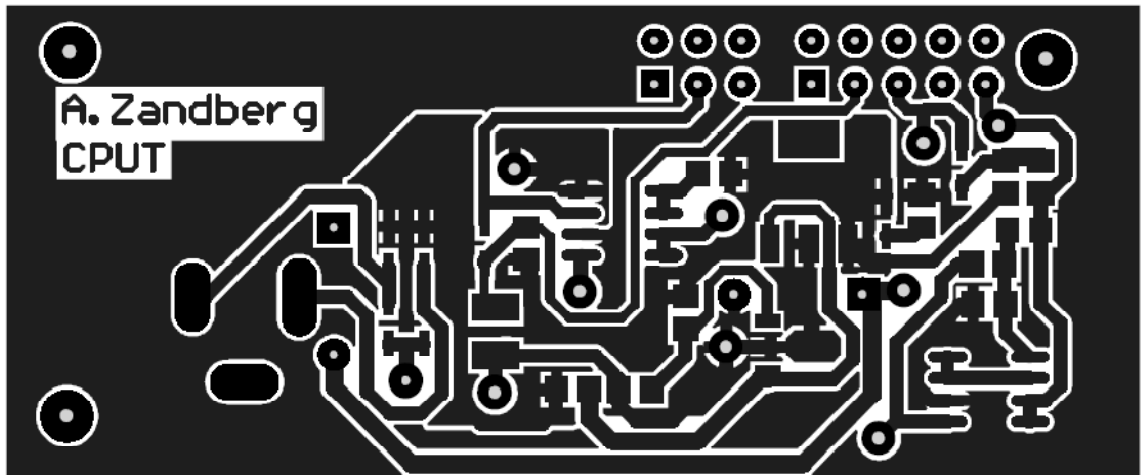
$$I_{prim} = \frac{V_{cap}}{V_{ref}} \times 200 \text{ A]$$

Alternatively:

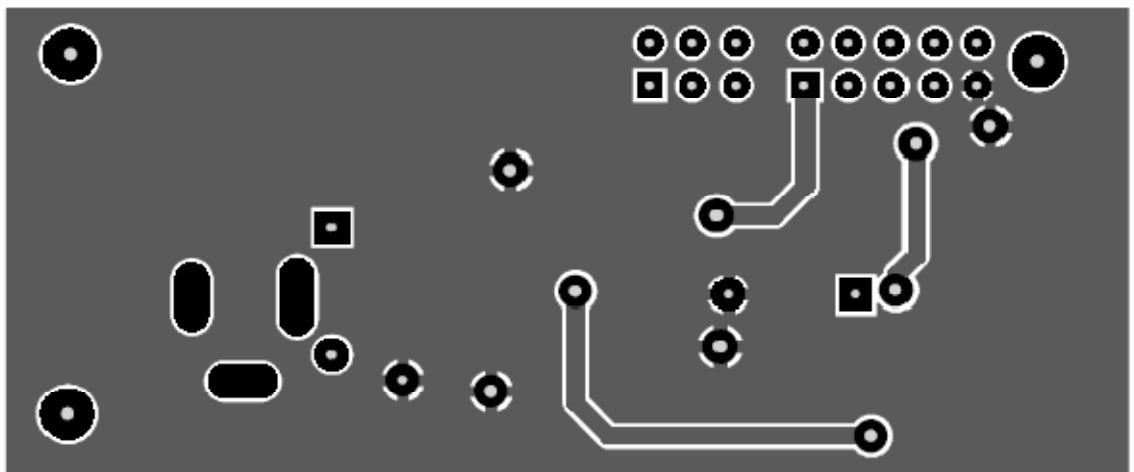
$$I_{prim} = \frac{\text{Bit value measured}}{12 \text{ Bit value}} \times 200 \text{ A}$$

Therefore with a ripple value of 45.5mV the current output will have a maximum swing of:

$$I_{swing} = \frac{V_{cap}}{V_{ref}} \times 200\text{A} = \frac{45.5 \text{ mV}}{2500 \text{ mV}} \times 200\text{A} = 3.64 \text{ A}$$



PCB layout top view



PCB layout bottom view

Appendix C– Calibration procedure

- 1) Select the standard off-the-shelf ammeter against which the new ammeter is to be calibrated
 - a) Fluke 189 True RMS multimeter has been selected to serve as a reference meter.
 - Standard meter description
 - 1.5% + 20
 - ISO 9001 P/N 1589971 Rev. 1 6/2005
 - b) Fluke 80i 500s Ac Current Probe used with the reference meter (off-the-shelf)
 - 1A – 500A Ac Rms
 - 5Hz – 10 KHz
 - Working Voltage 600V Cat III
- 2) Select supply source according to the range of meter
 - a) Supply source is an Agilent 33120A Waveform Generator that feeds into a
 - b) Crest Audio Amplifier. The Crest Amplifier feeds directly into a
 - c) Current simulation rig, consisting of 40 insulated copper wire loops.
- 3) Laboratory ambient temperature
 - a) Lab conditions at 21° Celsius
- 4) Connect the reference meter in series with the calibration circuit
 - a) Remember that the test rig has 40 current loops therefore the current measured by the reference meter has to be multiplied by a factor of 40 to determine the actual current that would be detected by the CT's.
- 5) Connect the off-the-shelf CT onto the calibration circuit
- 6) Connect new CT also to the calibration circuit.
- 7) Output of New CT is converted to a 12 bit value
- 8) Insert primary current of 3A (rms) into the current simulation rig. Calibrate the new CT to read 120 A_{rms} . After calibration of the CT run accuracy tests over the entire current range of the new CT.
- 9) Increase the Current in suitable steps of 10 Amps from 5 to 120 Amps and back to 5 again. Note comparative readings between reference fluke meter, off-the-shelf CT and new CT.
- 10) Calculate % Error & determine calibration Status by comparing % Error with % accuracy/error claimed.
- 11) Repeat the above steps 9 and 10 for at least five times and estimate the measurement uncertainty.
- 12) Prepare the calibration report showing the expanded uncertainty in measurement at a 95 % of confidence level for a coverage factor of $K = 2$

Appendix D – WSN program

The program used to operate the WSN is a re-written and edited version of the original Oscilloscope available with TinyOs. The program was edited to be able to activate General I/O pins, as well as take voltage readings using ADC0 and ADC1. The source code used is constructed out of sections **OscilloscopeC.nc**, **OscilloscopeAppC.nc**, **Oscilloscope.h**, **MyadcC.nc**, **MyadcP.nc**, **MyadcCs2.nc**, **MyadcPs2.nc**.

OscilloscopeC.nc

```
/*
 * Copyright (c) 2006 Intel Corporation All rights reserved.
 * This file is distributed under the terms in the attached INTEL-LICENSE file. If you do not
 * find these files, copies can be found by writing to Intel Research Berkeley, 2150
 * Shattuck Avenue, Suite 1300, Berkeley, CA, 94704. Attention: Intel License Inquiry.
 * Oscilloscope demo application. See README.txt file in this directory. @author David Gay
 */
#include "Timer.h"
#include "Oscilloscope.h"
module OscilloscopeC @safe()
{
  uses {
    interface Boot;
    interface SplitControl as RadioControl;
    interface AMSend;
    interface Timer<TMilli> as PeriodTimer;
    interface Timer<TMilli> as HighTimer;
    interface Timer<TMilli> as ReadingTimer;
    interface Read<uint16_t> as CurrentRead;
    interface Read<uint16_t> as BatteryRead;
    interface GeneralIO as GPIO;
    interface GeneralIO as GPIO2;
    interface Leds;
  }
}
implementation
{
  task void sendData();
  message_t sendBuf;
  bool sendBusy;
  uint8_t adcCount;
  uint16_t readings[ADCCOUNT+1];
  /* Current local state - interval, version and accumulated readings */
  oscilloscope_t local;
  uint8_t reading; /* 0 to NREADINGS */
  /*
   * When we head an Oscilloscope message, we check it's sample count. If it's ahead of ours,
   * we "jump" forwards (set our count to the received count). However, we must then suppress
   * our next count increment. This is a very simple form of "time" synchronization (for an
   * abstract notion of time).
   */
  bool suppressCountChange;
  void startTimer();
  /* Use LEDs to report various status issues */
  void report_problem(void) { /* call Leds.led0Toggle(); */ }
  void report_sent() { /* call Leds.led1Toggle(); */ }
```

```
void report_received() { /*call Leds.led2Toggle();*/ }
/* Boot.booted() indicates start of the program */
event void Boot.booted() {
// Make pin23 an output and make it low
call GPIO.makeOutput();
call GPIO.clr();
// make pin 26 an output, for testing ripple samples
call GPIO2.makeOutput();
call GPIO2.clr();
// When data packet transmission is not active
sendBusy = FALSE;
adcCount = 0;
/* Set the local interval (period) to PERIODINTERVAL defined in Oscilloscope.h*/
local.interval = PERIODINTERVAL;
// Local mote ID set at compile time
local.id = TOS_NODE_ID;
local.count = 0;
startTimer();
} /* End of Boot.booted() */
/* Starting Periodic timer, and set readings in data package to 0 */
void startTimer() {
call PeriodTimer.startPeriodic(local.interval);
reading = 0;
}
/*Fire indicates the end of Periodtimer. When timer is fired, GPIOpin 23 will be set high.*/
event void PeriodTimer.fired() {
//Set pin23 high
call GPIO.set();
/*
* Set a single-short timer to some time units in the future. Replacesany current timer settings.
* Equivalent to startOneShotAt(getNow(),dt). The <code>fired</code> will be signalled when
* the timerexpires. @param dt Time until the timer fires.When PeriodTimer is fired,
* immediately the HighTimer (startOneshot) will be started, thus GPIO will remain in high
* state.
*/
call HighTimer.startOneShot(HIGHINTERVAL);
}
/*
* Hightimer.fired() indicates that the timer has finished and the following actions will take
* place.
*/
event void HighTimer.fired() {
/*
* This function calls the ADC to read the voltage that a capacitor has been charged to known as
*CurrentRead.read()if current read is not a success report the problem
*/
if (call CurrentRead.read() != SUCCESS)
report_problem();
}
/* If data reading is ffff, report problem */
event void CurrentRead.readDone(error_t result, uint16_t data) {
/*
* Allocating storage for 3 different variable integer values, sample,storage, and the average
* value calculated
*/
}
```

```
    */
uint8_t i;
uint16_t store;
uint16_t average;
if (result != SUCCESS)
    {
        data = 0xffff;
        report_problem();
    }
readings[adcCount] = data;
/*
 * call GPIO as a toggle function. This means that, each time that the code gets to toggle, the
 * pin will change from state and remain in that state until the program has executed the toggle
 * command again.
 */
call GPIO2.toggle();
/*
 * Increment adcCount until it reaches the value of ADCCOUNT, once it has reached that
 * value, get out of the loop and go to the next section
 */
adcCount++;
if(adcCount < ADCCOUNT)
    {
    call CurrentRead.read();
    }
/*
 * Store current reading measured at the capacitor in store. Each time i < ADCCOUNT, i will
 * be incremented, and the next measuring will be placed in store and added to the old one, thus
 * adding the amount of measurements that ADCCOUNT is set to.
 */
else
    {
    adcCount = 0;
    store = 0;
    for(i = 0; i < ADCCOUNT; i++)
        {
        store = store + readings[i];
        }
/*
 * Set store to the first reading slot or first package slot. After that, calculate the average of the
 * ripple on the measurecapacitor and set that to average, insert it into the second package slot
 * when calculating the average, the miner will be displayed in slot 3 of the package
 */
// local.readings[0] = store;
average = store / ADCCOUNT;
local.readings[0] = average;
average = store % ADCCOUNT;
local.readings[1] = average;
/*
 * This function calls the ADC2 to read the voltage which the Super capacitor has been charged
 * to known as BatteryRead.read()if current read is not a success report the problem
 */
if (call BatteryRead.read() != SUCCESS)
    report_problem();
```

```
    }
  }
  event void ReadingTimer.fired() {
  // repeat loop until adcCount = ADCCOUNT
  call CurrentRead.read();
  }
  /* If the reading was not successful report problem */
  event void BatteryRead.readDone(error_t result, uint16_t data) {
  if (result != SUCCESS)
    {
      data = 0xffff;
      report_problem();
    }
  // If reading wassuccessful, increment counter
  local.readings[3] = data;
  local.count++;
  // Set pin23 low
  call GPIO.clr();
  if (call RadioControl.start() != SUCCESS)
    report_problem();
  }
  event void RadioControl.startDone(error_t error) {
  post sendData();
  }
  event void RadioControl.stopDone(error_t error) {
  }
  /*
  * When the message is sent, status will be successful. If that is not true indicate the problem
  */
  event void AMSend.sendDone(message_t* msg, error_t status) {
  if (status == SUCCESS)
    report_sent();
  else
    report_problem();
  sendBusy = FALSE;
  if (call RadioControl.stop() != SUCCESS)
    report_problem();
  }
  task void sendData()
  {
  // Build and send packet
  if (sendBusy == FALSE)
    {
  // memory copy (destination address, source address, amount to copy)
  memcpy(call AMSend.getPayload(&sendBuf, sizeof(local)), &local,
  sizeof local);
  if (call AMSend.send(AM_BROADCAST_ADDR, &sendBuf, sizeof local) ==
  SUCCESS)
    sendBusy = TRUE;
  if (sendBusy == FALSE)
    report_problem();
  }
  else
  {
```

```
    report_problem();
  }
}
}
```

OscilloscopeAppC.nc

```
/*
 * Copyright (c) 2006 Intel Corporation All rights reserved.
 * This file is distributed under the terms in the attached INTEL-LICENSE file. If you do not
 * find these files, copies can be found by writing to Intel Research Berkeley, 2150 Shattuck
 * Avenue, Suite 1300, Berkeley, CA, 94704. Attention: Intel License Inquiry.
 * Oscilloscope demo application. Uses the demo sensor - change the new DemoSensorC()
 * instantiation if you want something else. See README.txt file in this directory for usage
 * instructions. @author David Gay
 */
configuration OscilloscopeAppC { }
implementation
{
  components OscilloscopeC;
  components MainC;
  OscilloscopeC.Boot -> MainC;
  components ActiveMessageC;
  OscilloscopeC.RadioControl -> ActiveMessageC;
  components new AMSenderC(AM_OSCILLOSCOPE);
  OscilloscopeC.AMSend -> AMSenderC;
  components new TimerMilliC() as PeriodTimerC;
  OscilloscopeC.PeriodTimer -> PeriodTimerC;
  components new TimerMilliC() as HighTimerC;
  OscilloscopeC.HighTimer -> HighTimerC;
  components new TimerMilliC() as ReadingTimerC;
  OscilloscopeC.ReadingTimer -> ReadingTimerC;
  components new MyAdcC() as CurrentSensorC;
  OscilloscopeC.CurrentRead -> CurrentSensorC;
  components new MyAdcCs2() as BatterySensorC;
  OscilloscopeC.BatteryRead -> BatterySensorC;
  components HplMsp430GeneralIO as GeneralIO;
  components new Msp430GpioC() as GPIO;
  GPIO -> GeneralIO.Port23;
  OscilloscopeC.GPIO -> GPIO;
  components new Msp430GpioC() as GPIO2;
  GPIO2 -> GeneralIO.Port26;
  OscilloscopeC.GPIO2 -> GPIO2;
  components LedsC;
  OscilloscopeC.Leds -> LedsC;
}
```

Oscilloscope.h

```
/*
 * Copyright (c) 2006 Intel Corporation All rights reserved.
 * This file is distributed under the terms in the attached INTEL-LICENSE file. If you do not
 * find these files, copies can be found by writing to Intel Research Berkeley, 2150 Shattuck
 * Avenue, Suite 1300, Berkeley, CA, 94704. Attention: Intel License Inquiry.
 */
// @author David Gay
```



```
#ifndef OSCILLOSCOPE_H
#define OSCILLOSCOPE_H
enum {
/*
*Number of readings per message. If you increase this, you may have to increase the
* message_t size.
*/
NREADINGS = 10,
PERIODINTERVAL = 8192,
HIGHINTERVAL = 1024,
READINTERVAL = 1,
ADCCOUNT = 10,
AM_OSCILLOSCOPE = 0x93
};
typedef nx_struct oscilloscope {
nx_uint16_t version; /* Version of the interval. */
nx_uint16_t interval; /* Sampling period. */
nx_uint16_t id; /* Mote id of sending mote. */
nx_uint16_t count; /* The readings are samples count*NREADINGS onwards */
nx_uint16_t readings[NREADINGS];
} oscilloscope_t;
#endif
```

MyAdcC.nc

```
/*
* Generic ADC component - module. Refer to the files in tos/chips/msp430/adc12
* In particular: Msp430Adc12.h and README.txt Also check the pin outs (and other data)
* in the TMote Sky datasheet and the MSP430x1xx Family User's Guide (chapter 17).
*/
generic configuration MyAdcC() {
provides interface Read<uint16_t>;
}
implementation {
/*
* The ADC Read Client provides the means for reading ADC values. It automatically does
* resource reservation, reference voltage configuration, ADC configuration and returns the
* sampled value to the calling application. There are alternative Clients available.
*/
components new AdcReadClientC();
Read = AdcReadClientC;
components MyAdcP;
/*
* This is where we tell the ADC Read Client that it can get the ADC configuration structure
* from MyAdcP
*/
AdcReadClientC.AdcConfigure -> MyAdcP;
}
```

MyAdcP.nc

```
#include "Msp430Adc12.h"
/*
* Generic ADC component - module. Refer to the files in tos/chips/msp430/adc12
* In particular: Msp430Adc12.h and README.txt Also check the pin outs (and other data)
* in the TMote Sky datasheet and the MSP430x1xx Family User's Guide (chapter 17).
```

```
*/
module MyAdcP {
provides interface AdcConfigure<const msp430adc12_channel_config_t*>;
}
implementation {
/*
 * This structure defines the operation of the ADC channel Generally, you won't need to touch
 * most of the fields
 */
msp430adc12_channel_config_t config = {
/*
 * inch: This selects the ADC channel to be used. There are 8 external ADC channels as part of
 * the MSP430 (see Msp430Adc12.h) The standard TelosB/TMote Sky mote only provides 6
 * channels (see datasheet)
 */
inch: INPUT_CHANNEL_A0,
/*
 * sref: This selects the voltage reference source for positive and negative (or ground) reference
 * voltage. Do not change (unless you have custom hardware)
 */
sref: REFERENCE_VREFplus_AVss,
/*
 * ref2_5v: There are 2 internal reference voltage options of 1.5V and 2.5V.
 * Select the most appropriate voltage reference here
 */
ref2_5v: REFWOLT_LEVEL_2_5,
/*
 * adc12ssel: Select the clock source for the ADC. The default here uses Timer A. You typically
 * won't need to change this. If you do change the clock source, then you will need to comment
 * out '#define ADC12_TIMERA_ENABLED' in Msp430Adc12.h
 * Changing this value is only required for high speed sampling
 */
adc12ssel: SHT_SOURCE_ACLK,
/* adc12div: ADC clock division for adjusting clock speed */
adc12div: SHT_CLOCK_DIV_1,
/*
 * sht: For setting the sample and hold time in number of clock cycles of ADC clock source.
 * See page 17-9 of MSP430x1xx Family Users Guide for calculating the appropriate
 * sample and hold time.
 */
sht: SAMPLE_HOLD_4_CYCLES,
/*
 * samcon_ssel: The sample and hold clock source. The default setting here is the 32 kHz
 * clock for Timer A
 */
samcon_ssel: SAMPCON_SOURCE_SMCLK,
/* samcon_id: For adjusting clock speed again. No need to change this. */
samcon_id: SAMPCON_CLOCK_DIV_1
};
/*
 * This command is called by the ADC Read Client to configure the ADC channel
 * for use. It returns a pointer to the structure above.
 */
async command const msp430adc12_channel_config_t* AdcConfigure.getConfiguration() {
```

```
return&config;
}
}
```

MyAdcCs2.nc

```
/*
 * Generic ADC component –moduleRefer to the files in tos/chips/msp430/adc12
 * In particular: Msp430Adc12.h and README.txtAlso check the pin outs (and other data) in
 * the TMote Sky datasheet and the MSP430x1xx Family User's Guide (chapter 17).
 */
generic configuration MyAdcCs2() {
provides interface Read<uint16_t>;
}
implementation {
/*
 * The ADC Read Client provides the means for reading ADC values.It automatically does
 * resource reservation, reference voltage configuration,ADC configuration and returns the
 * sampled value to the calling application.There are alternative Clients available.
 */
components new AdcReadClientC();
  Read = AdcReadClientC;
components MyAdcPs2;
/*
 * This is where we tell the ADC Read Client that it can get the ADC
 * configuration structure from MyAdcP
 */
  AdcReadClientC.AdcConfigure -> MyAdcPs2;
}
}
```

MyAdcPs2.nc

```
#include "Msp430Adc12.h"
/*
 * Generic ADC component – moduleRefer to the files in tos/chips/msp430/adc12
 * In particular: Msp430Adc12.h and README.txtAlso check the pin outs (and other data) in
 * the TMote Sky datasheetand the MSP430x1xx Family User's Guide (chapter 17).
 */
module MyAdcPs2 {
provides interface AdcConfigure<const msp430adc12_channel_config_t*>;
}
implementation {
/*
 * This structure defines the operation of the ADC channel
 * Generally, you won't need to touch most of the fields
 */
msp430adc12_channel_config_t config = {
/*
 * inch: This selects the ADC channel to be used.There are 8 external ADC channels as part of
 * the MSP430 (see Msp430Adc12.h)The standard TelosB/TMote Sky mote only provides 6
 * channels (see datasheet)
 */
inch: INPUT_CHANNEL_A1,
/*
 * sref: This selects the voltage reference source for positive and negative(or ground) reference
 * voltage.Do not change (unless you have custom hardware)
 */
}
```

```
*/
sref: REFERENCE_VREFplus_AVss,
/*
* ref2_5v: There are 2 internal reference voltage options of 1.5V and 2.5V.
* Select the most appropriate voltage reference here
*/
ref2_5v: REFVOLT_LEVEL_2_5,
/*
* adc12ssel: Select the clock source for the ADC. The default here uses Timer A. You typically
* won't need to change this. If you do change the clock source, then you will need to comment
* out '#define ADC12_TIMERA_ENABLED' in Msp430Adc12.h
* Changing this value is only required for high speed sampling
*/
adc12ssel: SHT_SOURCE_ACLK,
/* adc12div: ADC clock division for adjusting clock speed*/
adc12div: SHT_CLOCK_DIV_1,

/*
* sht: For setting the sample and hold time in number of clock cycles of ADC clock source.
* See page 17-9 of MSP430x1xx Family Users Guide for calculating the appropriate sample
* and hold time.
*/
sht: SAMPLE_HOLD_4_CYCLES,
/*
* samcon_ssel: The sample and hold clock source.
* The default setting here is the 32 kHz clock for Timer A
*/
samcon_ssel: SAMPCON_SOURCE_SMCLK,
/* samcon_id: For adjusting clock speed again. No need to change this.*/
samcon_id: SAMPCON_CLOCK_DIV_1
};
/*
* This command is called by the ADC Read Client to configure the ADC channel
* for use. It returns a pointer to the structure above.
*/
async command const msp430adc12_channel_config_t* AdcConfigure.getConfiguration() {
return &config;
}
}
```